Electronic Supplementary Information for:

Linear Inverse Sandwich Complexes of Tetraanionic Benzene Stabilized by Covalent δ-Bonding with Late Lanthanides

K. Randall McClain,[§‡‡] Alexandre H. Vincent,[†‡‡] Ahmadreza Rajabi[¶‡‡], Danh X. Ngo,[†] Katie R. Meihaus, [†] Filipp Furche[¶]*, Benjamin G. Harvey,[§]* and Jeffrey R. Long[†,‡,#,‖]*

[§]US Navy, Naval Air Warfare Center, Weapons Division, Research Department, Chemistry Division, China Lake, California, 93555, United States

[†]Department of Chemistry, [‡]Department of Chemical and Biomolecular Engineering, and [#]Department of Materials Science and Engineering, University of California, Berkeley, Berkeley, California 94720, United States

[¶]Department of Chemistry, University of California Irvine, 1102 Natural Sciences II, Irvine, California 92697-2025, United States

Author Contributions

[‡‡]K.R.M., A.H.V. and A.R. are co-first authors, each contributing equally to the work.

Table of Contents

1. Synthesis and General Characterization

General Procedures. Unless otherwise specified, all manipulations were performed using Schlenk or glovebox techniques under an atmosphere of purified argon with rigorous exclusion of water and oxygen. All solvents were purchased from Sigma-Aldrich as anhydrous grade in Sure/Seal™ bottles, purged for several hours with purified argon, and stored over activated 3 Å molecular sieves in an argon filled glovebox. Celite (AW Standard Super-Cel® NF) was purchased from Sigma-Aldrich and dried under vacuum at 150–200 °C overnight before being transferred to the glovebox. Potassium graphite (KC_8) was purchased from Strem and used as received or synthesized by the reaction of graphite with potassium at ~100 °C under argon. Anhydrous LnI_3 were purchased from Alfa Aesar as Ultra Dry™ grade reagents and used as received. The salt $NaCp^{iPr5}$ was prepared using a previously published method.[1] The compounds $(Cp^{iPr5})_2Ln_2I_4$ (Ln = Y, Gd, Tb, Dy, Tm) were prepared using the previously reported procedure.[2]

Fourier transform infrared spectra (Section 7) were recorded on a Perkin Elmer Avatar Spectrum 400 FTIR Spectrometer equipped with an attenuated total reflectance attachment. UV-vis-NIR absorption spectra were collected with a CARY 5000 spectrophotometer interfaced with Varian WinUV software (Section 6). Matrix Assisted Laser Desorption Ionization Time of Flight (MALDI-ToF) mass spectra were recorded on an Applied Biosystems Voyager-DE PRO Workstation in positive ion mode (Section 8). Samples were co-crystalized in an anthracene matrix on an AB SCIEX MALDI-TOF stainless steel sample plate. Spectra were averaged over 200 laser pulses with a low mass gate of 400 Dalton and a high mass gate of 1500 Dalton. Elemental analyses (C, H, N) were performed by the Microanalytical Facility at the University of California, Berkeley using a Perkin-Elmer 2400 Series II combustion analyzer.

Synthesis of $[(Cp^{iPr5})Y]_2(\mu\text{-}C_6H_6)$ (1-Y). Under argon, $(Cp^{iPr5})_2Y_2I_4$ (0.580 g / 0.469 mmol) and diethyl ether (40 mL) were combined in a 100 mL Schlenk flask with a glass-coated magnetic stirring bar and benzene (4.17 mL / 3.66 g / 46.9 mmol) was added via syringe to give a nearly colorless solution. Under vigorous stirring, KC_8 (0.634 g / 4.69 mmol) was added; a greenish color was observed in solution initially, which changed to brown within minutes. The reaction mixture was allowed to stir for 4 days at room temperature, and then the solvent was removed under vacuum. The dark solid residue was extracted by stirring with 100 mL of boiling n-hexane for 0.5 h, then filtered through a medium porosity fritted glass filter loaded with Celite and the filter pad extracted with additional boiling n-hexane (2 × 15 mL) to give a dark reddish-brown filtrate. This was concentrated to ~30 mL, heated to redissolve any precipitate, then transferred to a 40 mL vial, wrapped in Al foil and allowed to cool to room temperature overnight, then transferred to the freezer (−35 °C). Dark red prism crystals of **1-Y** were isolated in multiple crops, washed with a small amount of cold (−35 °C) pentane and dried under vacuum. (0.135 g / 0.167 mmol / 36 % based on $(Cp^{iPr5})_2Y_2I_4$). ^{1}H NMR (C_6D_6, 500 MHz, 298 K): δ = 1.29 (d, 30H, Cp–CH(CH_3)$_2$), 1.59 (d, 30H, Cp–CH(CH_3)$_2$), 3.24 (sept, 10H, Cp–CH(CH$_3$)$_2$), 3.75 (s, Y-C$_6H_6$-Y). ^{13}C{^{1}H} NMR (C_6D_6, 125 MHz, 298 K): δ = 23.78, 25.74 (Cp–CH(*C*H$_3$)$_2$), 27.21 (Cp–*C*H(CH$_3$)$_2$), 59.39 (t, J = 4.4 Hz, Y–*C*$_6$H$_6$–Y), 126.35 (*Cp*–CH(CH$_3$)$_2$). ^{89}Y NMR (C_6D_6, 25 MHz, 298 K): δ = −103 (*Y*–C$_6$H$_6$–*Y*). MALDI-ToF MS *m/z*: 807.02(1) ([M]$^+$). $C_{46}H_{76}Y_2$ (806.93): calcd (%) C 68.47, H 9.49; found (%) C 68.30, H 9.36.

Synthesis of $[(Cp^{iPr5})Gd]_2(\mu\text{-}C_6H_6)$ (1-Gd). Under argon, $(Cp^{iPr5})_2Gd_2I_4$ (0.540 g / 0.393 mmol) and diethyl ether (40 mL) were combined in a 100 mL Schlenk flask with a glass-coated magnetic stirring bar and benzene (3.49 mL / 3.07 g / 39.3 mmol) was added via syringe to give a light yellow solution. Under vigorous stirring, KC_8 (0.531 g / 3.93 mmol) was added; a blue color was

observed in solution initially, which changed to reddish-brown within minutes. The reaction mixture was allowed to stir for 4 days at room temperature, then solvent was removed under vacuum. The dark solid residue was extracted by stirring with 100 mL of boiling n-hexane for 0.5 h, then filtered through a medium porosity fritted glass filter loaded with Celite and the filter pad extracted with additional boiling n-hexane (2 × 15 mL) to give a dark reddish-brown filtrate. This was concentrated to ~40 mL, heated to redissolve any precipitate, then transferred in approximately equivalent volume to two 40 mL vials, wrapped in Al foil and allowed to cool to room temperature overnight, then transferred to the freezer (−35 °C). Dark reddish-brown prism crystals of **1-Gd** were isolated in multiple crops, washed with a small amount of cold (−35 °C) pentane and dried under vacuum. (0.172 g / 0.182 mmol / 46 % based on $(Cp^{iPr5})_2Gd_2I_4$). MALDI-ToF MS *m/z*: 942.510(3) ($[M]^+$). $C_{46}H_{76}Gd_2$ (943.61): calcd (%) C 58.55, H 8.12; found (%) C 58.18, H 8.00.

Synthesis of $[(Cp^{iPr5})Tb]_2(\mu\text{-}C_6H_6)$ (1-Tb). Under argon, $(Cp^{iPr5})_2Tb_2I_4$ (0.400 g / 0.291 mmol) and diethyl ether (40 mL) were combined in a 100 mL Schlenk flask with a glass-coated magnetic stirring bar and benzene (2.58 mL / 2.27 g / 29.1 mmol) was added via syringe to give a light yellow solution. Under vigorous stirring, KC_8 (0.393 g / 2.91 mmol) was added; a blue color was observed in solution initially, which changed to reddish-brown within minutes. The reaction mixture was allowed to stir for 4 days at room temperature, then solvent was removed under vacuum. The dark solid residue was extracted by stirring with 100 mL of boiling n-hexane for 0.5 h, then filtered through a medium porosity fritted glass filter loaded with Celite and the filter pad extracted with additional boiling n-hexane (2 × 15 mL) to give a dark reddish-brown filtrate. This was concentrated to ~8 mL, heated to redissolve any precipitate, then transferred to a 40 mL vial, wrapped in Al foil and allowed to cool to room temperature overnight, then transferred to the freezer (−35 °C). Dark reddish-brown prism crystals of **1-Tb** were isolated in multiple crops, washed with a small amount of cold (−35 °C) pentane and dried under vacuum. (0.075 g / 0.079 mmol / 27 % based on $(Cp^{iPr5})_2Tb_2I_4$). MALDI-ToF MS *m/z*: 946.218(7) ($[M]^+$). $C_{46}H_{76}Tb_2$ (946.96): calcd (%) C 58.34, H 8.09; found (%) C 58.68, H 7.85.

Synthesis of $[(Cp^{iPr5})Dy]_2(\mu\text{-}C_6H_6)$ (1-Dy). Under argon, $(Cp^{iPr5})_2Dy_2I_4$ (0.420 g / 0.304 mmol) and diethyl ether (40 mL) were combined in a 100 mL Schlenk flask with a glass-coated magnetic stirring bar and benzene (2.70 mL / 2.37 g / 30.3 mmol) was added via syringe to give a light yellow solution. Under vigorous stirring, KC_8 (0.410 g / 3.03 mmol) was added; a blue color was observed in solution initially, which changed to reddish-brown within minutes. The reaction mixture was allowed to stir for 4 days at room temperature, then solvent was removed under vacuum. The dark solid residue was extracted by stirring with 100 mL of boiling n-hexane for 0.5 h, then filtered through a medium porosity fritted glass filter loaded with Celite and the filter pad extracted with additional boiling n-hexane (2 × 15 mL) to give a dark reddish-brown filtrate. This was concentrated to ~20 mL, heated to redissolve any precipitate, then transferred to a 40 mL vial, wrapped in Al foil and allowed to cool to room temperature overnight, then transferred to the freezer (−35 °C). Dark reddish-brown prism crystals of **1-Dy** were isolated in multiple crops, washed with a small amount of cold (−35 °C) pentane and dried under vacuum. (0.132 g / 0.138 mmol / 45 % based on $(Cp^{iPr5})_2Dy_2I_4$). MALDI-ToF MS *m/z*: 953.88(1) ($[M]^+$). $C_{46}H_{76}Dy_2$ (954.11): calcd (%) C 57.91, H 8.03; found (%) C 57.58, H 7.68.

Synthesis of $[(Cp^{iPr5})Tm]_2(\mu\text{-}C_6H_6)$ (1-Tm). Under argon, $(Cp^{iPr5})_2Tm_2I_4$ (0.500 g / 0.358 mmol) and diethyl ether (40 mL) were combined in a 100 mL Schlenk flask with a glass-coated magnetic stirring bar and benzene (3.18 mL / 2.80 g / 35.8 mmol) was added via syringe to give a yellow-

orange solution. Under vigorous stirring, KC_8 (0.484 g / 3.58 mmol) was added and the reaction mixture was allowed to stir for 4 days at room temperature, then solvent was removed under vacuum. The dark solid residue was extracted by stirring with 100 mL of boiling n-hexane for 0.5 h, then filtered through a medium porosity fritted glass filter loaded with Celite and the filter pad extracted with additional boiling n-hexane (2 × 15 mL) to give a dark reddish-brown filtrate. This was concentrated to ~20 mL, heated to redissolve any precipitate, then transferred to a 40 mL vial, wrapped in Al foil and allowed to cool to room temperature overnight, then transferred to the freezer (−35 °C). Dark brown prism crystals of **1-Tm** were isolated in multiple crops, washed with a small amount of cold (−35 °C) pentane and dried under vacuum. (0.156 g / 0.161 mmol / 45 % based on $(Cp^{iPr5})_2Tm_2I_4$). MALDI-ToF MS *m/z*: 966.27(1) ($[M]^+$). $C_{46}H_{76}Tm_2$ (966.98): calcd (%) C 57.14, H 7.92; found (%) C 57.20, H 7.83.

2. X-ray Crystallography Data Collection and Refinement Details

Single crystal X-ray diffraction data were collected as follows. Samples were coated with Parabar oil and mounted on a MiTeGen polyimide loop. X-ray intensity data were measured using a Bruker SMART Apex II diffractometer equipped with a PHOTON II CPAD detector. Data collection was performed at 100 K under the N_2 stream of an Oxford Cryosystems Cryostream with MoKα radiation (graphite monochrometer) at a detector distance of 6 cm. The frames were integrated and scaling was performed using APEX3 software, including a multi-scan absorption correction.[3–5] Crystal structure models were obtained using intrinsic phasing method as implemented in ShelXT.[6] The structural models were refined with least-squares fitting as implemented in ShelXL.[7] Olex2 was used as a graphical frontend throughout the refinement process.[8]

CheckCIF A & B Level Alerts

1-Y:
PLAT215_ALERT_3_B Disordered C11 has ADP max/min Ratio ..... 4.7 Note

C11 is one of the rotationally disordered carbon atoms of the benzene ring. The large ADP max/min ratio is a product of the incomplete modeling of the rotational disorder combined with the equivalent occupancies given to each of the disordered components. A simplified model with equivalent chemical occupancies for each disordered benzene position was used to overcome refinement instability which was observed when the chemical occupancy values were floating. 1 reflection (-2 0 2) was omitted from the refinement due to a large difference in *I*(obs) and *I*(calc), as recommended by the PLAT934 alert. This reflection was likely affected by the beamstop.

1-Gd:
2 reflections (-4 0 2, -3 0 1) were omitted from the refinement due to large differences in *I*(obs) and *I*(calc), as recommended by the PLAT934 alert. These reflections were likely affected by the beamstop.

1-Tb:
2 reflections (-4 0 2, -3 0 1)were omitted from the refinement due to large differences in *I*(obs) and *I*(calc), as recommended by the PLAT934 alert. These reflections were likely affected by the beamstop.

1-Dy:
PLAT215_ALERT_3_B Disordered C4 has ADP max/min Ratio ..... 4.2 Note

C4 is one of the rotationally disordered carbon atoms of the benzene ring. The large ADP max/min ratio is a product of the incomplete modeling of the rotational disorder combined with the equivalent occupancies given to each of the disordered components. A simplified model with equivalent chemical occupancies for each disordered benzene position was used to overcome refinement instability which was observed when the chemical occupancy values were floating.

2 reflections (-4 0 2, -3 0 1) were omitted from the refinement due to large differences in *I*(obs) and *I*(calc), as recommended by the PLAT934 alert. These reflections were likely affected by the beamstop.

1-Tm:
4 reflections (0 1 1, -1 0 1, 1 0 1, -4 0 2) were omitted from the refinement due to large differences in *I*(obs) and *I*(calc), as recommended by the PLAT934 alert. These reflections were likely affected by the beamstop.

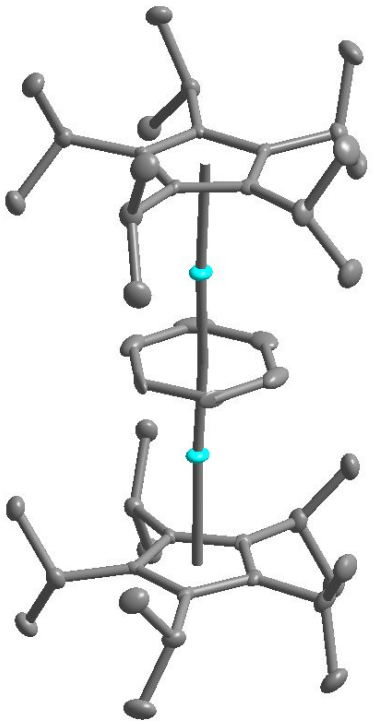

Figure S1. Crystal structure of **1-Y** with thermal ellipsoids drawn at the 50% probability level. Cyan and gray ellipsoids represent Y and C atoms, respectively. Hydrogen atoms and minor disorder positions for Cp^{iPr5} and benzene have been omitted for clarity.

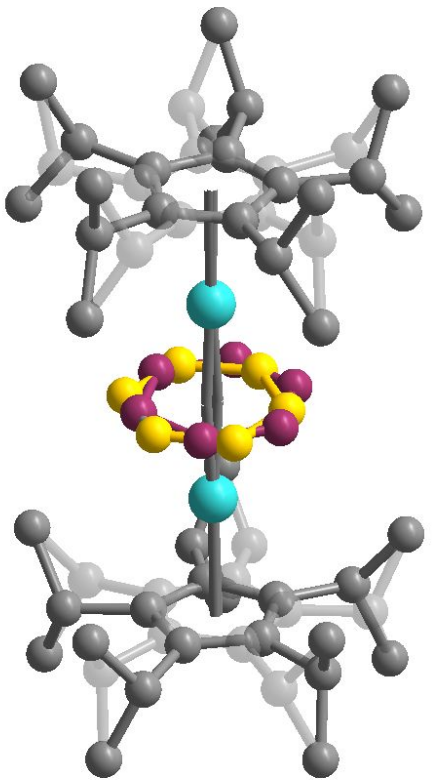

Figure S2. Crystal structure of **1-Y**. Cyan and gray spheres represent Y and C atoms, respectively. Hydrogen atoms have been omitted for clarity. Minor disorder positions for Cp^{iPr5} are shown as transparent spheres (Chemical Occupancy: ~0.3) Major Cp^{iPr5} positions are shown as opaque spheres (Chemical Occupancy: ~0.7). The in-plane rotational disorder of benzene is presented as the yellow and magenta spheres. Both rotational positions have equal chemical occupancy values of 0.5. The disorder pattern illustrated here for **1-Y** is the same for other **1-Ln**.

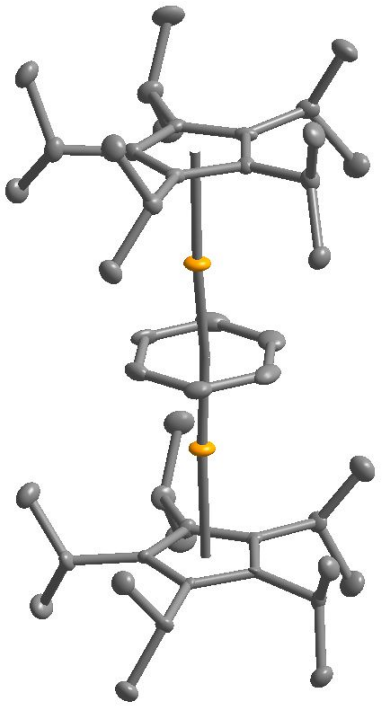

Figure S3. Crystal structure of **1-Gd**. Gd, orange; C, gray. Ellipsoids are drawn at 50% probability. Hydrogen atom and minor disorder positions for Cp^{iPr5} and benzene have been omitted for clarity.

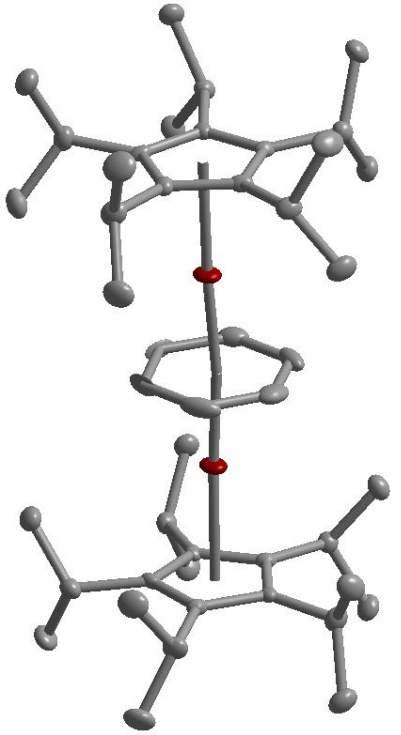

Figure S4. Crystal structure of **1-Tb**. Tb, red; C, gray. Ellipsoids are drawn at 50% probability. Hydrogen atoms and minor disorder positions for Cp^{iPr5} and benzene have been omitted for clarity.

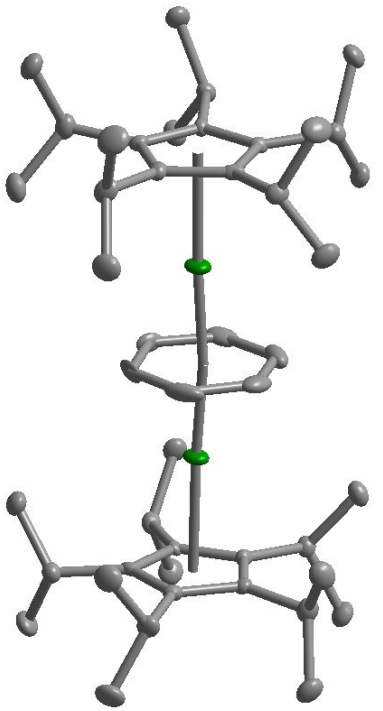

Figure S5. Crystal structure of **1-Dy**. Dy, green; C, gray. Ellipsoids are drawn at 50% probability. Hydrogen atoms and minor disorder positions for Cp^{iPr5} and benzene have been omitted for clarity.

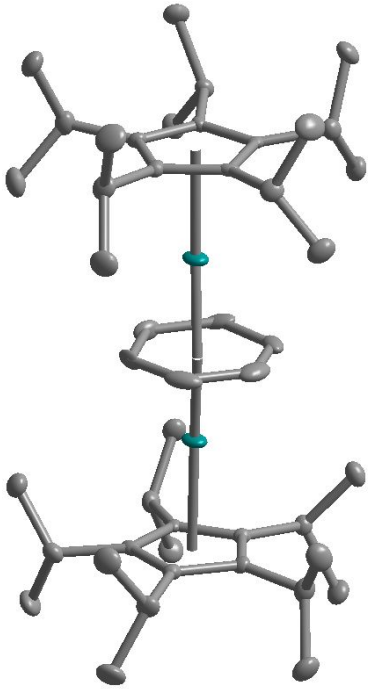

Figure S6. Crystal structure of **1-Tm**. Tm, blue; C, gray. Ellipsoids are drawn at 50% probability. Hydrogen atoms and minor disorder positions for Cp^{iPr5} and benzene have been omitted for clarity.

Table S1. Selected distances for **1-Ln**. All distances are given in Å. Cp(centroid)1 corresponds to major Cp^{iPr5} disordered position. Bz corresponds to benzene. Estimated standard deviations are given in parentheses.

Bz C–C Bond Index	**1-Y**	**1-Gd**	**1-Tb**	**1-Dy**	**1-Tm**
1	1.454(9)	1.48(1)	1.46(1)	1.46(2)	1.437(9)
2	1.451(8)	1.46(1)	1.483(8)	1.447(9)	1.44(1)
3	1.46(2)	1.47(1)	1.452(9)	1.454(9)	1.47(1)
4	1.46(1)	1.46(1)	1.446(7)	1.46(1)	1.471(9)
5	1.489(8)	1.440(9)	1.460(8)	1.483(9)	1.48(2)
6	1.45(1)	1.44(1)	1.45(2)	1.47(2)	1.47(2)
Average	**1.46(1)**	**1.46(2)**	**1.46(1)**	**1.46(1)**	**1.46(2)**
M–Cp(centroid)1	2.3676(2)	2.4202(2)	2.3979(1)	2.3819(3)	2.3281(1)
M–Cp(centroid)2	2.3705(2)	2.4228(2)	2.4084(1)	2.3859(3)	2.3262(1)
M–Bz(centroid)1	1.9831(2)	2.0323(2)	2.00525(9)	1.9804(2)	1.9408(1)
M–Bz(centroid)2	1.9949(2)	2.0447(2)	2.0198(1)	2.0097(2)	1.9435(1)

Table S2. Weighted average details for Cp^{iPr5}(centroid) distances. All distances are given in Å. Weighting coefficients are unitless.

	1-Y		**1-Gd**		**1-Tb**		**1-Dy**		**1-Tm**	
	Dist	weight	Dist	weight	Dist	weight	Dist	weight	Dist	weight
Cent1	2.3676	0.676	2.4202	0.670	2.3979	0.708	2.3819	0.693	2.3281	0.682
Cent2	2.3705	0.324	2.4228	0.33	2.4084	0.292	2.3859	0.307	2.3262	0.318
W. Avg.	2.369(2)		2.421(2)		2.401(7)		2.383(3)		2.327(1)	

Table S3. Unit Cell Metrics and Refinement Parameters for **1-Ln** (Ln = Y, Gd, Tb, Dy, Tm).

Compound	**1-Y**	**1-Gd**	**1-Tb**	**1-Dy**	**1-Tm**
Empirical formula	$C_{46}H_{70}Y_2$	$C_{46}H_{70}Gd_2$	$C_{46}H_{70}Tb_2$	$C_{46}H_{70}Dy_2$	$C_{46}H_{70}Tm_2$
Formula weight	800.84	937.52	940.86	948.02	960.88
Temp/K	100	100	100	100	100
Crystal system	monoclinic	monoclinic	monoclinic	monoclinic	monoclinic
Space group	P2/n	P2/n	P2/n	P2/n	P2/n
a/Å	15.3920(9)	15.5090(5)	15.4480(5)	15.4016(13)	15.2497(3)
b/Å	9.8462(5)	9.8117(3)	9.8220(3)	9.8337(8)	9.8545(2)
c/Å	16.2170(9)	16.2094(5)	16.1975(6)	16.2056(14)	16.1989(3)
α/°	90	90	90	90	90
β/°	116.440(2)	116.8010(10)	116.5860(10)	116.477(2)	116.1200(10)
γ/°	90	90	90	90	90
Volume/Å^3	2200.7(2)	2201.61(12)	2197.79(13)	2197.0(3)	2185.73(8)
Z	2	2	2	2	2
ρ_{calc}g/cm^3	1.209	1.414	1.422	1.433	1.46
μ/mm^{-1}	2.651	3.013	3.219	3.402	4.06
F(000)	848	948	952	956	968
Crystal size/mm^3	0.363 × 0.199 × 0.128	0.194 × 0.171 × 0.104	0.178 × 0.155 × 0.138	0.17 × 0.139 × 0.099	0.265 × 0.154 × 0.144
Radiation	MoKα (λ = 0.71073)	MoKα (λ = 0.71073)	MoKα (λ = 0.71073)	MoKα (λ = 0.71073)	MoKα (λ = 0.71073)
2Θ range for data collection/°	4.136 to 50.7	4.152 to 50.7	4.146 to 50.692	4.142 to 50.694	4.134 to 50.698
Index ranges	-18 ≤ h ≤ 18, -11 ≤ k ≤ 11, -19 ≤ l ≤ 19	-18 ≤ h ≤ 18, -11 ≤ k ≤ 11, -19 ≤ l ≤ 19	-18 ≤ h ≤ 18, -11 ≤ k ≤ 11, -19 ≤ l ≤ 19	-18 ≤ h ≤ 18, -11 ≤ k ≤ 11, -19 ≤ l ≤ 19	-18 ≤ h ≤ 18, -11 ≤ k ≤ 11, -19 ≤ l ≤ 19
Reflections collected	69663	68406	26344	26260	58751
Independent reflections	4020 [R_{int} = 0.0556, R_{sigma} = 0.0217]	4032 [R_{int} = 0.0482, R_{sigma} = 0.0171]	4016 [R_{int} = 0.0184, R_{sigma} = 0.0118]	4014 [R_{int} = 0.0227, R_{sigma} = 0.0137]	3987 [R_{int} = 0.0247, R_{sigma} = 0.0103]
Data/restraints/parameters	4020/98/345	4032/122/345	4016/104/345	4014/107/345	3987/86/345
Goodness-of-fit on F^2	1.096	1.078	1.069	1.076	1.139
Final R indexes [I>=2σ (I)]	R_1 = 0.0224, wR_2 = 0.0551	R_1 = 0.0163, wR_2 = 0.0377	R_1 = 0.0120, wR_2 = 0.0313	R_1 = 0.0130, wR_2 = 0.0332	R_1 = 0.0112, wR_2 = 0.0285
Final R indexes [all data]	R_1 = 0.0275, wR_2 = 0.0574	R_1 = 0.0193, wR_2 = 0.0390	R_1 = 0.0129, wR_2 = 0.0317	R_1 = 0.0141, wR_2 = 0.0336	R_1 = 0.0132, wR_2 = 0.0303
Largest diff. peak/hole / e Å^{-3}	0.39/-0.22	0.52/-0.48	0.43/-0.24	0.40/-0.37	0.36/-0.41

3. Tabulated Molecular Planarity Parameters for 1-Ln and Literature Compounds

As discussed in the main text, we used molecular planarity parameter (MPP)[9] in order to quantify the degree of arene distortion from planarity in **1-Ln** and as a metric for comparison with all Ln–(η^6-Ar) containing compounds in the CSD. The MPP is defined as follows:

$$MPP = \sqrt{\frac{\sum_{n=1}^{6} {D_n}^2}{N}} \qquad \text{Eq S1,}$$

where D_n is the magnitude of the displacement vector from the mean plane to atom n and N is the total number of atoms in the ring. The mean plane for each **1-Ln** and reported literature compounds were calculated in Mercury4[10] using the six ring carbon positions. In the tables below, D_n and corresponding MPP values are tabulated for **1-Ln** (Table S4) and Y, Gd, Tb, Dy, and Tm literature compounds (Tables S5 through S9, respectively).

Table S4. Tabulated D_n and MPP values for **1-Ln** compared with MPP ranges based on literature Ln–(η^6-Ar) containing compounds of the corresponding lanthanides. Compounds featuring only η^6-bound tetraphenylborates were excluded from the literature query results.

1-Ln	D_1 (Å)	D_2 (Å)	D_3 (Å)	D_4 (Å)	D_5 (Å)	D_6 (Å)	**MPP (Å)**	Lit. Range of MPP (Å)
1-Y	0.0015	0.0057	0.0128	0.0003	0.0022	0.0005	6×10^{-3}	4×10^{-3} to 1.3×10^{-1}
1-Gd	0.0010	0.0028	0.0018	0.0009	0.0045	0.0043	3×10^{-3}	5×10^{-3} to 6.2×10^{-2}
1-Tb	0.0063	0.0016	0.0004	0.0156	0.0000	0.0048	7×10^{-3}	1.4×10^{-2} *
1-Dy	0.0168	0.0015	0.0028	0.0009	0.0006	0.0007	7×10^{-3}	6×10^{-3} to 1.7×10^{-1}
1-Tm	0.0048	0.0356	0.0066	0.0003	0.0061	0.0009	2×10^{-2}	2×10^{-3} to 1.4×10^{-1}

*Only one Tb–η^6-Ar structure was found in the CSD (see Table S7).

Table S5. Tabulated D_n and MPP values for all Y-(η^6-Ar) containing compounds in the CSD. Compounds featuring only η^6-bound tetraphenylborates were excluded from the query results.

CSD CODE	D_1 (Å)	D_2 (Å)	D_3 (Å)	D_4 (Å)	D_5 (Å)	D_6 (Å)	**MPP (Å)**	Ref.
CUKLOL	0.089	0.100	0.196	0.101	0.089	0.182	0.13	11
EZIBUN*	0.000	0.000	0.000	0.000	0.000	0.000	0.000	12
GIRHUN	0.019	0.039	0.042	0.024	0.004	0.001	0.03	13
ICAWOC	0.001	0.003	0.013	0.019	0.014	0.004	0.01	14
ICELEL	0.001	0.003	0.000	0.004	0.006	0.004	0.004	14
KUGLUV	0.005	0.003	0.002	0.005	0.002	0.003	0.004	15
KUGLUV	0.003	0.005	0.010	0.007	0.000	0.005	0.006	15
MALXAY	0.009	0.000	0.011	0.014	0.004	0.007	0.009	16
MUXDUH	0.035	0.026	0.004	0.009	0.001	0.023	0.02	17
NIVNEL	0.044	0.013	0.041	0.065	0.034	0.021	0.040	18
NIVNIP	0.003	0.028	0.032	0.006	0.025	0.029	0.02	18
ODEYEB	0.032	0.019	0.022	0.050	0.036	0.004	0.03	19
TOPFOT	0.015	0.057	0.052	0.003	0.038	0.032	0.04	20
TOPFOT	0.029	0.002	0.013	0.000	0.029	0.042	0.002	20
XEKRIP	0.024	0.020	0.047	0.029	0.017	0.043	0.032	21
YEMWOE	0.000	0.075	0.073	0.000	0.073	0.075	0.060	22
YEMWUK	0.000	0.063	0.062	0.000	0.062	0.063	0.051	22
YEMXUL	0.000	0.082	0.081	0.000	0.081	0.082	0.067	22
EZICEY	0.007	0.012	0.014	0.005	0.024	0.024	0.02	12
				Average MPP*			0.033	

*EZIBUN was excluded from literature average as six membered ring appears to have been fixed to a plane during structure refinement

Table S6. Tabulated D_n and MPP values for all Gd-(η^6-Ar) containing compounds in the CSD. Compounds featuring only η^6-bound tetraphenylborates were excluded from the query results.

CSD CODE	D_1 (Å)	D_2 (Å)	D_3 (Å)	D_4 (Å)	D_5 (Å)	D_6 (Å)	**MPP (Å)**	Ref.
QATNAE	0.001	0.009	0.018	0.017	0.007	0.002	0.01	23
QATNAE	0.020	0.012	0.004	0.012	0.003	0.013	0.01	23
QATNUY	0.019	0.022	0.017	0.007	0.003	0.009	0.01	23
FOGJEQ	0.005	0.018	0.019	0.003	0.027	0.027	0.02	24
POXMEW	0.000	0.064	0.062	0.000	0.062	0.064	0.051	25
POXMOG	0.074	0.071	0.006	0.081	0.077	0.001	0.06	25
YEHLAB	0.019	0.035	0.035	0.019	0.003	0.003	0.02	26
YEHLIJ	0.025	0.025	0.025	0.025	0.025	0.025	0.025	26
YILSOB*	0.000	0.000	0.000	0.000	0.000	0.000	0.000	27
EZICAU	0.001	0.002	0.005	0.007	0.007	0.003	0.005	12
EZICIC	0.013	0.011	0.000	0.009	0.007	0.004	0.009	12
Average MPP*							**0.023**	

*YILSOB was excluded from literature average as six membered ring appears to have been fixed to a plane during structure refinement

Table S7. Tabulated D_n and MPP values for all Tb-(η^6-Ar) containing compounds in CSD. Compounds featuring only η^6-bound tetraphenylborates were excluded from the query results.

CSD CODE	D_1 (Å)	D_2 (Å)	D_3 (Å)	D_4 (Å)	D_5 (Å)	D_6 (Å)	**MPP (Å)**	Ref.
QOPZEC	0.007	0.02	0.014	0.004	0.017	0.012	0.014	28
Average MPP							**0.014**	

Table S8. Tabulated D_n and MPP values for all Dy-(η^6-Ar) containing compounds in CSD. Compounds featuring only η^6-bound tetraphenylborates were excluded from the query results.

CSD CODE	D_1 (Å)	D_2 (Å)	D_3 (Å)	D_4 (Å)	D_5 (Å)	D_6 (Å)	**MPP (Å)**	Ref.
JIZVIA	0.014	0.011	0.002	0.012	0.009	0.004	0.01	29
JIZVIA	0.025	0.010	0.013	0.021	0.007	0.017	0.02	29
JIZVIA	0.032	0.021	0.010	0.031	0.019	0.013	0.023	29
JIZVIA	0.033	0.016	0.014	0.028	0.011	0.019	0.022	29
BEWWOP	0.231	0.112	0.128	0.241	0.116	0.116	0.167	30
DUXGUB	0.017	0.010	0.025	0.013	0.014	0.030	0.019	29
HATPAW	0.003	0.003	0.004	0.010	0.010	0.003	0.006	28
HATPEA	0.024	0.027	0.011	0.007	0.010	0.006	0.02	28
LOKQAE	0.005	0.008	0.011	0.000	0.013	0.016	0.01	31
MUXFAP	0.038	0.029	0.004	0.012	0.002	0.023	0.02	17
POXMAS	0.000	0.074	0.072	0.000	0.072	0.074	0.060	25
POXMIA	0.000	0.083	0.082	0.000	0.082	0.083	0.067	25
QOPZIG	0.005	0.017	0.013	0.002	0.014	0.010	0.01	32
WAQYUJ	0.007	0.014	0.005	0.010	0.018	0.008	0.01	33
YEHDEX	0.024	0.024	0.024	0.024	0.024	0.024	0.024	26
YEHKUU	0.018	0.033	0.034	0.021	0.006	0.005	0.02	26
YEHMAC	0.005	0.002	0.012	0.033	0.041	0.027	0.02	26
Average MPP							**0.031**	

Table S9. Tabulated D_n and MPP values for all Tm-(η^6-Ar) containing compounds in CSD. Compounds featuring only η^6-bound tetraphenylborates were excluded from the query results.

CSD CODE	D_1 (Å)	D_2 (Å)	D_3 (Å)	D_4 (Å)	D_5 (Å)	D_6 (Å)	**MPP (Å)**	Ref.
FUQFIH	0.004	0.003	0.000	0.002	0.001	0.002	0.002	34
MAWXAK	0.002	0.002	0.010	0.018	0.018	0.010	0.01	35
RIRQOY	0.062	0.178	0.102	0.095	0.204	0.123	0.14	36
SALJAR	0.005	0.001	0.007	0.009	0.004	0.003	0.005	37
Average MPP							**0.039**	

4. Magnetometry

All magnetic measurements were carried out using a Quantum Design MPMS-XL SQUID magnetometer. Crystalline samples were dried under vacuum, mechanically ground, loaded into a quartz tube (inner diameter of 5 mm, outer diameter of 7 mm), covered with a solid layer of eicosane, and flame sealed under vacuum. The eicosane was subsequently melted at 40 °C (80 °C for **1-Dy**) in order to restrain the sample (prevent crystallite torquing) and to improve thermal conductivity between the sample and the environment. Diamagnetic corrections were calculated using Pascal's constants,[38] and were applied to all reported magnetic susceptibility values unless otherwise noted. Material quantities: **1-Gd**, 31.6 mg sample ($-\chi_M^{dia} = 5.38 \times 10^{-3}$ emu/mol) with 61.0 mg of eicosane ($-\chi_M^{dia} = 2.43 \times 10^{-3}$ emu/mol). **1-Tb**, 8.6 mg sample ($-\chi_M^{dia} = 5.37\times 10^{-3}$ emu/mol) with 30.2 mg eicosane ($-\chi_M^{dia} = 2.43 \times 10^{-3}$ emu/mol). **1-Dy**, 12.8 mg sample ($-\chi_M^{dia} = 5.37 \times 10^{-3}$ emu/mol) with 48.2 mg eicosane ($-\chi_M^{dia} = 2.43 \times 10^{-3}$ emu/mol). **1-Tm**, 29.2 mg sample ($-\chi_M^{dia} = 5.35 \times 10^{-3}$ emu/mol) with 86.3 mg eicosane ($-\chi_M^{dia} = 2.43 \times 10^{-3}$ emu/mol).

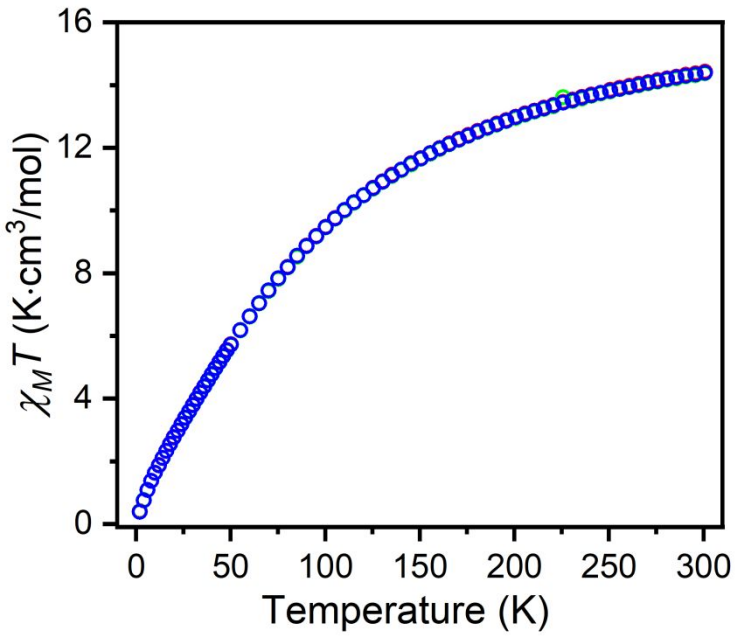

Figure S7. Dc magnetic susceptibility data for **1-Gd** measured under 0.1 T (red), 0.5 T (green) and 1 T (blue) applied fields. All the data overlay.

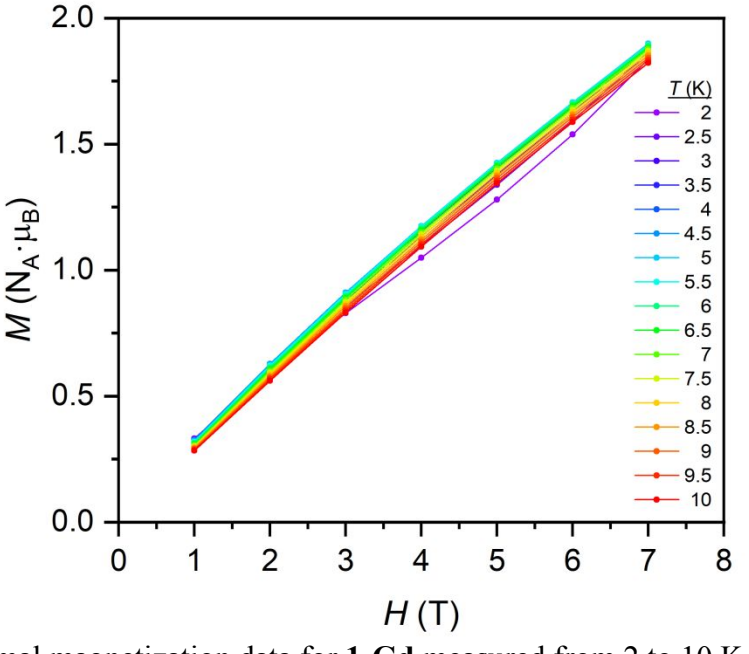

Figure S8. Isothermal magnetization data for **1-Gd** measured from 2 to 10 K. Solid lines are guides for the eye.

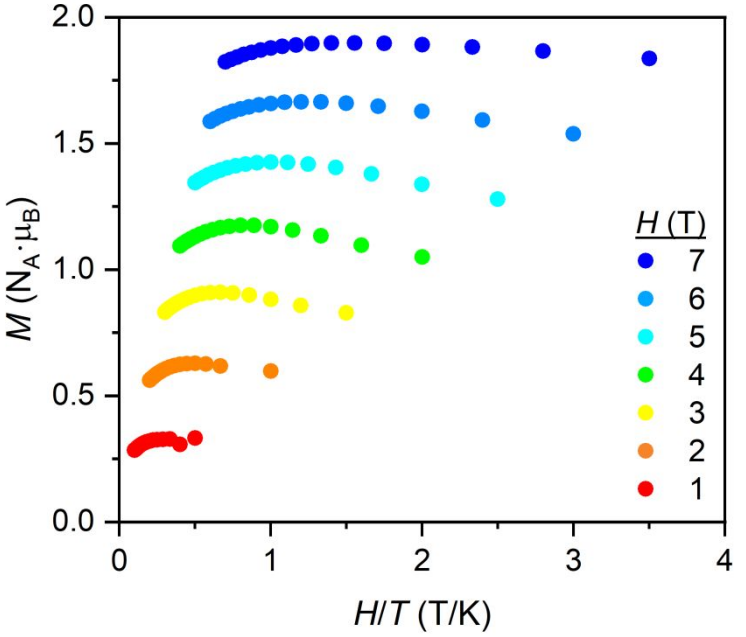

Figure S9. Reduced magnetization data collected for **1-Gd** measured under applied fields ranging from 1 to 7 T.

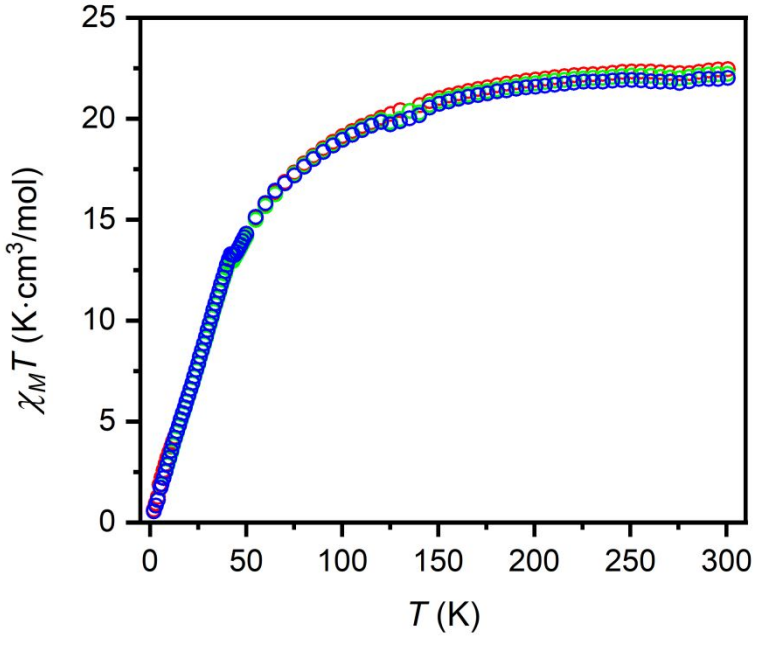

Figure S10. Dc magnetic susceptibility data for **1-Tb** collected under fields of 0.1 T (red), 0.5 T (green) and 1 T (blue).

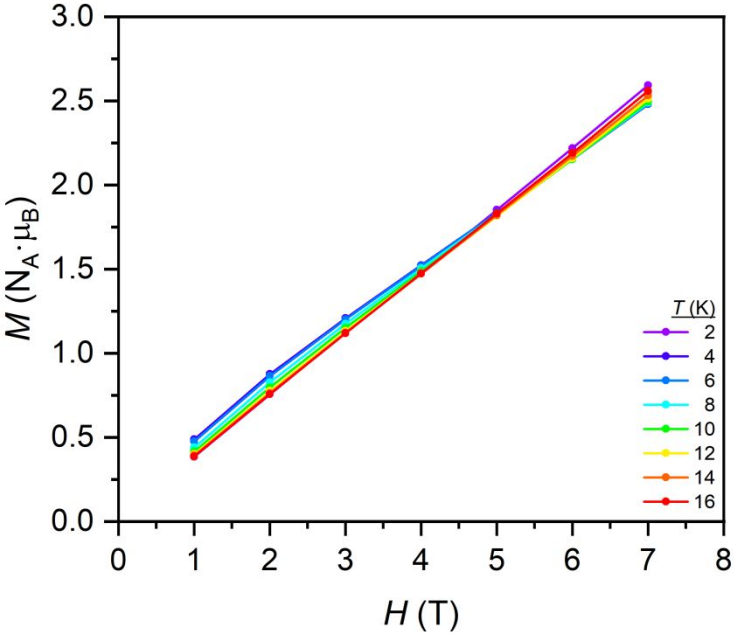

Figure S11. Isothermal magnetization data collected for **1-Tb** measured from 2 to 16 K. Solid lines are guides for the eye.

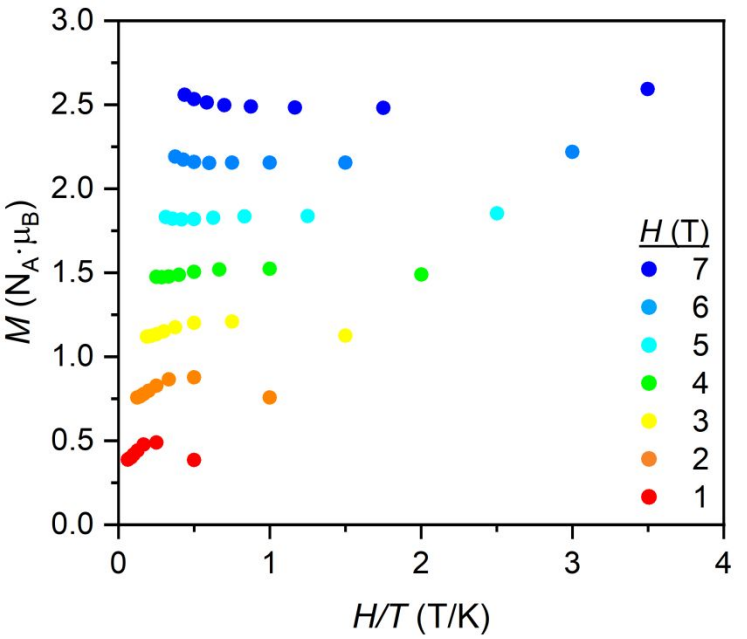

Figure S12. Reduced magnetization data for **1-Tb** collected under applied fields ranging from 1 to 7 T.

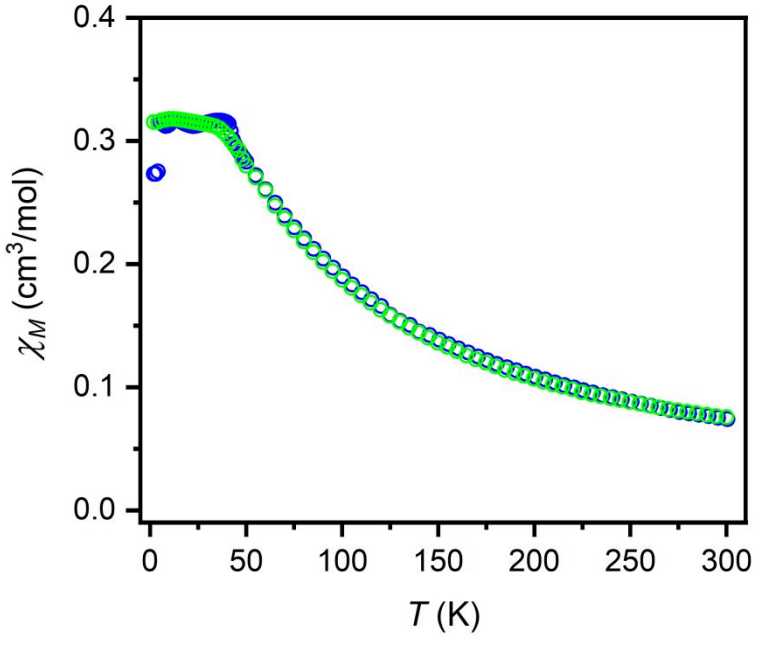

Figure S13. Field cooled (green circles) and zero-field cooled (blue circles) molar magnetic susceptibility data for **1-Tb** measured under a 0.5 T field.

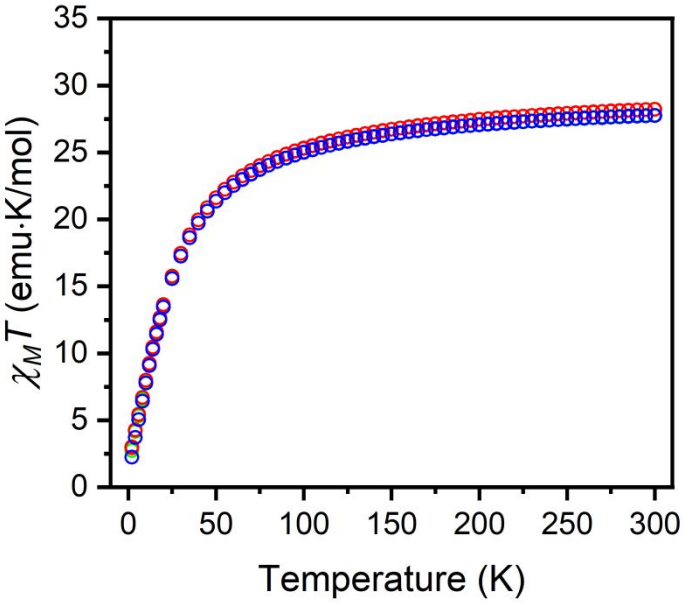

Figure S14. Dc magnetic susceptibility data for **1-Dy** collected under 0.1 T (red), 0.5 T (green) and 1 T (blue) applied fields.

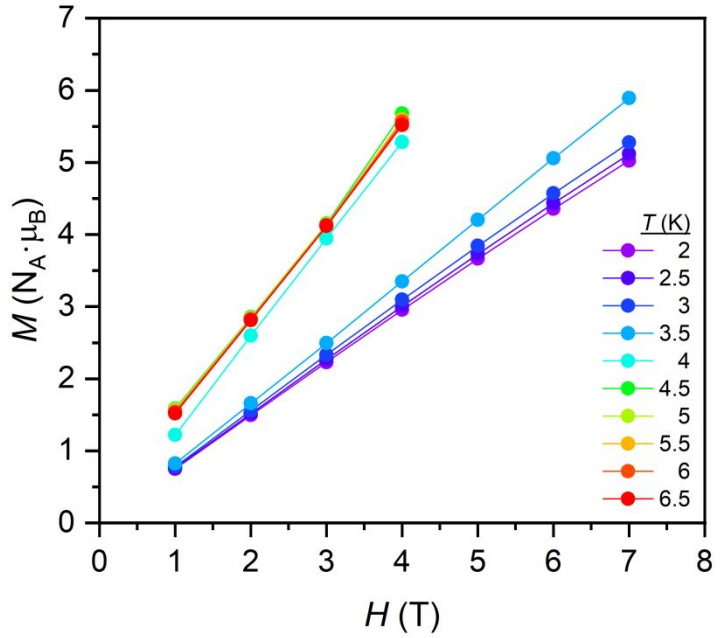

Figure S15. Isothermal magnetization data for **1-Dy**. Solid lines are guides for the eye. At 4 K and higher temperatures, the magnetization saturated the SQUID detector at fields beyond 4 T.

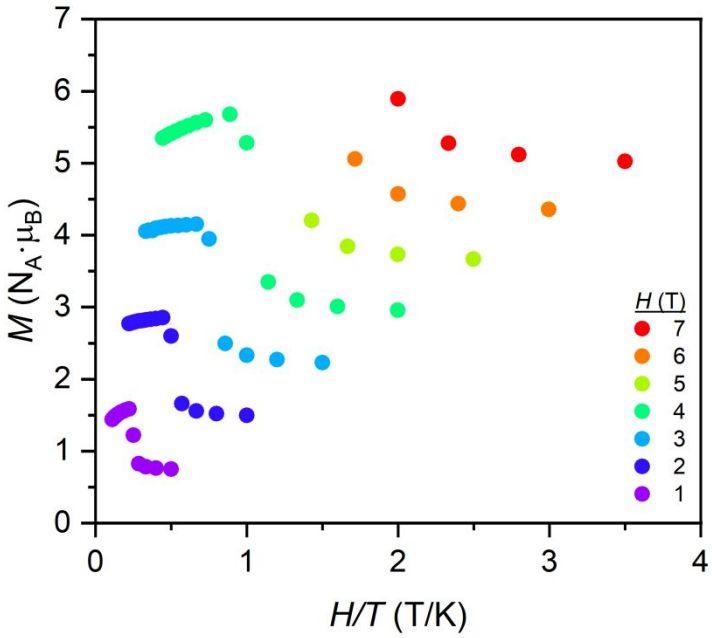

Figure S16. Reduced magnetization data for **1-Dy** collected under applied fields ranging from 1 to 7 T.

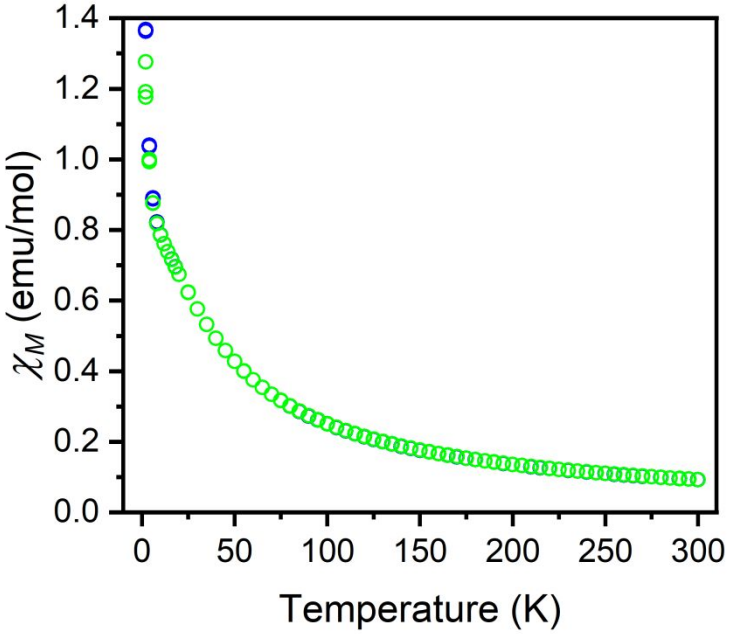

Figure S17. Field cooled (green circles) and zero-field cooled (blue circles) molar magnetic susceptibility data for **1-Dy** measured under a 0.5 T applied field.

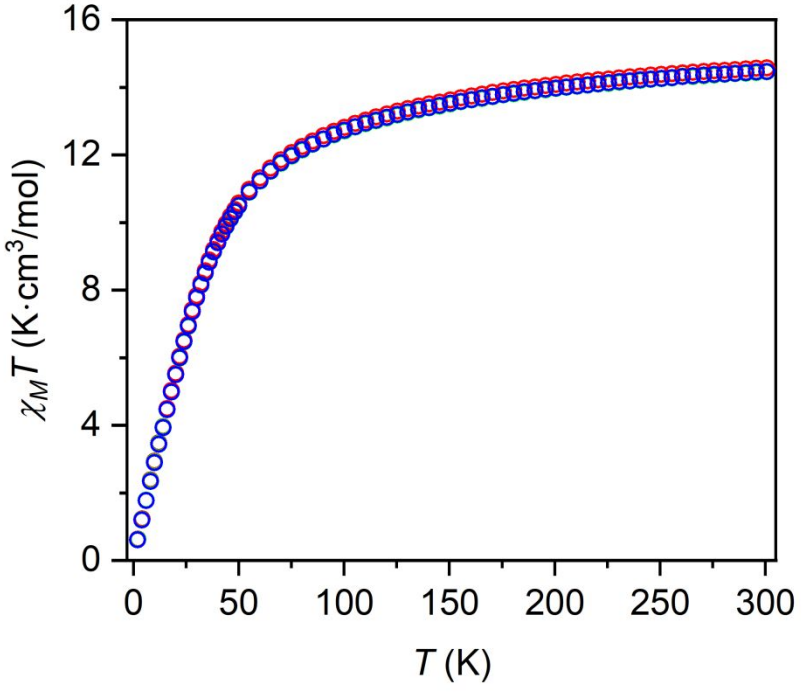

Figure S18. Dc magnetic susceptibility data for **1-Tm** measured under 0.1 T (red), 0.5 T (green) and 1 T (blue) applied fields.

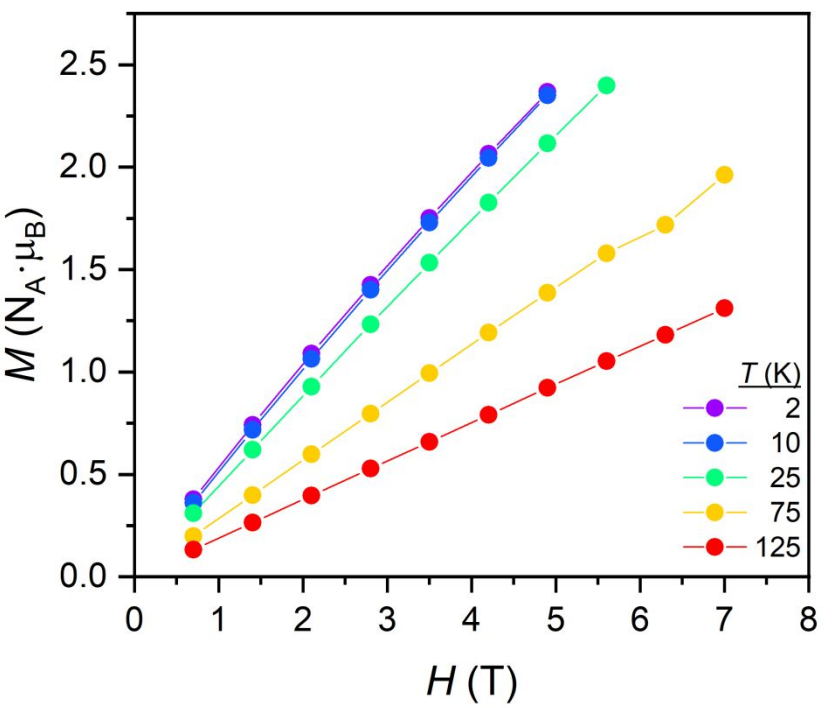

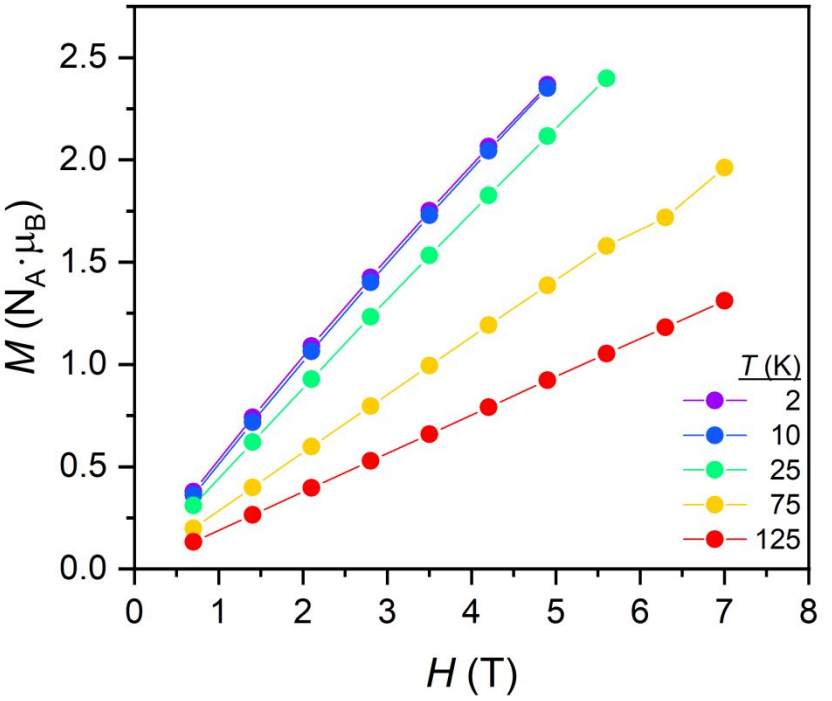

Figure S19. Isothermal magnetization data for **1-Tm**. Solid lines are guides for the eye. At 2 K and 10 K, the magnetization saturated the SQUID detector at fields higher than 4.5 T. At 25 K, the magnetization saturated the SQUID detector at fields higher than 5.5 T.

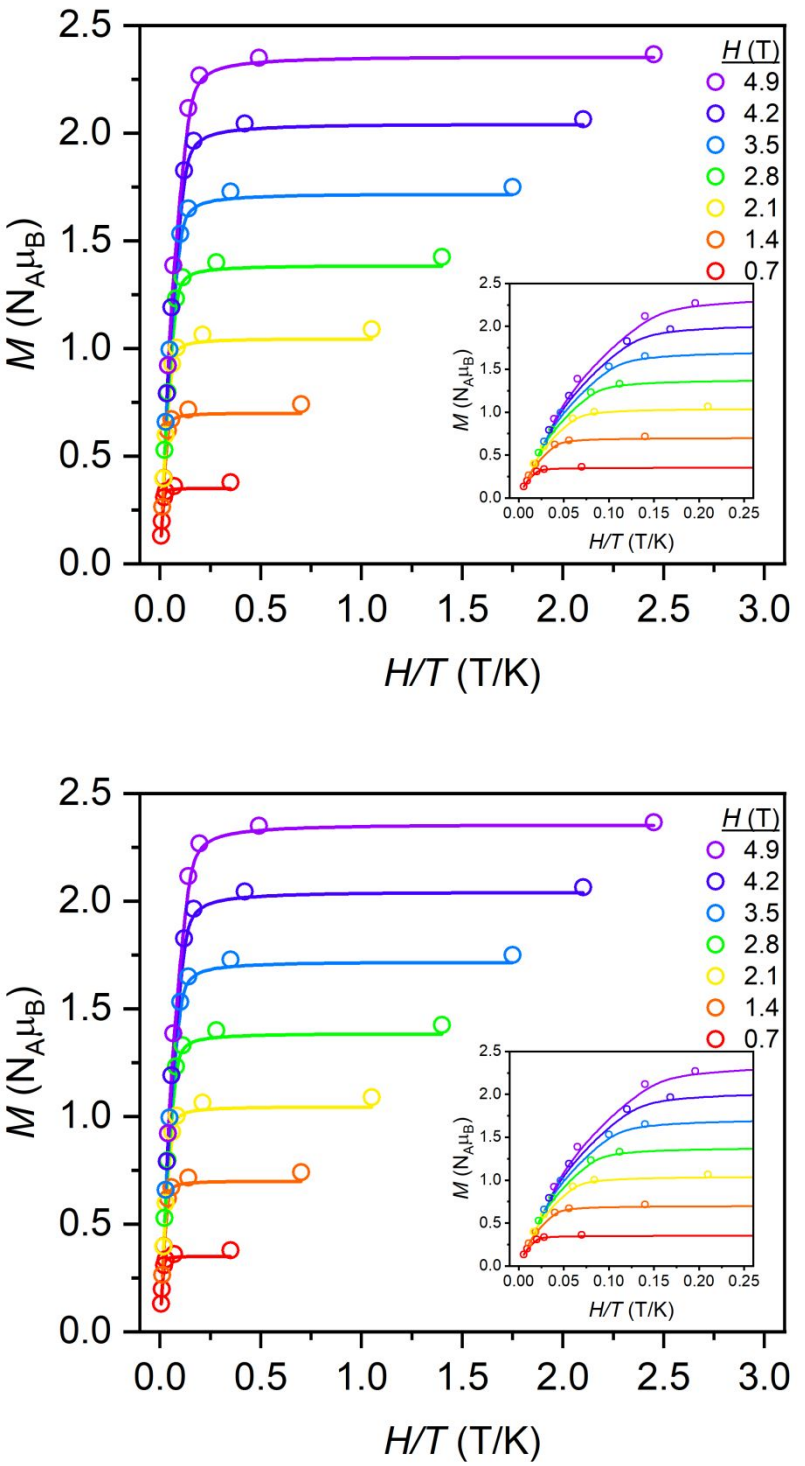

Figure S20. Reduced magnetization data for **1-Tm** collected under applied fields ranging from 0.7 to 4.9 T. Solid lines are guides for the eye.

5. NMR Spectroscopy Characterization

^{1}H and ^{13}C NMR spectra were recorded on a Bruker Avance 500 MHz spectrometer at temperatures ranging from 25 to 105 °C, and spectra were internally referenced to the residual solvent signals. The ^{89}Y NMR spectra of **1-Y** were collected at 9.4 T at various temperatures at the UC Davis NMR facility on their Avance 400 MHz instrument. Samples were dissolved in C_6D_6 or toluene-d_8 and sealed inside a J. Young NMR tube beneath an atmosphere of argon prior to measurement. C_6D_6 and toluene-d_8 were purchased from Sigma-Adrich or Cambridge Isotope Laboratories, saturated with argon using three freeze-pump-thaw cycles, and dried for 72 h over 3 Å molecular sieves prior to use.

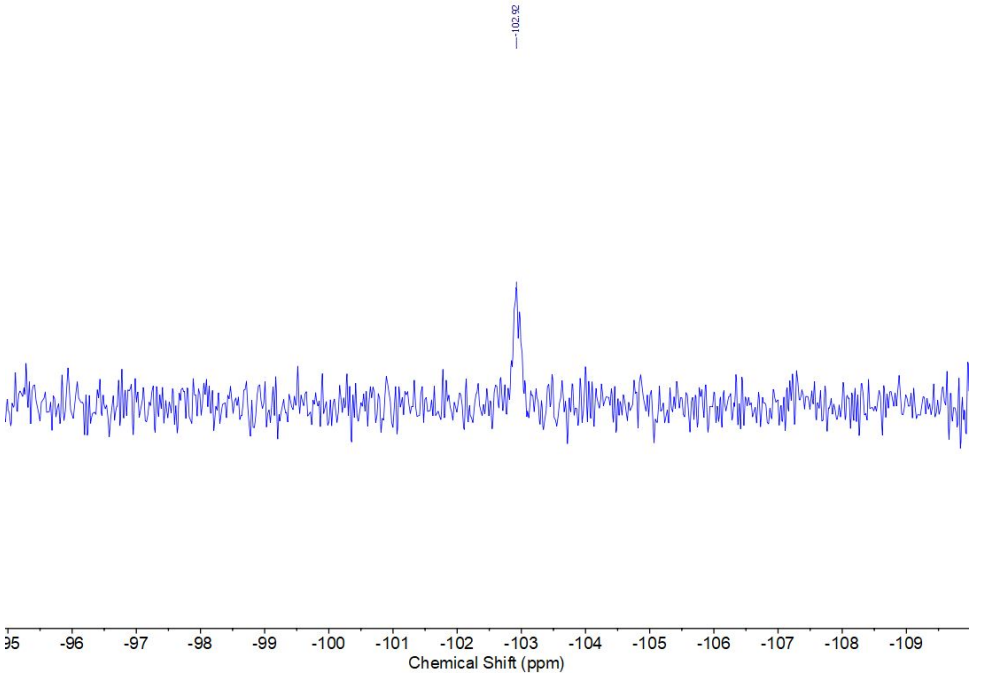

Figure S21. ^{89}Y NMR spectrum of **1-Y** in C_6D_6 collected at 25 MHz at 25 °C.

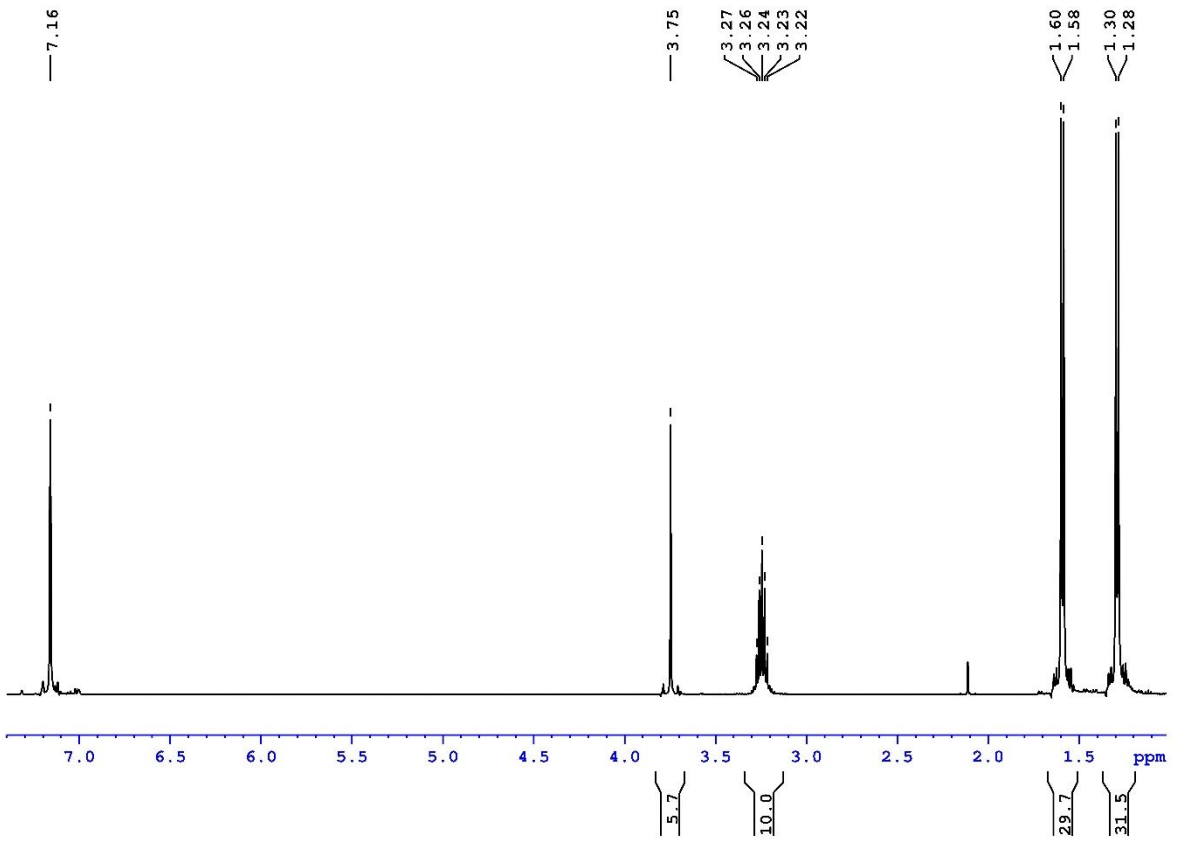

Figure S22. ^{1}H NMR spectrum of **1-Y** in C_6D_6 collected at 25 °C.

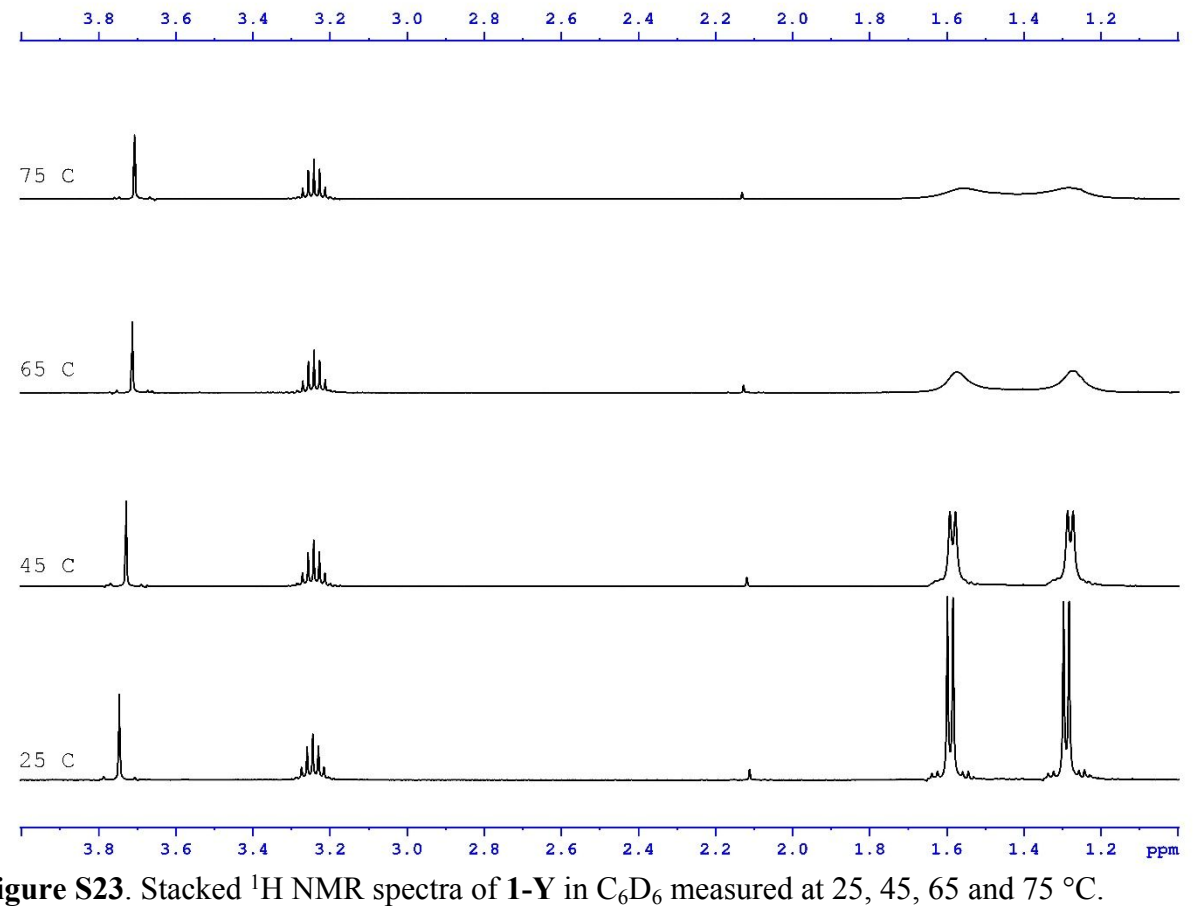

Figure S23. Stacked ^{1}H NMR spectra of **1-Y** in C_6D_6 measured at 25, 45, 65 and 75 °C.

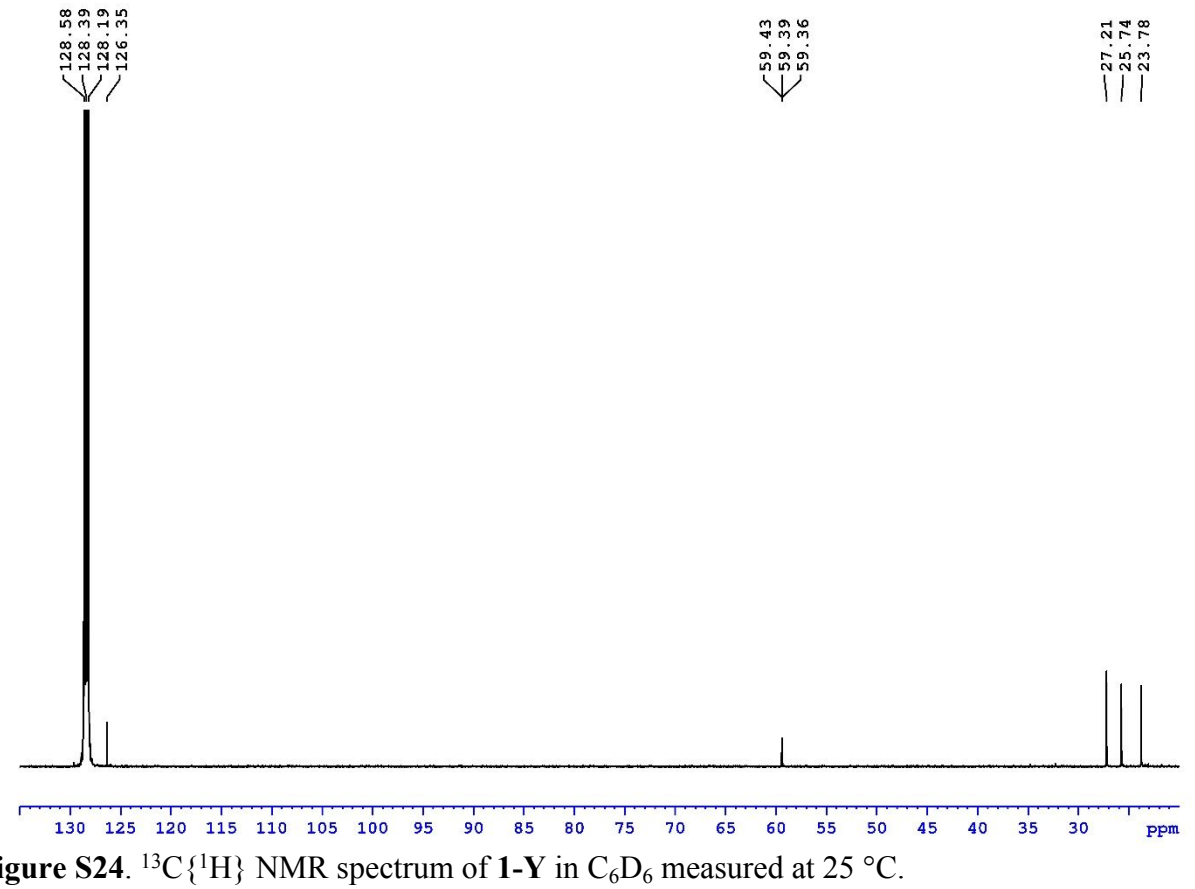

Figure S24. $^{13}C\{^{1}H\}$ NMR spectrum of **1-Y** in C_6D_6 measured at 25 °C.

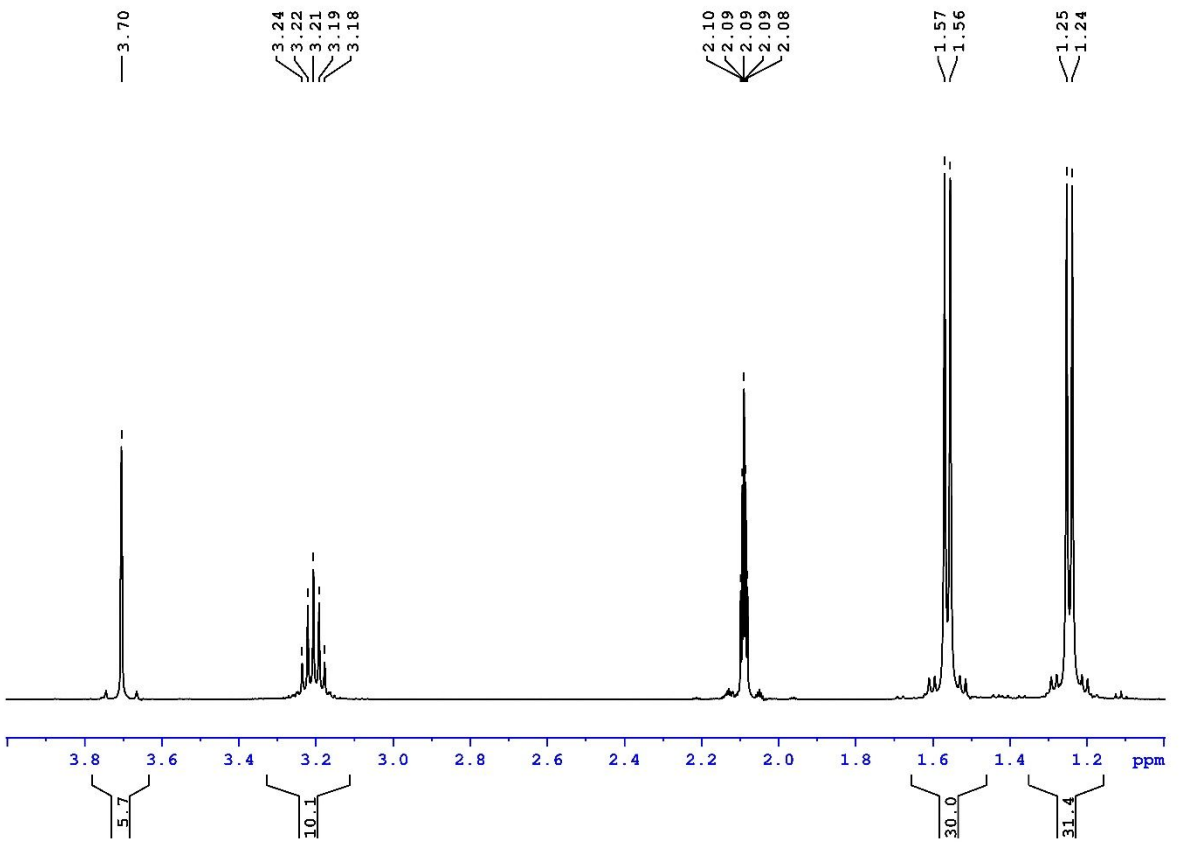

Figure S25. ^{1}H NMR spectrum of **1-Y** in toluene-d_8 measured at 25 °C.

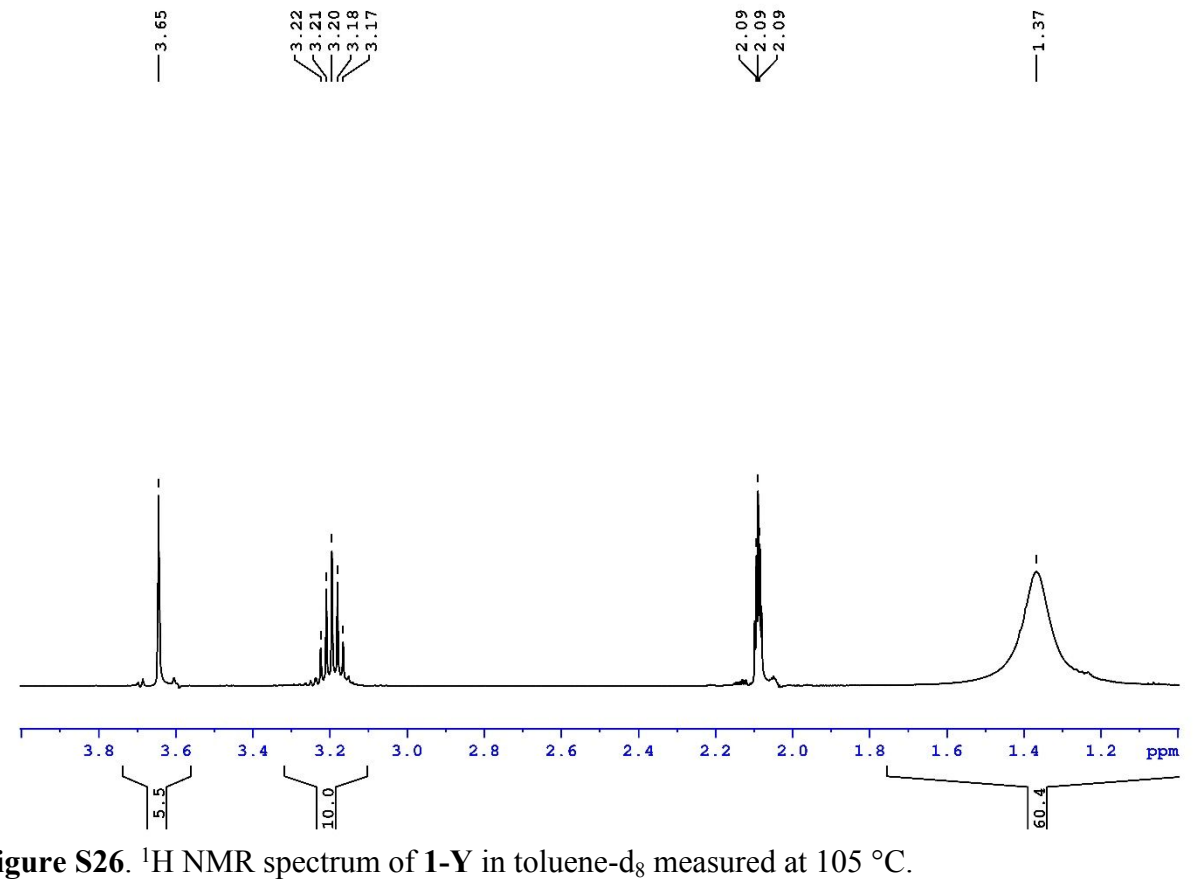

Figure S26. ^{1}H NMR spectrum of **1-Y** in toluene-d_8 measured at 105 °C.

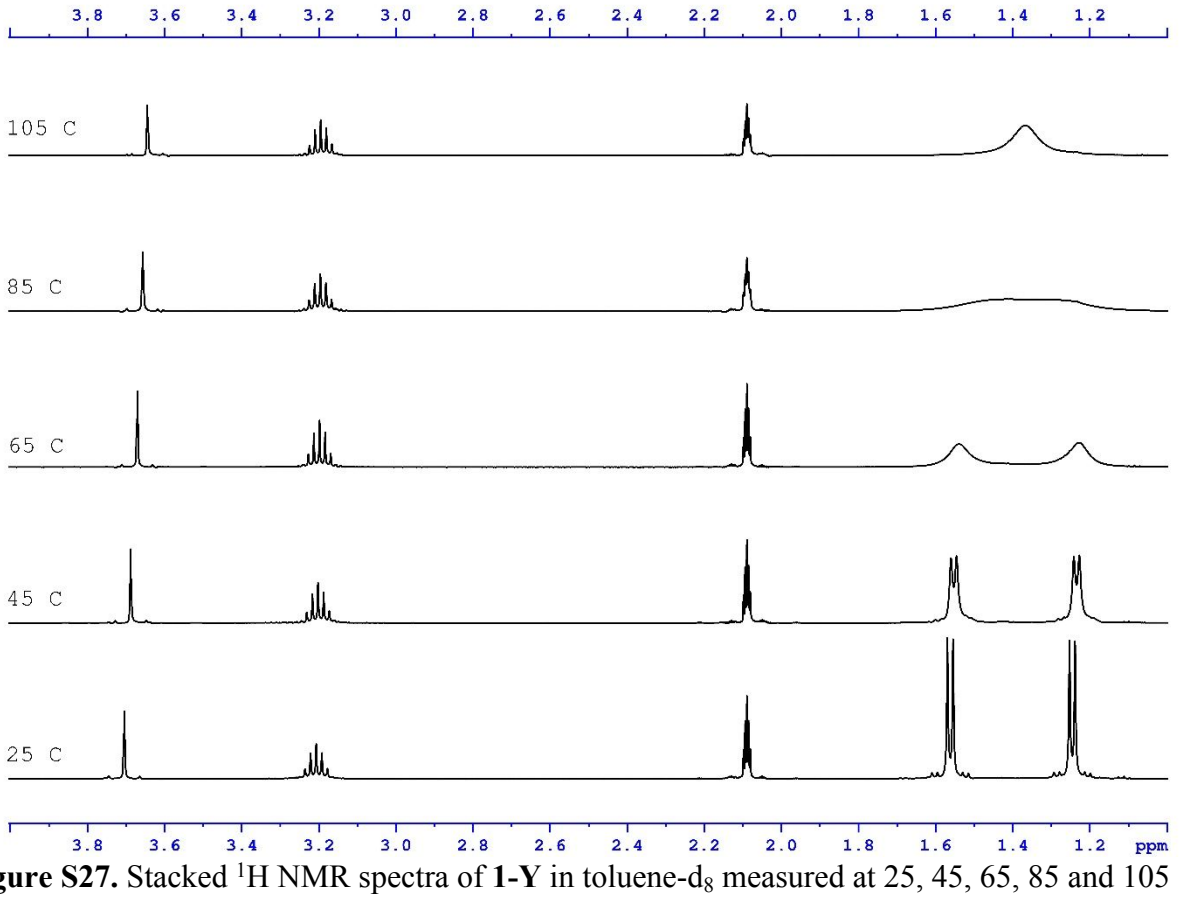

Figure S27. Stacked ^{1}H NMR spectra of **1-Y** in toluene-d_8 measured at 25, 45, 65, 85 and 105 °C.

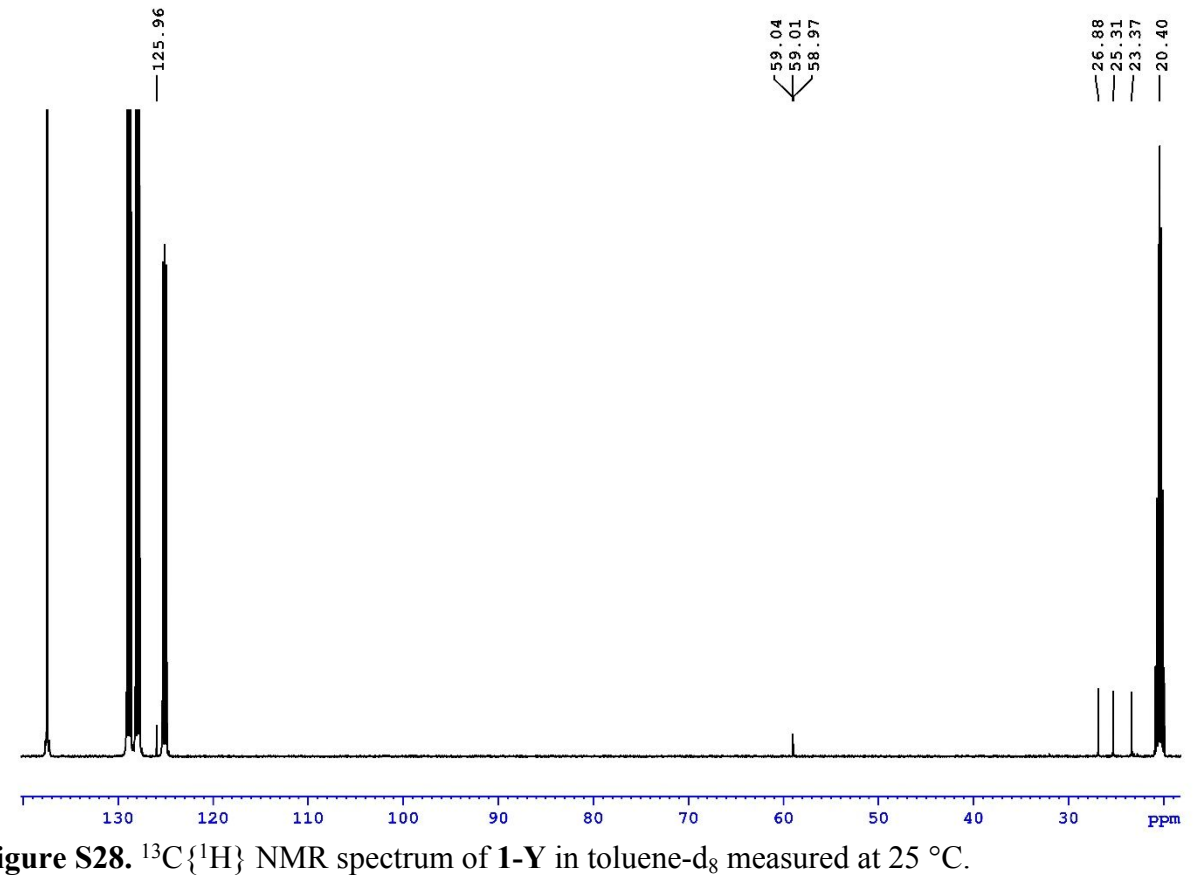

Figure S28. $^{13}C\{^{1}H\}$ NMR spectrum of **1-Y** in toluene-d_8 measured at 25 °C.

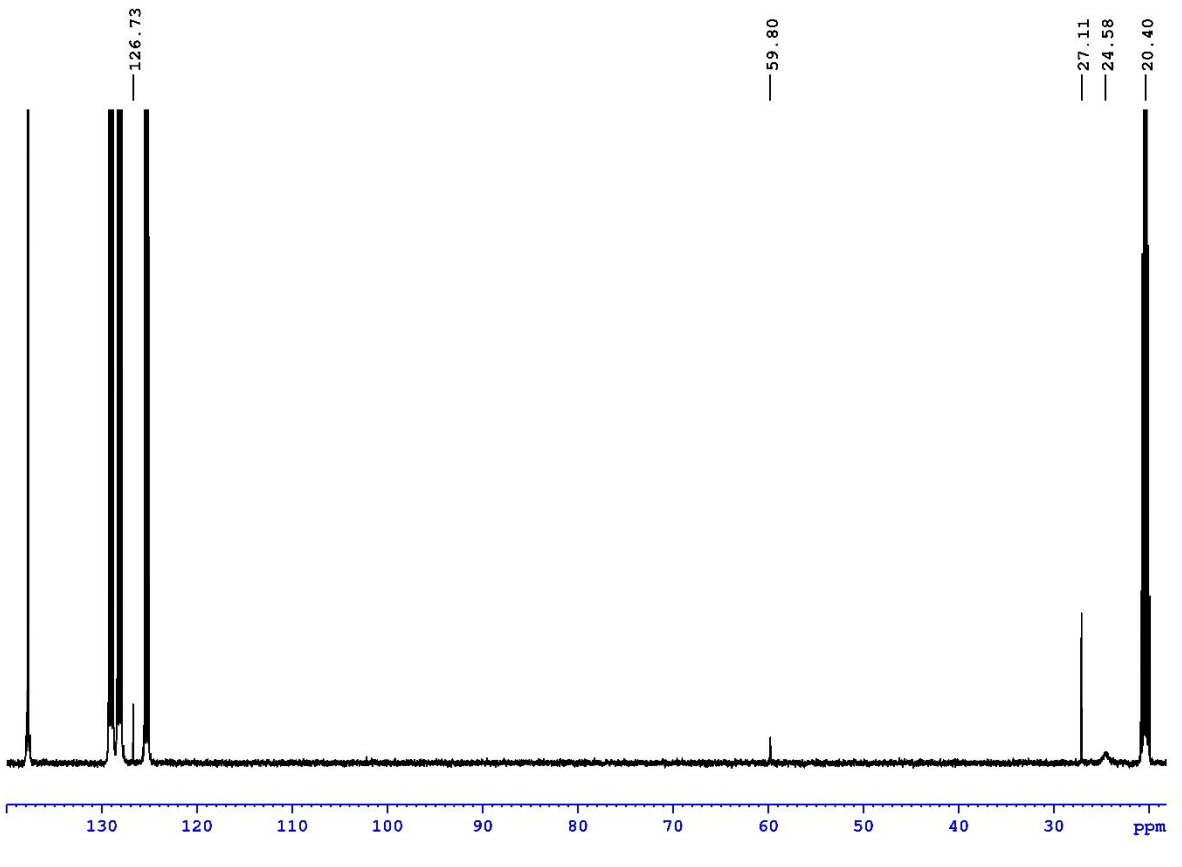

Figure S29. $^{13}C\{^{1}H\}$ NMR spectrum of **1-Y** in toluene-d_8 measured at 105 °C.

6. UV-Vis-NIR Spectroscopy

All UV-Vis spectra were collected on n-hexane solutions sealed within J. Young adapted cuvettes under an inert atmosphere of argon at ambient temperature (25 °C). A Varian Cary 5000 spectrometer was used for all samples. Beer's law linear regressions were produced using OriginPro.

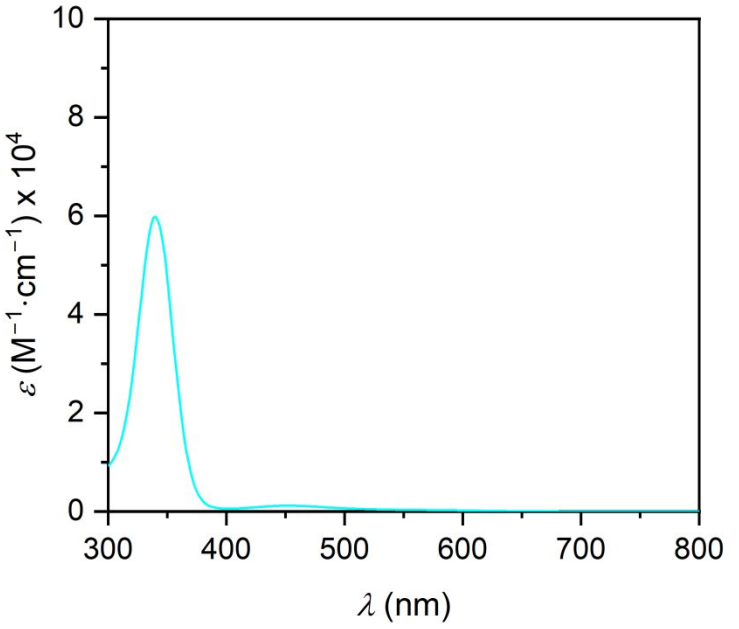

Figure S30. UV-vis spectrum of an n-hexane solution of **1-Y**.

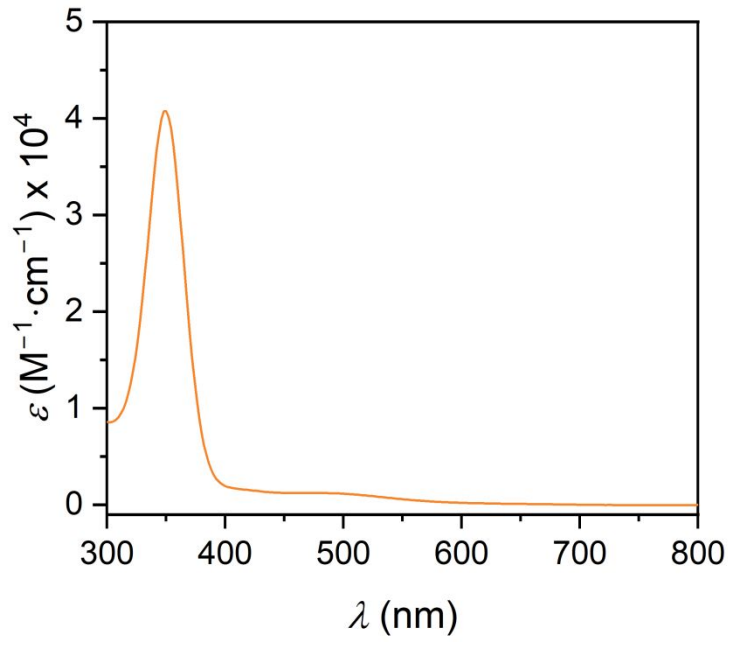

Figure S31. UV-vis spectrum of an n-hexane solution of **1-Gd**.

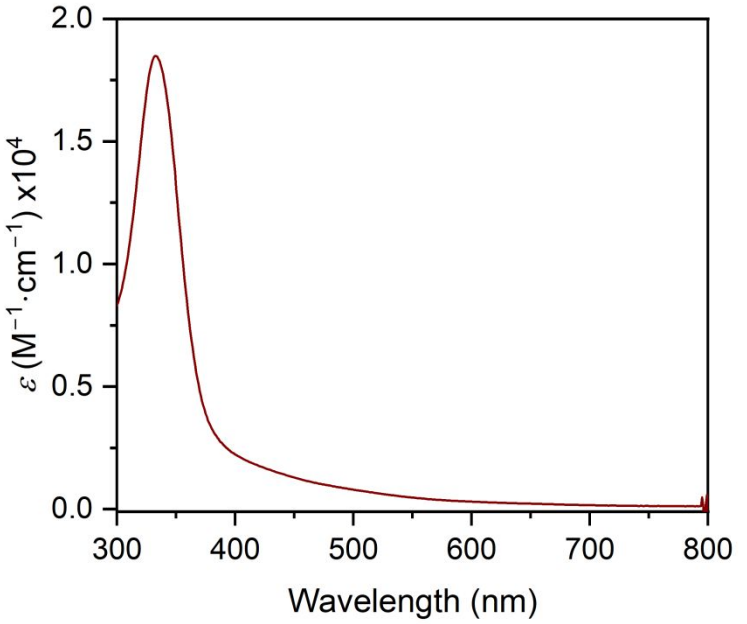

Figure S32. UV-vis Spectrum of an n-hexane solution of **1-Tb**.

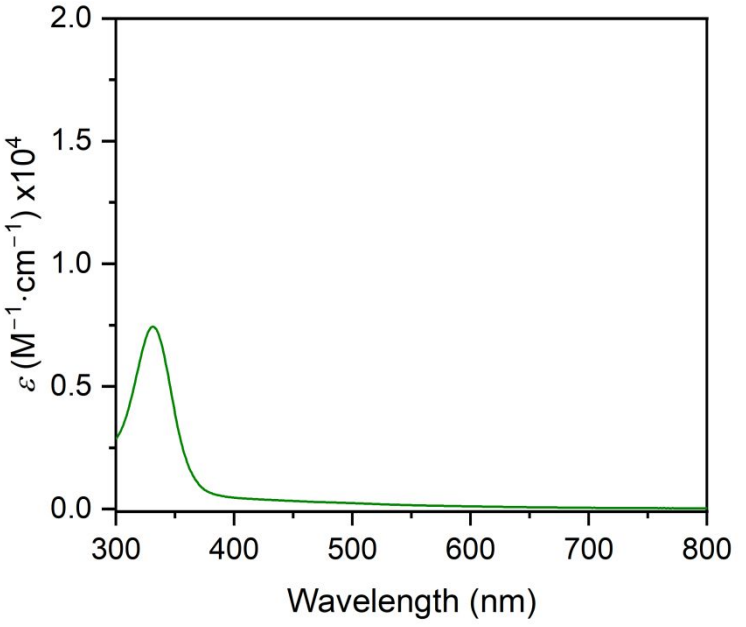

Figure S33. UV-vis spectrum of an n-hexane solution of **1-Dy**.

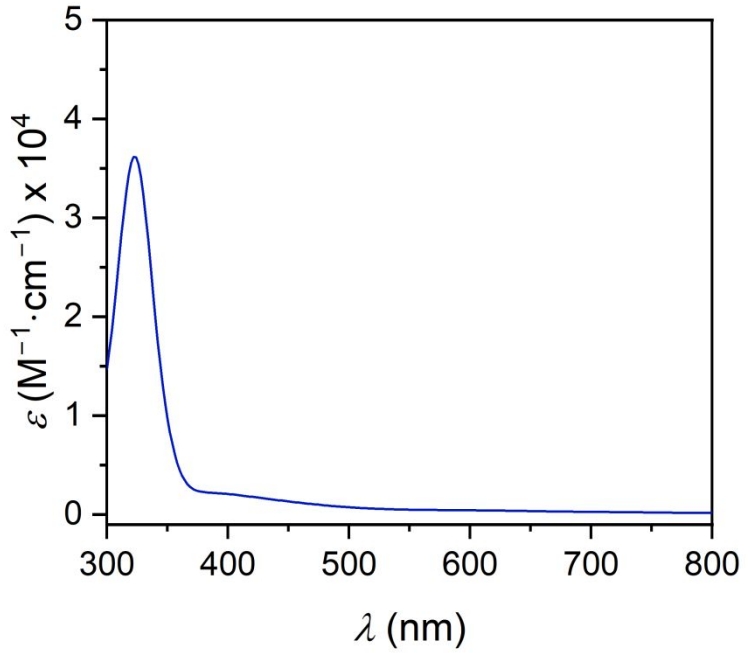

Figure S34. UV-vis spectrum of an n-hexane solution of **1-Tm**.

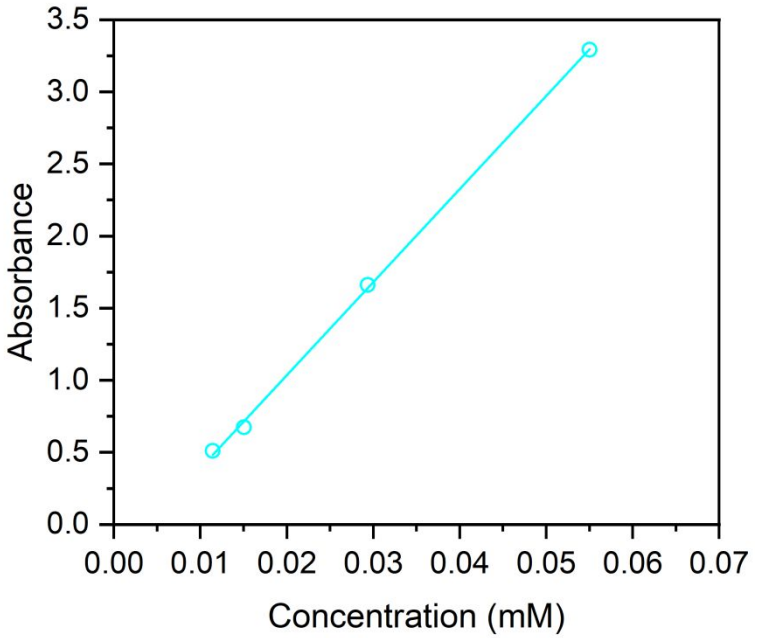

Figure S35. Beer's law plot for the feature at 340 nm in the UV-vis spectrum of **1-Y**. Circles correspond to experimental absorption maxima and the line represents the fit to the equation: $A = \varepsilon lM + b$; $\varepsilon = 64500 \pm 600$ M^{-1}·cm^{-1}, $b = -0.25$.

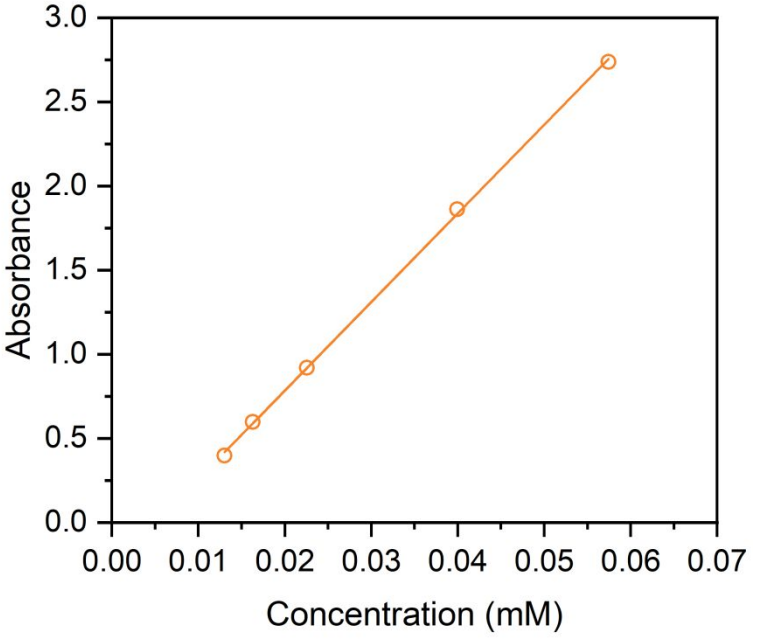

Figure S36. Beer's law plot for the absorption at 350 nm in the UV-vis spectrum of **1-Gd**. Circles correspond to absorption maxima, line corresponds to fit to: $A = \varepsilon lM + b$. $\varepsilon = 52700 \pm 600$ $M^{-1} \cdot cm^{-1}$, $b = -0.26$

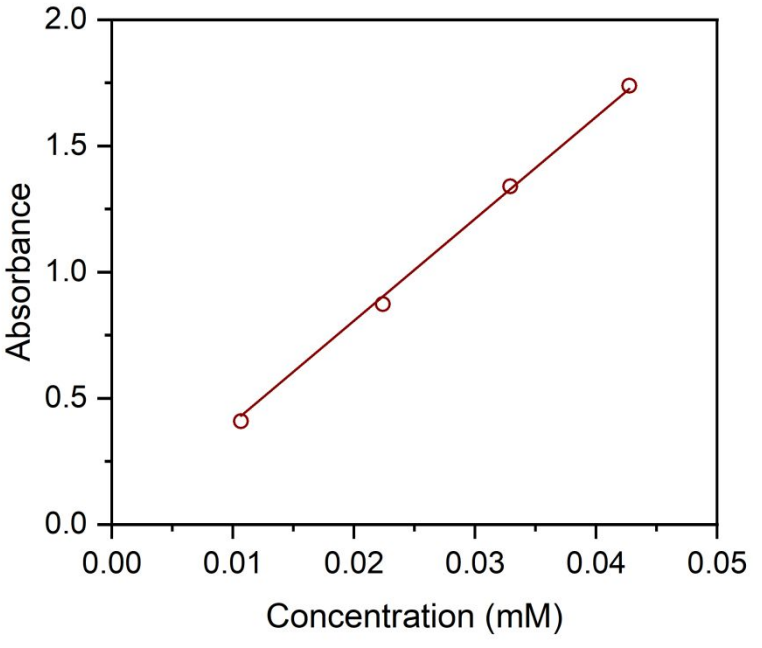

Figure S37. Beer's law plot for the absorption at 332 nm in the UV-vis spectrum of **1-Tb**. Circles correspond to absorption maxima, line corresponds to fit to: $A = \varepsilon lM + b$. $\varepsilon = 40400 \pm 400$ $M^{-1} \cdot cm^{-1}$, $b = 0$

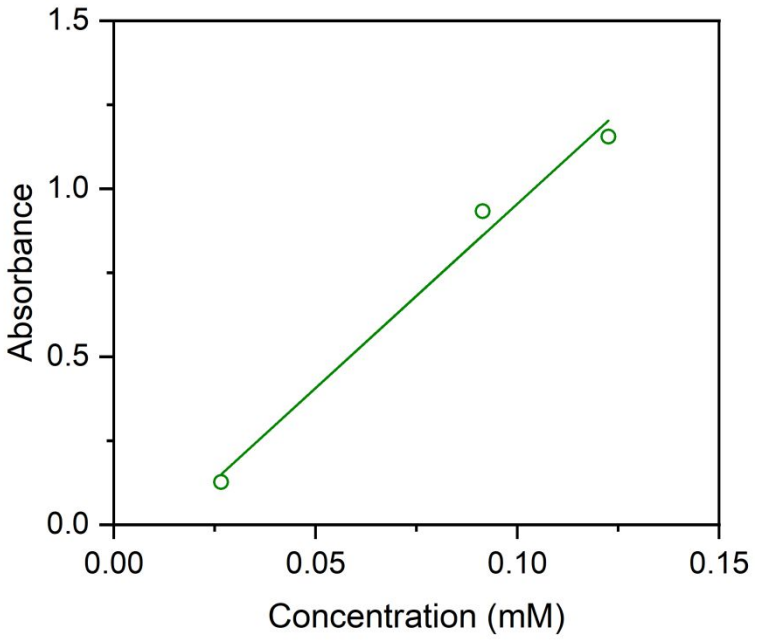

Figure S38. Beer's law plot for the absorption at 331 nm in the UV-vis spectrum of **1-Dy**. Circles correspond to absorption maxima, line corresponds to fit to: $A = \varepsilon lM + b$. $\varepsilon = 11000 \pm 1300\ M^{-1}\cdot cm^{-1}$, $b = -0.14$

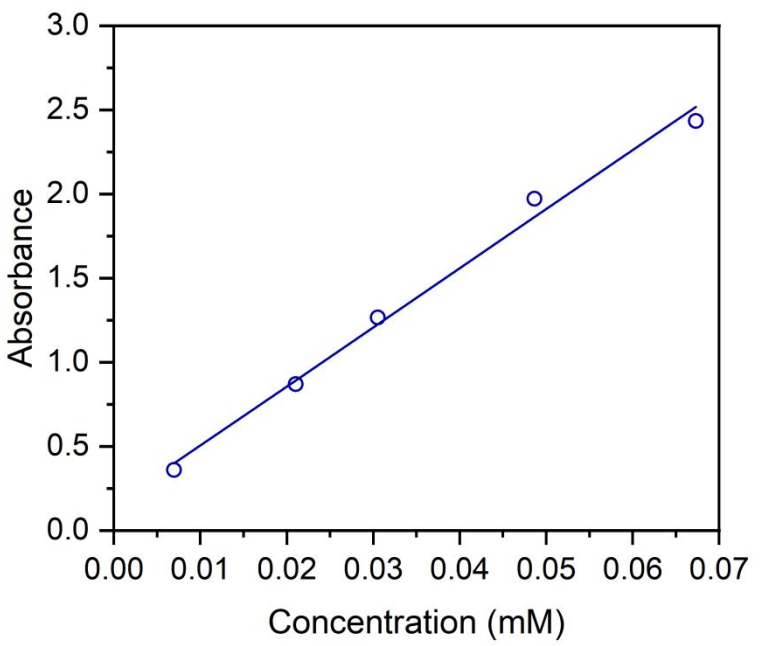

Figure S39. Beer's law plot for the absorption at 320 nm in the UV-vis spectrum of **1-Tm**. Circles correspond to absorption maxima, line corresponds to fit to: $A = \varepsilon lM + b$. $\varepsilon = 35000 \pm 1800\ M^{-1}\cdot cm^{-1}$, $b = 0.15$

Table S10. Summary of the Beer's Law regression analysis for solutions of **1-Ln** with parenthesized uncertainties.

Compound	ε ($M^{-1}\cdot cm^{-1}$)	λ (nm)
1-Y	64500(600)	340
1-Gd	52700(600)	350
1-Tb	40400(400)	332
1-Dy	11000(1300)	331
1-Tm	35000(1800)	320

7. Infrared Spectra for 1-Ln

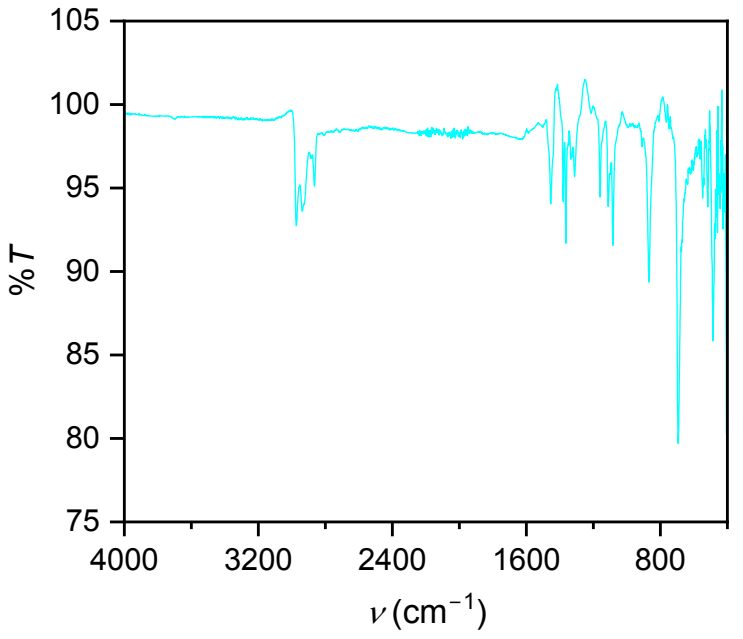

Figure S40. Fourier transform infrared spectrum of **1-Y**.

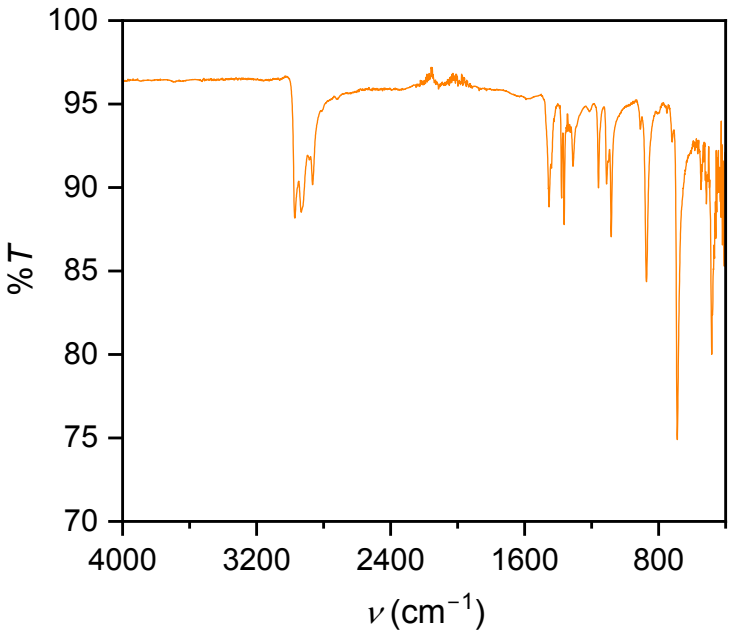

Figure S41. Fourier transform infrared spectrum of **1-Gd**.

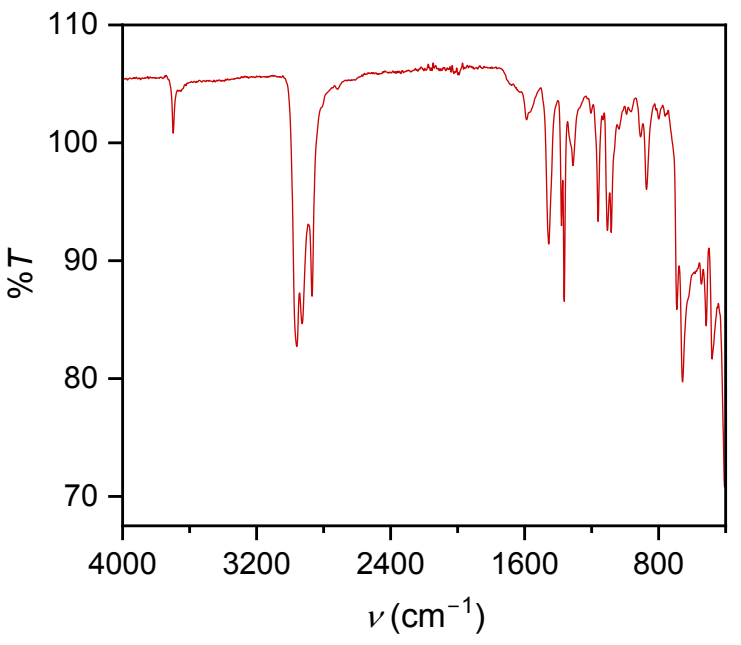

Figure S42. Fourier-transform infrared spectrum of **1-Tb**.

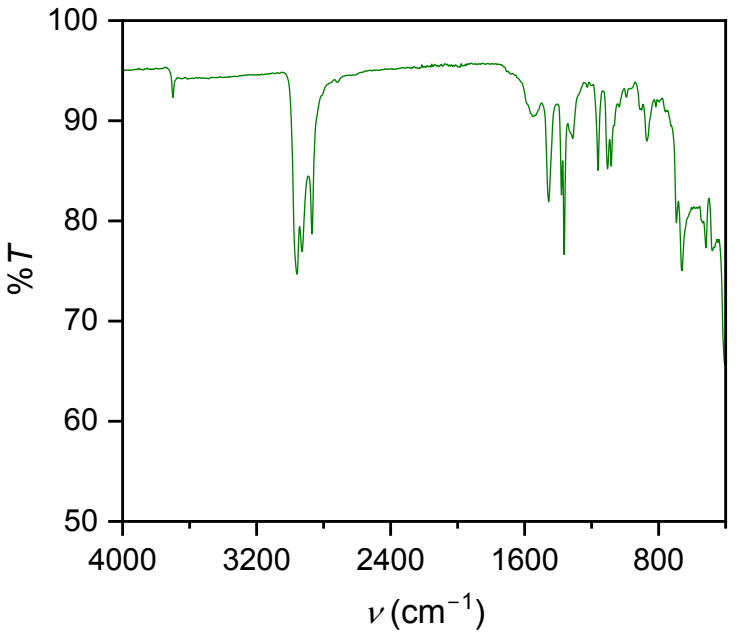

Figure S43. Fourier-transform infrared spectrum of **1-Dy**.

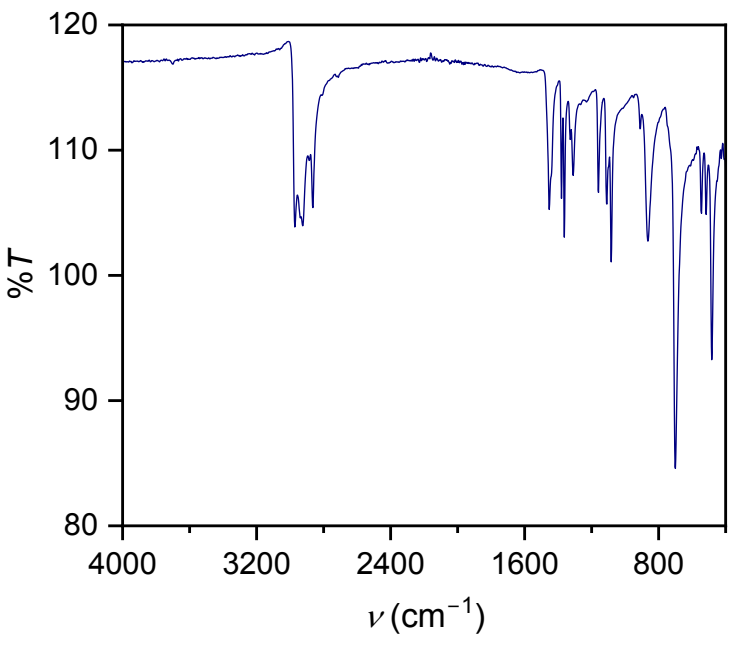

Figure S44. Fourier-transform infrared spectrum of **1-Tm**.

8. MALDI-ToF Mass Spectra for 1-Ln

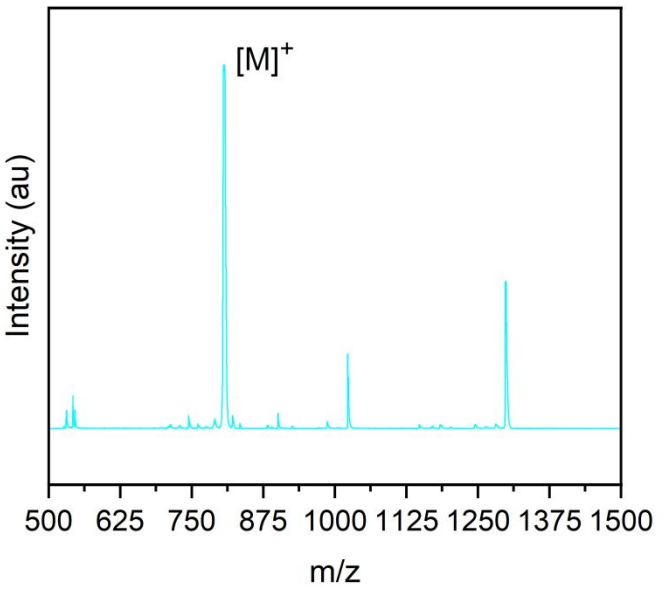

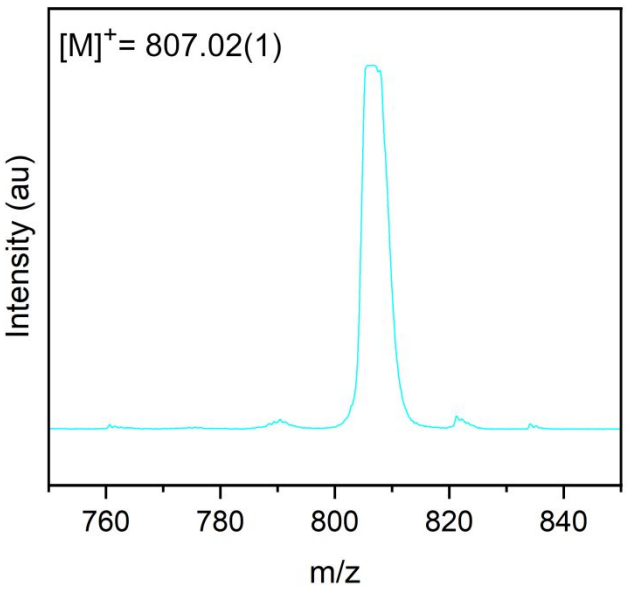

Figure S45. MALDI-ToF mass spectrum of **1-Y**.

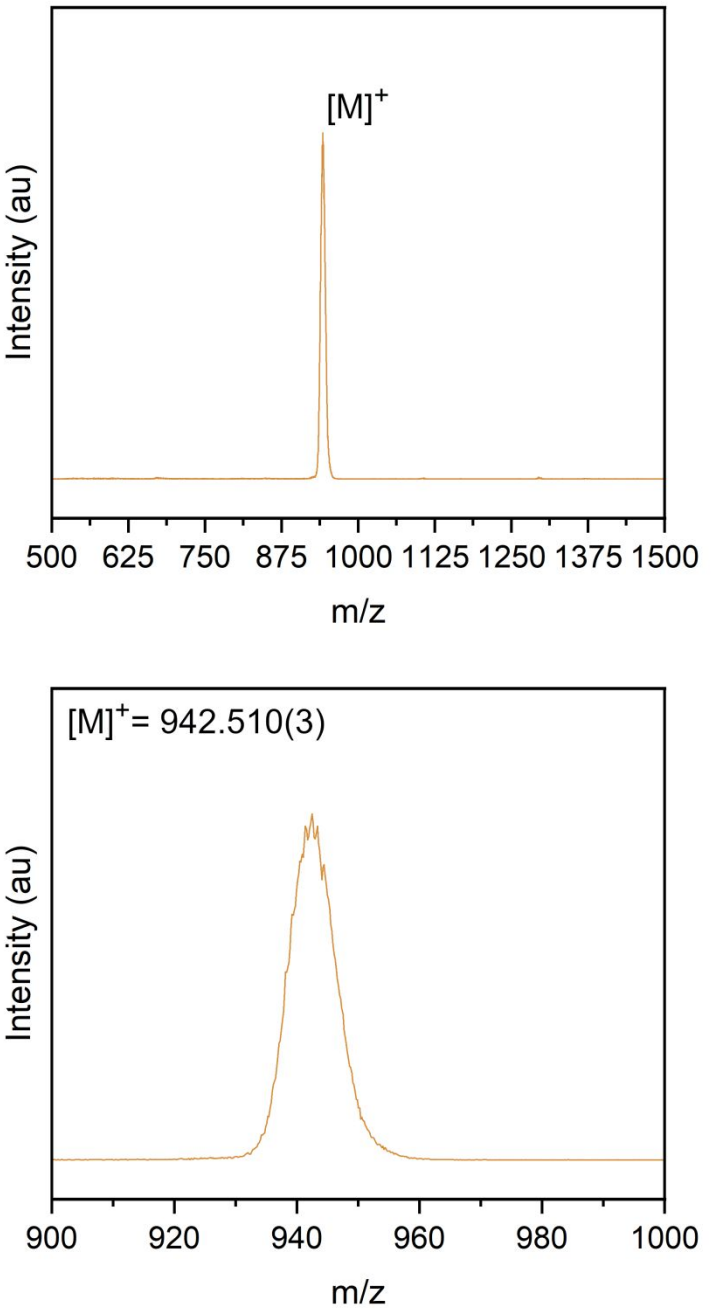

Figure S46. MALDI-ToF mass spectrum of **1-Gd**.

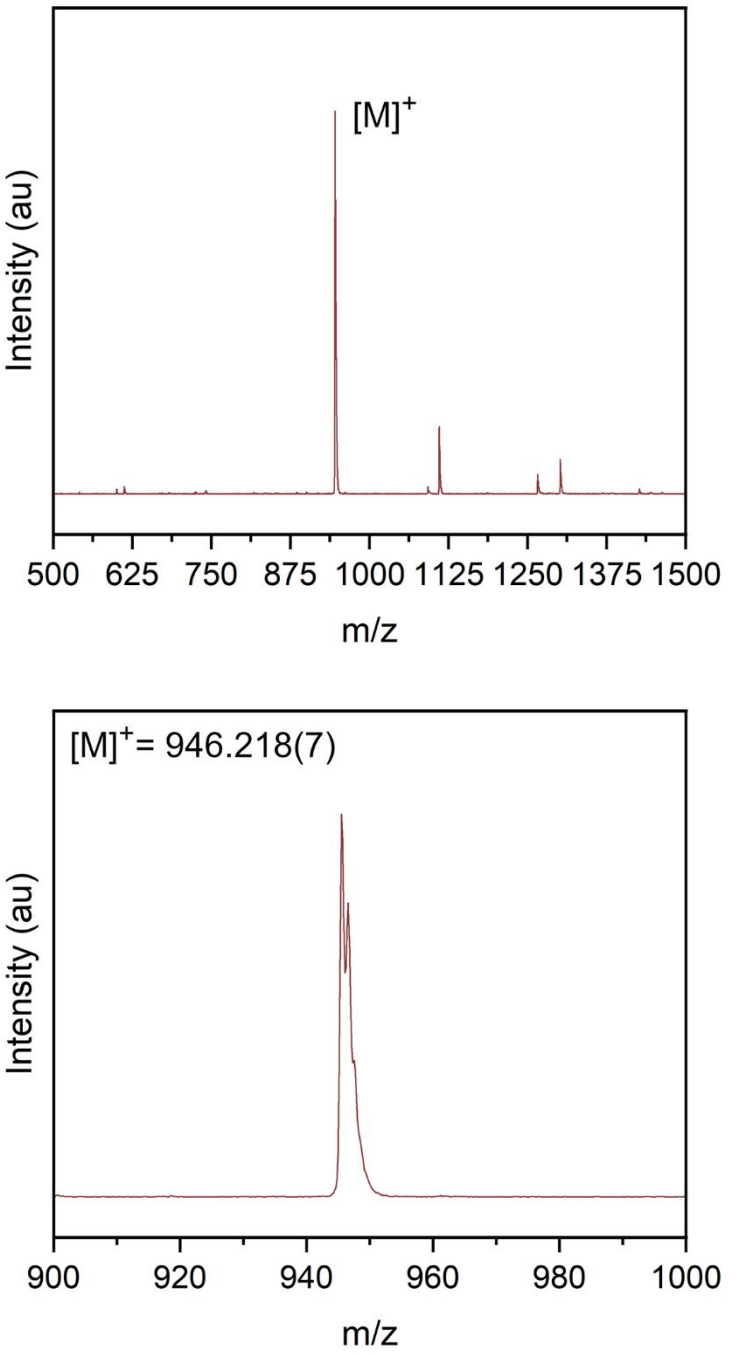

Figure S47. MALDI-ToF mass spectrum of **1-Tb**.

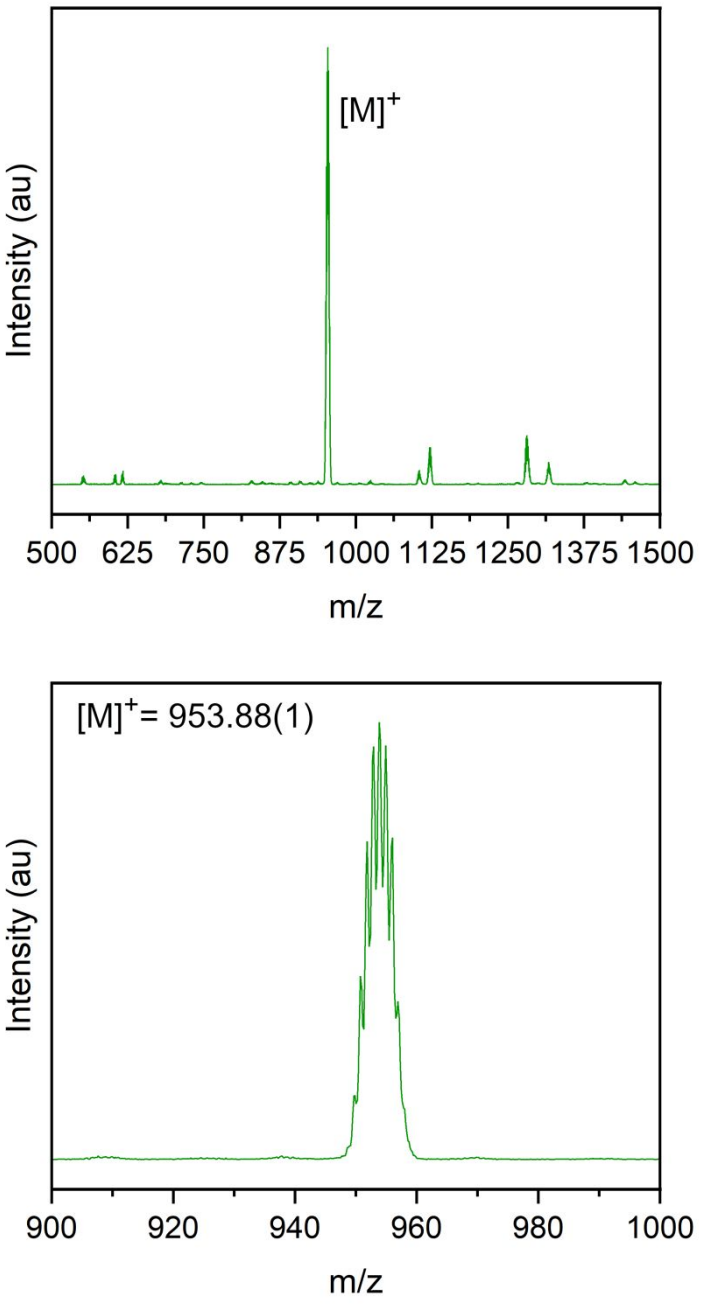

Figure S48. MALDI-ToF mass spectrum of **1-Dy**.

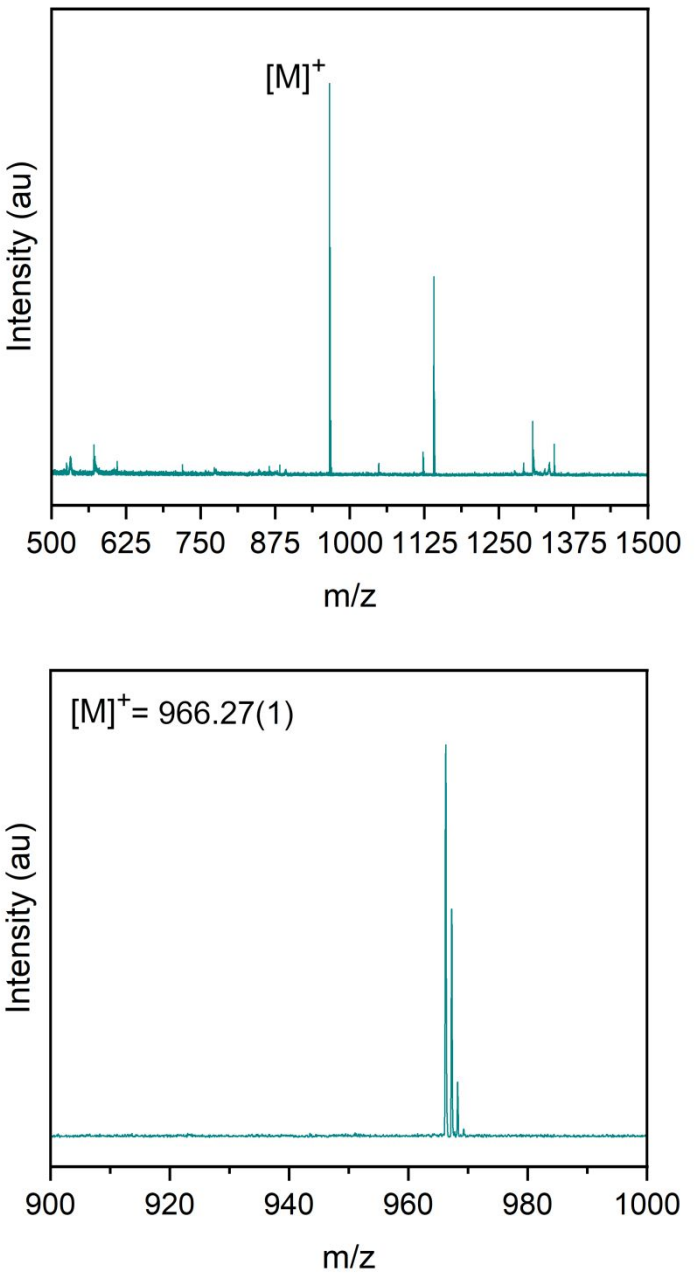

Figure S49. MALDI-ToF mass spectrum of **1-Tm**.

9. Density Functional Theory Calculations

In order to determine the ground state and optimized structures of $(Cp^{iPr5}Ln)_2(\mu\text{-}\eta^6\text{:}\eta^6\text{-}C_6H_6)$ complexes (**1-Ln**; Ln = Y, Gd, Tb, Dy, Tm), density functional theory (DFT) calculations were initially conducted in the gas phase. Geometry optimizations were performed on structures obtained from single crystal x-ray diffraction data, using C_1 symmetry. The TPSSh hybrid meta-Generalized Gradient Approximation (meta-GGA) density functional,[5] including Grimme's D3 dispersion correction[6] with a Becke-Johnson damping function,[7] and the Resolution of Identity (RI-*J*) approximation,[8] were employed. The practicality of the TPSSh hybrid functional for lanthanide complexes, particularly those with small HOMO-LUMO gaps, has been demonstrated in previous studies.[23] For C and H atoms, the double-ζ split valence basis set with polarization functions (def2-SVP)[10] was used, while the triple-ζ basis set with polarization functions (def2-TZVP)[11] was employed for the metallic atoms. Stuttgart-Cologne scalar-relativistic small core effective core potentials (ECPs)[12] were also included for these metallic atoms. A lanthanide molecular complex can exhibit degeneracy in its various 4f configurations due to the contracted nature of the 4f orbitals. Therefore, small core ECPs were utilized to explicitly treat 4f electrons, as opposed to 4f-in-core ECP calculations, which are necessary to determine the appropriate 4f configuration for lanthanide complexes with near-degenerate f-occupations. The convergence tolerances for geometry and electron density were set to 10^{-4} a.u. and 10^{-7}, respectively. Quadrature grids of size 4[13] were employed for numerical integration. The optimized structures were confirmed as minima on their respective ground-state potential energy surfaces through harmonic vibrational analysis. [14]

All spin multiplicities corresponding to M^{2+}/Bz^{2-} and M^{3+}/Bz^{4-} in **1-Ln** complexes were explored. Electronic configurations, including $4f^{n+1}$ and $4f^n$, indicative of the oxidation states of the metals, as well as unconventional configurations involving d orbitals, were assessed. Achieving self-consistent field (SCF) convergence for many of these electronic occupations was extremely challenging. Nevertheless, Fermi smearing, in conjunction with SCF damping and level shifting, was employed to attain specific electronic configurations. These techniques have proven effective for other open-shell lanthanide complexes[23] with shallow potential energy surfaces in facilitating SCF convergence. Fermi smearing with the following settings was employed to obtain the specific electronic occupations of the valence shell including $4f^{n+1}$ and $4f^n5d^1$ for the lanthanide complexes. The initial temperature was set between 2000–3000 K, and the final temperature to be between 50–150 K with an annealing factor of 0.85 to ensure the desired electronic configuration. The occupation numbers were fixed during Fermi smearing to achieve the specified spin state. Ground-state optimization was then carried out for all the possible electronic configurations describing different spin states (various numbers of unpaired electrons (Ne^-)) for each complex.

All-electron calculations using the scalar-relativistic exact two-component (X2C-SR)DFT optimizations[39,40] were further performed on the ECP-optimized lanthanide compounds (Ln = Gd, Tb, Dy, Tm) in the singlet state. The diagonal local approximation to the unitary decoupling transformation (DLU) was employed.[41,42] Segmented-contracted x2c-type basis sets[43] including x2c-TZVPall-2c and x2c-SVPall-2c were used for the metals and nonmetallic atoms, respectively. Additionally, the finite nucleus model was utilized.[44,45] The same functional and dispersion correction choices from the ECP computations were employed in the X2C computations. Grids with an increased number of radial points (gridsize 5a) were used.[45]

The solvation effects of hexane on the lanthanide complexes were accounted for using the conductor-like screening implicit solvation model (COSMO)[31] with a dielectric constant of E =

1.887 and an index of refraction $n = 1.3727$. The structures obtained with COSMO were confirmed to be local minima through vibrational analysis. Time-dependent density functional theory (TDDFT)[29] computations with the nonorthonormal Krylov subspace method[30] were carried out to simulate the UV-Vis spectra and investigate the nature of observed experimental transitions. These computations involved 180–200 vertical excitations on the optimized structures in the liquid phase, using the same functional and choice of basis sets as previously described. Electronic absorption spectra were computed using a Gaussian spectral line shape with a half-width at half maximum (HWHM) of 0.2 eV, centered on the excitation energy.

All calculations were performed using the TURBOMOLE quantum chemistry package (version 7.7).[32] For the visualization of the orbitals, the VMD program with a contour value of 0.03 was used.[33]

It is important to note that DFT calculations using ECPs found an energy minimum corresponding to a singlet ground state **1-Gd**(g). However, the Gd···Gd distance in the **1-Gd**(g) model is 4.448 Å, which is 0.38 Å longer than the metal···metal distance observed in the crystal data, yet it is the closest to the experimental data when compared with the calculated metal···metal distances for the other states obtained with ECPs. Efforts to achieve a singlet ground state using ECPs, where the structural parameters of **1-Gd** align with the x-ray data within the error margin of our methodology, were unsuccessful. We attempted computations with larger basis sets, such as def2-TZVP for the entire system, or tried different initial guesses starting from states with higher spin multiplicities, but no significant improvement was observed. Consequently, all-electron calculations using the scalar-relativistic exact two-component (X2C-SR) approach were employed to optimize **1-Gd**(g), which resulted in excellent agreement with experimental data (see Table 3 and Table S15). To maintain consistency, singlet states of other **1-Ln** lanthanide complexes were also optimized using the X2C-SR method and are reported below in addition to the ECPs results. However, it is worth noting that the results for **1-Tb** and **1-Dy** obtained from ECPs and X2C-SR (see Tables S19 and S23) are both in agreement with the experimental data. Therefore, these results raise concerns about the accuracy of small-core ECP parameters for Gd metal[17]. The singlet states of **1-Ln** obtained from the X2C-SR optimization are the focus of the discussion in the main text.

Natural population analyses (NPA)[46] of the ground-state **1-Ln** molecular complexes are presented in Table S31 (total density) and Table S32 (spin density). The spin state of the benzene in each spin state of **1-Ln** (refer to Tables S11, S15, S19, S23, S27) is determined from the NPA analysis by summing the spin contributions of each atom in the benzene ring.

Table S11. Selected structural and electronic properties of **1-Y** calculated using TPSSh, def2-TZVP/ECP basis set for Y, and def2-SV(P) basis sets for C and H. The ground state is highlighted in peach. Below, Ne^- is the number of unpaired electrons defined for the complex; S is the total spin state of the compound; ΔE (eV) shows the energy difference with respect to the lowest energy; C–C(avg) is the average C–C bond distance of benzene; Y–Bz and Y–Cp are the metal benzene and metal Cp centroid distances (Å), respectively; Cp1–Bz–Cp2 is the angle (°) formed by the centroids of each Cp and the Bz ring. The Bz spin is the spin state of benzene and $\langle S^2 \rangle$ is the expectation value of the S^2 operator.

Structure	Ne^-	S	ΔE (eV)	C–C(avg) (Å)	Y–Bz (Å)	Cp1–Bz–Cp2	Y–Cp(Å)	Bz spin	$\langle S^2 \rangle$
(a)	0	0	0	1.472	1.982	174.3	2.351	0	0
(b)	2	1	1.56	1.455	2.112	170.2	2.329	0.60	2.01
(c)	4	2	2.69	1.437	2.250	174.8	2.333	1.16	6.01

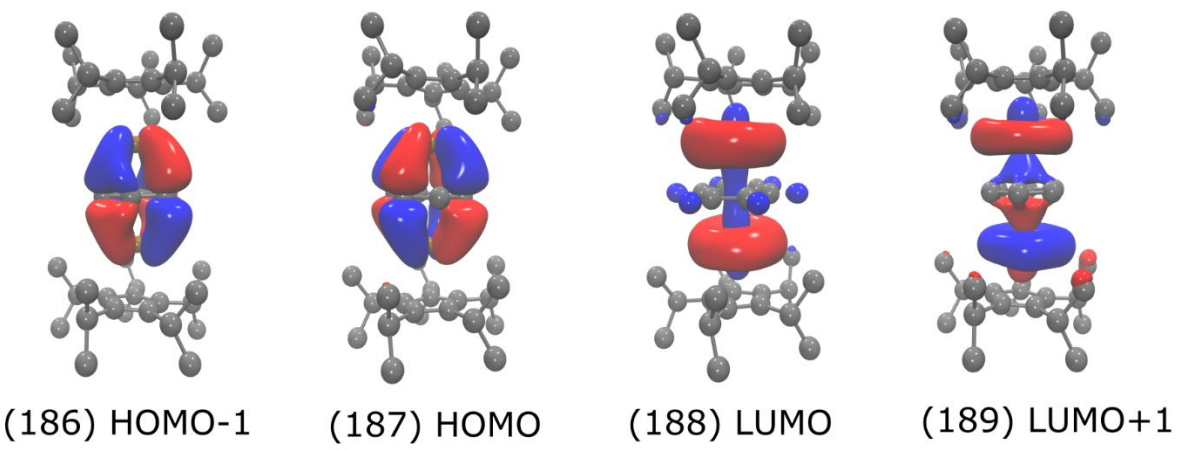

Figure S50. Molecular orbital plots of the singlet **1-Y**(a). Hydrogen atoms are omitted for clarity, and a contour value of 0.03 was used in the orbital depictions.

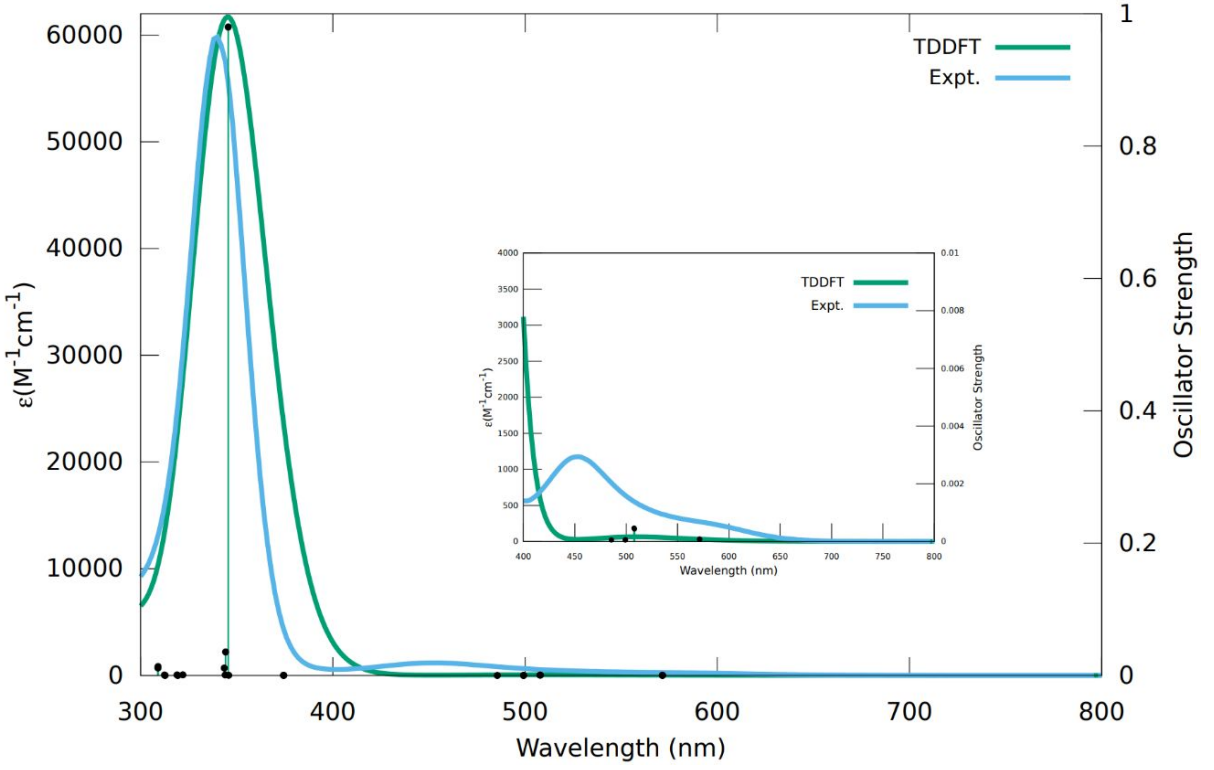

Figure S51. UV-Vis spectral comparison for **1-Y**. Experimental and simulated spectra of singlet **1-Y**(a) computed with TDDFT using TPSSh and COSMO solvent model. A Gaussian spectral lineshape with a width of 0.2 eV was used.

Table S12. Molecular orbital energies and Mulliken population analysis of singlet **1-Y**(a) complex. The % metal character identifies the overall metal contribution from both Y centers combined to the molecular orbital, the %d character identifies how much of the total orbital originates directly from the metal d orbitals. The % Bz character shows the overall contribution of the six carbons of the bridged benzene.

	Orbital	Energy (eV)	% Metal Character	% d Character	% Bz character
LUMO+6	194	+0.516	0	0	0
LUMO+5	193	+0.515	0	0	0
LUMO+4	192	+0.264	0	0	0
LUMO+3	191	−0.309	73.2	72.8	2.2
LUMO+2	190	−0.318	71.6	71.2	3.1
LUMO+1	189	−0.466	94.1	85.3	5.9
LUMO	188	−0.762	83.2	49.4	6.5
HOMO	187	−3.414	37.8	36.4	62.1
HOMO-1	186	−3.415	37.6	36.1	62.0
HOMO-2	185	−5.116	8.2	3.1	2.7
HOMO-3	184	−5.116	8.2	3.2	2.6

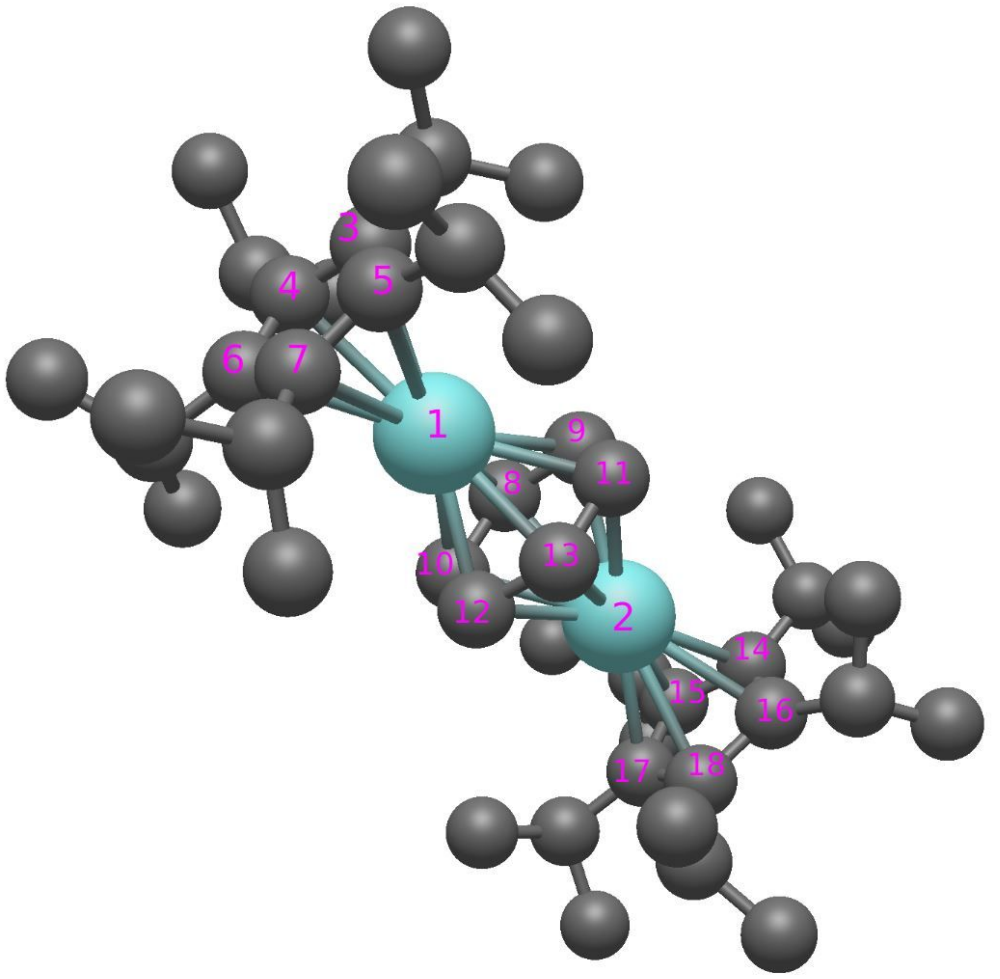

Figure S52. The optimized structure of **1-Y** calculated at the DFT level using TPSSh, def2-TZVP/ECP basis set for Y, and def2-SV(P) basis sets for C and H; H atoms are omitted for clarity. The same labels are used to summarize selected structural parameters of **1-Ln** (Ln = Gd, Tb, Dy, Tm) below.

Table S13. Selected bond distances (Å) and angles (deg) for optimized geometry of singlet **1-Y**(a) calculated using TPSSh, def2-TZVP/ECP basis set for Y, and def2-SV(P) basis sets for C and H.

	$(Cp^{iPr5}Y)_2(Bz)$		
Y(1)···Y(2)	3.963		
Y(1)–Cnt(Cp1)	2.352	Y(2)–Cnt(Cp2)	2.352
Y(1)–C(3)	2.644	Y(2)–C(14)	2.644
Y(1)–C(4)	2.661	Y(2)–C(15)	2.662
Y(1)–C(5)	2.634	Y(2)–C(16)	2.634
Y(1)–C(6)	2.661	Y(2)–C(17)	2.662
Y(1)–C(7)	2.644	Y(2)–C(18)	2.645
Y(1)–Cnt(Bz)	1.982	Y(2)–Cnt(Bz)	1.982
Y(1)–C(8)	2.492	Y(2)–C(8)	2.470
Y(1)–C(9)	2.477	Y(2)–C(9)	2.458
Y(1)–C(10)	2.471	Y(2)–C(10)	2.491
Y(1)–C(11)	2.454	Y(2)–C(11)	2.458
Y(1)–C(12)	2.459	Y(2)–C(12)	2.478
Y(1)–C(13)	2.458	Y(2)–C(13)	2.454
Y(1)–(Cnt)(Bz)–Y(2)	178.5	C(8)–C(9)	1.468
Cnt(Cp1)–Y(1)–Cnt(Bz)	174.8	C(8)–C(10)	1.470
Cnt(Cp2)–Y(2)–Cnt(Bz)	174.6	C(10)–C(12)	1.470
Cnt(Cp1)–Cnt(Bz)–Cnt(Cp2)	174.3	C(12)–C(13)	1.474
C(8)–C(9)–C(11)–C(13)*	−0.8	C(13)–C(11)	1.476
C(8)–C(10)–C(12)–C(13)*	−0.6	C(11)–C(9)	1.474

* dihedral angles

Table S14. Summary of single electronic excitations for singlet **1-Y**(a) computed with TDDFT using TPSSh, def2-TZVP/ECP basis set for Y, and def2-SV(P) basis sets for C and H, including COSMO solvent model. Oscillator strengths are reported in the length gauge. Only the dominant contributions to the overall excitation (%weight > %50) are reported.

Wavelength (nm)	Oscillator Strength	Dominant contributions		
		Occupied	Virtual	%weight
571	0.00008	186	188	98.7
508	0.0004	186	189	92.4
507	0.0004	187	189	91.9
499	0.00006	186	190	49.4
		187	191	49.4
485	0.00006	186	191	57.6
		187	190	40.3
374	0.0001	187	192	99.3
345	0.0002	187	193	28.7
		186	193	24.4
345	1.0	187	191	43.0
		186	190	42.4
344	0.03	187	193	52.9
		187	194	42.4
343	0.01	186	194	61.6
		186	193	35.7
322	0.0008	186	195	75.9
		187	196	23.4
319	0.0004	187	195	53.4
		186	196	45.1
312	0.00001	185	188	89.3
309	0.01	182	188	80.7

Table S15. Selected structural and electronic properties of **1-Gd** calculated using TPSSh, def2-TZVP/ECP basis set for Gd, and def2-SV(P) basis sets for C and H. The ground state is highlighted in peach. Below, Ne^- is the number of unpaired electrons defined for the complex; S is the spin state of the compound; ΔE (eV) shows the energy difference with respect to the lowest energy; C–C(avg) is the average C–C bond distance of benzene; Gd–Bz and Gd–Cp are the metal benzene and metal Cp centroid distances (Å), respectively; Cp1–Bz–Cp2 is the angle (°) formed by the centroids of each Cp and the Bz ring. The Bz spin is the spin state of benzene and $\langle S^2 \rangle$ is the expectation value of the S^2 operator.

Structure	Ne^-	S	ΔE (eV)	C–C(avg) (Å)	Gd–Bz (Å)	Cp1–Bz–Cp2	Gd–Cp(Å)	Bz spin	$\langle S^2 \rangle$
(a)	18	9	0	1.434	2.379	169.3	2.413	1.09	90.07
(b)	0	0	0.26	1.435	2.380	165.0	2.419	0	9.03
(c)	16	8	0.30	1.437	2.353	170.3	2.415	0.05	73.00
(d)	16	8	0.47	1.436	2.377	166.5	2.417	1.10	73.05
(e)	14	7	0.54	1.439	2.350	162.7	2.424	−1.31	58.0
(f)	14	7	0.60	1.436	2.370	165.6	2.419	−0.25	58.01
(g)	0	0	0.82	1.454	2.225	176.3	2.418	0	8.18
(h)[a]	0	0	-[b]	1.468	2.019	175.5	2.395	-0.14	7.09

[a] Optimized at the X2C-SR all-electron level using TPSSh, X2C-TZVPall-2c basis set for Gd, and X2C-SVPall-2c basis sets for C and H. [b]Relative energy is not compared with the energies obtained from ECP calculations as the computed energy systematically differs.

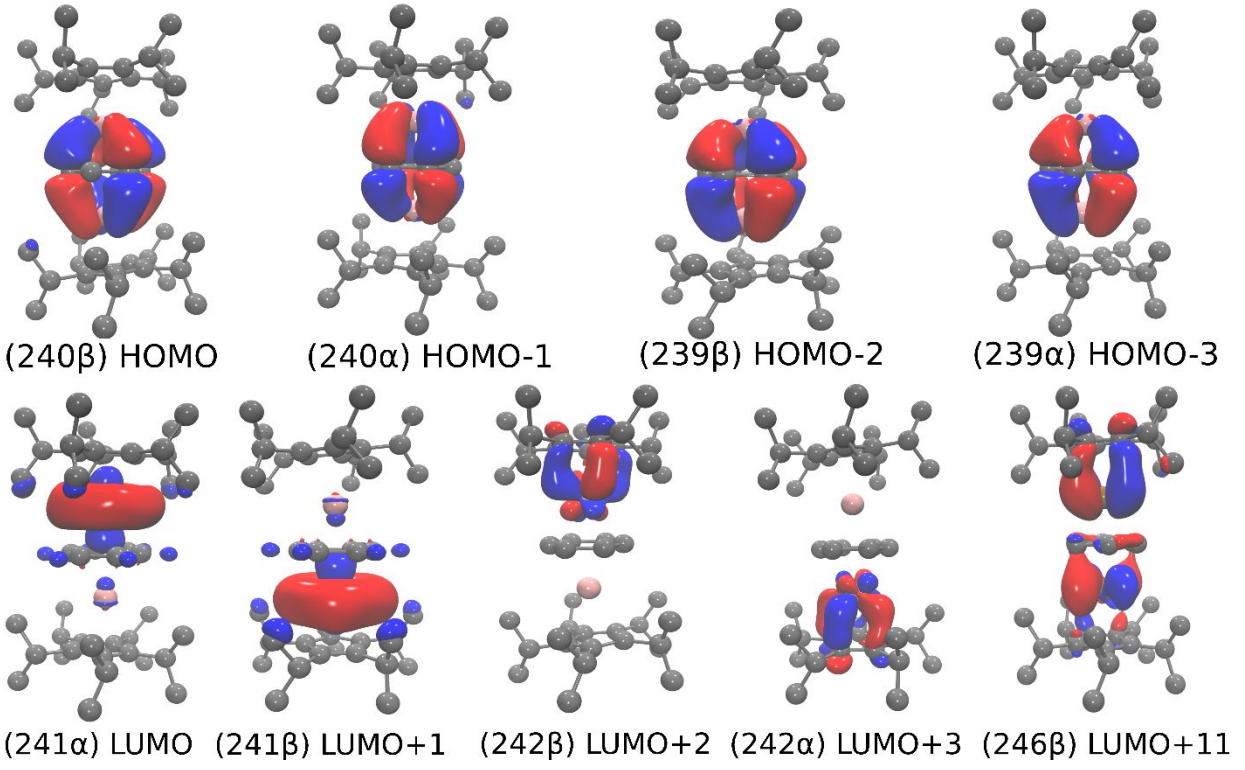

Figure S53. Molecular orbital plots of the singlet **1-Gd**(h). Hydrogen atoms are omitted for clarity, and a contour value of 0.03 was used in the orbital depictions.

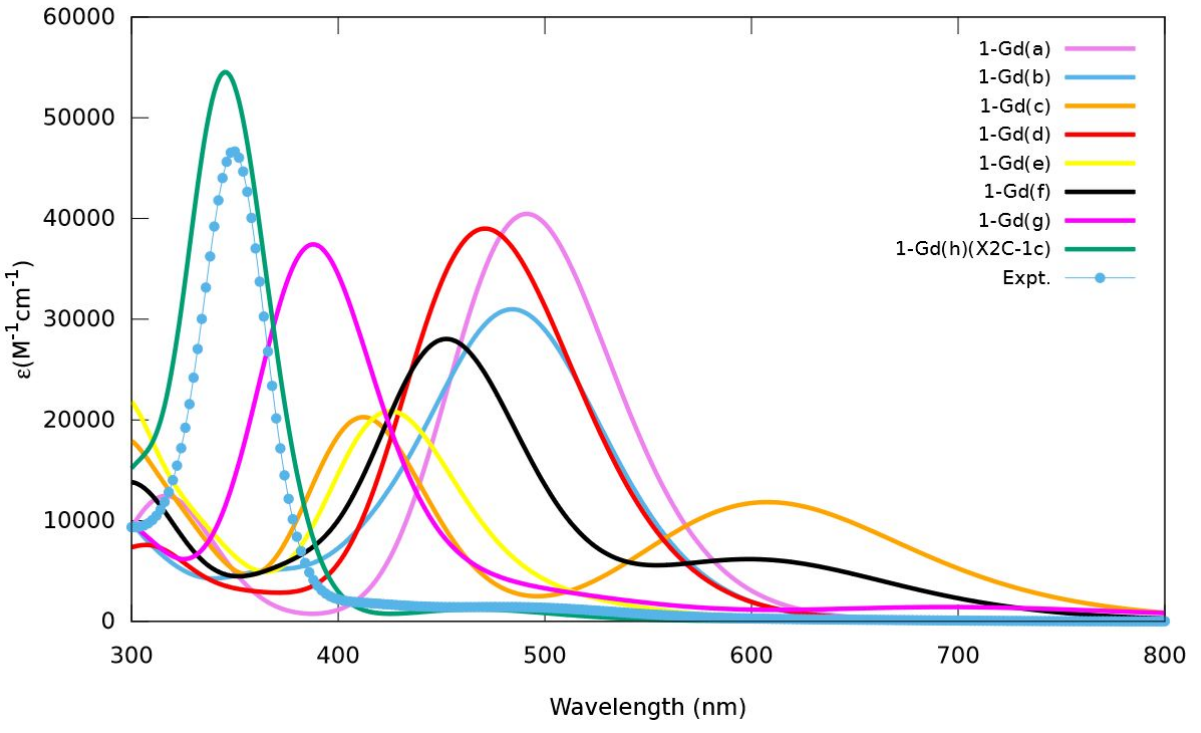

Figure S54. UV-Vis spectral comparison for **1-Gd**. Experimental (connected blue dots) and simulated (solid lines) spectra of all different spin states of **1-Gd** computed with TDDFT using TPSSh and COSMO solvent model. A Gaussian spectral lineshape with a width of 0.2 eV was used.

Table S16. Summary of single electronic excitations for singlet **1-Gd**(h) computed with TDDFT using TPSSh, X2C-TZVPall-2c basis set for Gd, and X2C-SVPall-2c basis sets for C and H, including COSMO solvent model. Oscillator strengths are reported in the length gauge. Only the dominant contributions to the overall excitation (%weight > ~%50) are reported.

Wavelength (nm)	Oscillator Strength	Dominant contributions		
		Occupied	Virtual	%weight
668	0.00007	239α	241α	43.7
		239β	241β	28.8
630	0.0001	239α	241α	31.3
		239β	241β	29.4
		240β	241β	19.4
505	0.00002	239α	242α	12.6
		240α	243α	11.5
478	0.001	239α	247α	23.1
		239β	247β	20.3
471	0.006	239β	243β	15.1
		240β	248β	12.9
461	0.002	240α	249α	20.7
		240β	249β	18.6
346	0.9	240β	246β	10.6
		240α	246α	10.3
		239β	245β	9.1
		239α	245α	8.8
338	0.006	239α	254α	24.8
		240β	254β	23.7
308	0.006	236β	243β	9.4
		236α	243α	6.1
		238β	246β	6.0
		235β	242β	5.3
		238β	243β	5.2
301	0.2	240α	256α	18.0
		240β	257β	16.5
		239β	256β	11.9
		239α	257α	11.1

Table S17. Selected bond distances (Å) and angles (deg) for optimized geometry of singlet **1-Gd**(h) at the X2C-SR all-electron level using TPSSh, X2C-TZVPall-2c basis set for Gd, and X2C-SVPall-2c basis sets for C and H.

	$(Cp^{iPr5}Gd)_2(Bz)$		
Gd(1)···Gd(2)	4.038		
Gd(1)−Cnt(Cp1)	2.394	Gd(2)−Cnt(Cp2)	2.394
Gd(1)−C(3)	2.669	Gd(2)−C(14)	2.673
Gd(1)−C(4)	2.691	Gd(2)−C(15)	2.697
Gd(1)−C(5)	2.706	Gd(2)−C(16)	2.706
Gd(1)−C(6)	2.695	Gd(2)−C(17)	2.689
Gd(1)−C(7)	2.671	Gd(2)−C(18)	2.668
Gd(1)−Cnt(Bz)	2.019	Gd(2)−Cnt(Bz)	2.019
Gd(1)−C(8)	2.488	Gd(2)−C(8)	2.514
Gd(1)−C(9)	2.487	Gd(2)−C(9)	2.495
Gd(1)−C(10)	2.498	Gd(2)−C(10)	2.487
Gd(1)−C(11)	2.515	Gd(2)−C(11)	2.487
Gd(1)−C(12)	2.503	Gd(2)−C(12)	2.486
Gd(1)−C(13)	2.485	Gd(2)−C(13)	2.507
Gd(1)−(Cnt)(Bz)−Gd(2)	178.8	C(8)−C(9)	1.466
Cnt(Cp1)−Gd(1)−Cnt(Bz)	174.1	C(8)−C(10)	1.470
Cnt(Cp2)−Gd(2)−Cnt(Bz)	174.2	C(10)−C(12)	1.472
Cnt(Cp1)−Cnt(Bz)−Cnt(Cp2)	175.5	C(12)−C(13)	1.470
C(8)−C(9)−C(11)−C(13)*	−0.8	C(13)−C(11)	1.466
C(8)−C(10)−C(12)−C(13)*	−0.6	C(11)−C(9)	1.464

* dihedral angles

Table S18. Molecular orbital energies and Mulliken population analysis of singlet **1-Gd**(h) complex. The % metal character identifies the overall metal contribution from both Gd centers combined to the molecular orbital, the %d character identifies how much of the total orbital originates directly from the metal d orbitals. The % Bz character shows the overall contribution of the six carbons of the bridged benzene.

	Orbital	Energy (eV)	% Metal Character	% d Character	% Bz character
LUMO+11	246β	−0.261	79.8	66.0	3.2
LUMO+9	245β	−0.268	76.2	66.6	4.3
LUMO+3	242α	−0.353	88	7	0
LUMO+2	242β	−0.356	89	7	0
LUMO+1	241β	−0.896	100	66.9	0
LUMO	241α	−0.897	100	70	0
HOMO	240β	−3.457	39.2	35.1	60.8
HOMO-1	240α	−3.457	39.3	35.2	60.7
HOMO-2	239β	−3.467	39.6	35.7	60.4
HOMO-3	239α	−3.467	39.6	35.7	60.4

Table S19. Selected structural and electronic properties of **1-Tb** calculated using TPSSh, def2-TZVP/ECP basis set for Tb, and def2-SV(P) basis sets for C and H. The ground state is highlighted in peach. Below, Ne^- is the number of unpaired electrons defined for the complex; S is the spin state of the compound ; ΔE (eV) shows the energy difference with respect to the lowest energy; C–C(avg) is the average C–C bond distance of benzene; Tb–Bz and Tb–Cp are the metal benzene and metal Cp centroid distances (Å), respectively; Cp1–Bz–Cp2 is the angle (°) formed by the centroids of each Cp and the Bz ring. The Bz spin is the spin state of benzene and $\langle S^2 \rangle$ is the expectation value of the S^2 operator.

Structure	Ne^-	S	ΔE (eV)	C–C(avg) (Å)	Tb–Bz(Å)	Cp1–Bz–Cp2	Tb–Cp(Å)	Bz spin	$\langle S^2 \rangle$
(a)	16	8	0	1.454	2.062	174.8	2.371	-0.22	72.11
(b)	14	7	0.03	1.461	2.038	172.5	2.376	-0.26	56.85
(c)	0	0	0.10	1.465	2.019	171.0	2.379	0	7.60
(d)[a]	0	0	-[b]	1.469	1.993	170.9	2.381	-0.14	6.05
(e)	12	6	1.07	1.449	2.184	175.8	2.394	−0.78	43.87
(f)	10	5	1.27	1.454	2.153	177.3	2.395	−0.84	32.86
(g)	10	5	4.49	1.441	2.339	172.0	2.404	−1.20	33.00

[a] Optimized at the X2C-SR all-electron level using TPSSh, X2C-TZVPall-2c basis set for Tb, and X2C-SVPall-2c basis sets for C and H. [b]Relative energy is not compared with the energies obtained from ECP calculations as the computed energy systematically differs.

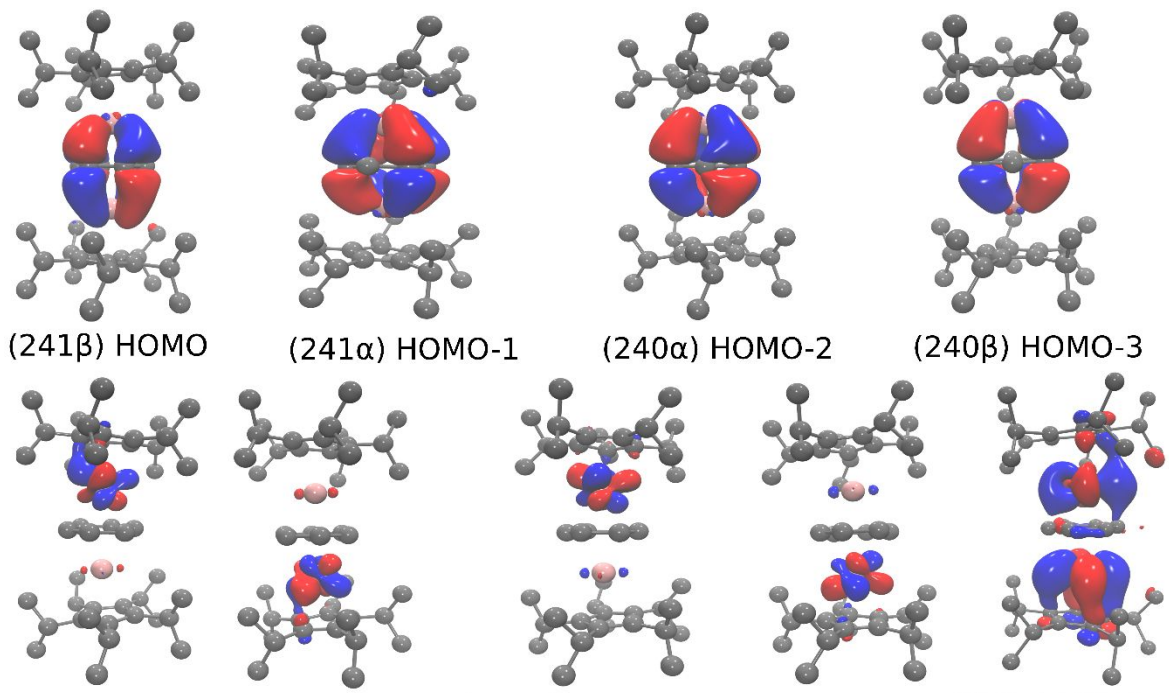

Figure S55. Molecular orbital plots of the singlet **1-Tb**(d). Hydrogen atoms are omitted for clarity, and a contour value of 0.03 was used in the orbital depictions.

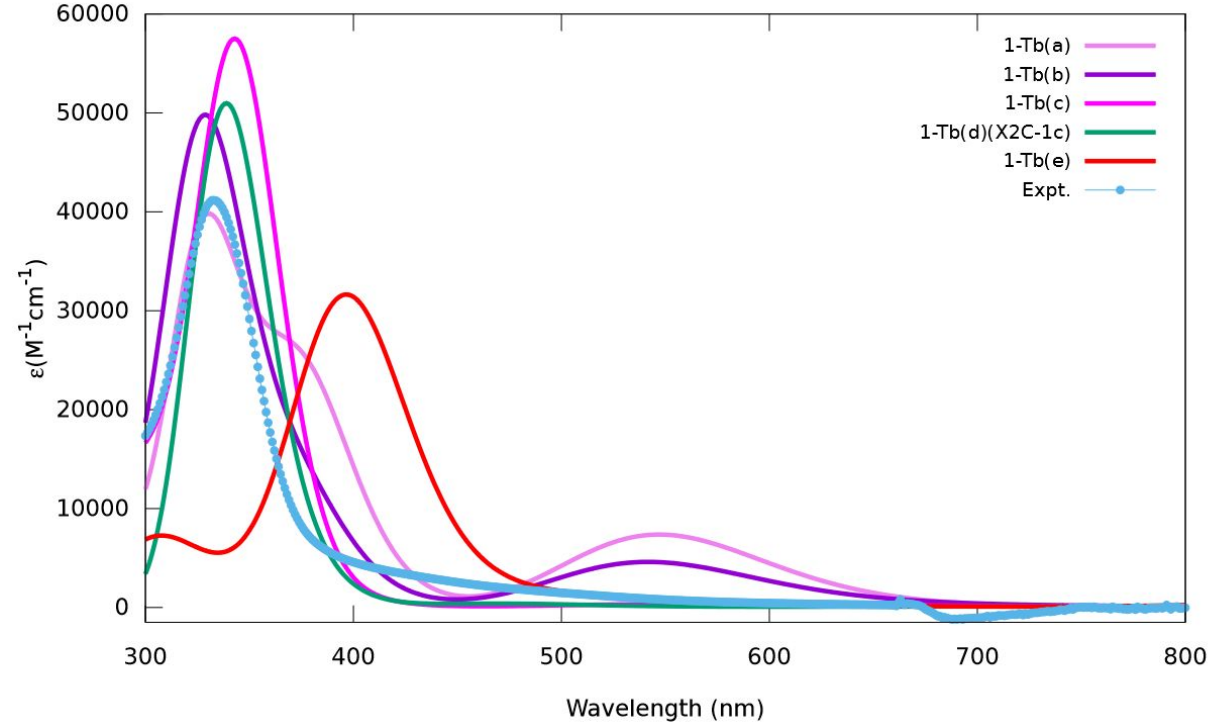

Figure S56. UV-Vis spectral comparison for **1-Tb**. Experimental (connected blue dots) and simulated (solid lines) spectra of all different spin states of **1-Tb** computed with TDDFT using TPSSh and COSMO solvent model. A Gaussian spectral lineshape with a width of 0.2 eV was used.

Table S20. Summary of single electronic excitations for singlet **1-Tb**(d) computed with TDDFT using TPSSh, X2C-TZVPall-2c basis set for Tb, and X2C-SVPall-2c basis sets for C and H, including COSMO solvent model. Oscillator strengths are reported in the length gauge. Only the dominant contributions to the overall excitation (%weight > %50) are reported.

Wavelength (nm)	Oscillator Strength	Dominant contributions		
		Occupied	Virtual	% weight
727	0.0006	240α	244α	51.6
		240β	244β	40.5
614	0.0002	241β	245β	35.8
		241α	245α	32.9
506	0.0006	241α	246α	70.1
		241β	246β	22.4
477	0.0009	240β	248β	34.3
		240β	249β	16.2
452	0.0009	241α	249α	36.9
		241β	248β	23.2
371	0.02	235β	242β	40.2
		237β	242β	35.9
339	0.7	241α	251α	12.7
		241β	251β	11.7
		240α	248α	11.5
		240β	250β	5.6
331	0.002	240β	253β	45.2
		241α	254α	43.6

Table S21. Selected bond distances (Å) and angles (deg) for optimized geometry of singlet **1-Tb**(d) at the X2C-SR all-electron level using TPSSh, X2C-TZVPall-2c basis set for Tb, and X2C-SVPall-2c basis sets for C and H.

	$(Cp^{iPr5}\ Tb)_2(Bz)$		
Tb(1)···Tb(2)	3.986		
Tb(1)−Cnt(Cp1)	2.381	Tb(2)−Cnt(Cp2)	2.381
Tb(1)−C(3)	2.679	Tb(2)−C(14)	2.672
Tb(1)−C(4)	2.694	Tb(2)−C(15)	2.656
Tb(1)−C(5)	2.682	Tb(2)−C(16)	2.665
Tb(1)−C(6)	2.660	Tb(2)−C(17)	2.688
Tb(1)−C(7)	2.657	Tb(2)−C(18)	2.693
Tb(1)−Cnt(Bz)	1.993	Tb(2)−Cnt(Bz)	1.993
Tb(1)−C(8)	2.477	Tb(2)−C(8)	2.500
Tb(1)−C(9)	2.507	Tb(2)−C(9)	2.483
Tb(1)−C(10)	2.471	Tb(2)−C(10)	2.494
Tb(1)−C(11)	2.477	Tb(2)−C(11)	2.450
Tb(1)−C(12)	2.442	Tb(2)−C(12)	2.469
Tb(1)−C(13)	2.481	Tb(2)−C(13)	2.456
Tb(1)−(Cnt)(Bz)−Tb(2)	177.9	C(8)−C(9)	1.464
Cnt(Cp1)−Tb(1)−Cnt(Bz)	173.7	C(8)−C(10)	1.464
Cnt(Cp2)−Tb(2)−Cnt(Bz)	173.4	C(10)−C(12)	1.467
Cnt(Cp1)−Cnt(Bz)−Cnt(Cp2)	170.9	C(12)−C(13)	1.473
C(8) −C(9) −C(11) −C(13)*	4.2	C(13)−C(11)	1.474
C(8) −C(10) −C(12) −C(13)*	-4.1	C(11)−C(9)	1.469

* dihedral angles

Table S22. Molecular orbital energies and Mulliken population analysis of singlet **1-Tb**(d) complex. The % metal character identifies the overall metal contribution from both Tb centers combined to the molecular orbital, the %d character identifies how much of the total orbital originates directly from the metal d orbitals. The % Bz character shows the overall contribution of the six carbons of the bridged benzene.

	Orbital	Energy (eV)	% Metal Character	% d Character	% Bz character
LUMO+19	251α	−0.125	80.0	54.9	1.4
LUMO+17	250β	−0.163	90.0	40.9	0
LUMO+13	248α	−0.211	82.8	64.0	2.7
LUMO+3	243β	−1.120	100	5.6	0
LUMO+2	243α	−1.127	98.9	5.6	0
LUMO+1	242α	−1.133	97.6	5.4	0
LUMO	242β	−1.139	97.6	5.4	0
HOMO	241β	−3.486	38.7	32.0	61.3
HOMO-1	241α	−3.489	39.3	32.3	60.7
HOMO-2	240α	−3.499	39.0	32.7	61.0
HOMO-3	240β	−3.503	39.6	33.1	60.4

Table S23. Selected structural and electronic properties of **1-Dy** calculated using TPSSh, def2-TZVP/ECP basis set for Dy, and def2-SV(P) basis sets for C and H. The ground state is highlighted in peach. The ground state is highlighted in peach. Below, Ne^- is the number of unpaired electrons defined for the complex; S is the spin state of the compound; ΔE (eV) shows the energy difference with respect to the lowest energy; C–C(avg) is the average C–C bond distance of benzene; Dy–Bz and Dy–Cp are the metal benzene and metal Cp centroid distances (Å), respectively; Cp1–Bz–Cp2 is the angle (°) formed by the centroids of each Cp and the Bz ring. The Bz spin is the spin state of benzene and $\langle S^2 \rangle$ is the expectation value of the S^2 operator.

Structure	Ne^-	S	ΔE (eV)	C–C(avg) (Å)	Dy–Bz (Å)	Cp1–Bz–Cp2	Dy–Cp (Å)	Bz spin	$\langle S^2 \rangle$
(a)	12	6	0	1.453	2.140	196.9	2.386	0.45	42.78
(b)	12	6	0.03	1.441	2.272	178.3	2.393	-0.16	43.02
(c)	0	0	0.07	1.469	2.017	164.8	2.374	0	6.32
(d)[a]	0	0	-[b]	1.467	1.982	172.8	2.368	-0.09	5.00
(e)	10	5	0.15	1.442	2.258	174.7	2.396	−0.40	32.00
(f)	8	4	0.27	1.440	2.318	173.1	2.388	−1.40	23.00
(g)	0	0	0.30	1.451	2.184	171.0	2.384	−0.67	6.73
(h)	14	7	1.28	1.436	2.269	167.9	2.382	1.00	56.60

[a] Optimized at the X2C-SR all-electron level using TPSSh, X2C-TZVPall-2c basis set for Dy, and X2C-SVPall-2c basis sets for C and H. [b]Relative energy is not compared with the energies obtained from ECP calculations as the computed energy systematically differs.

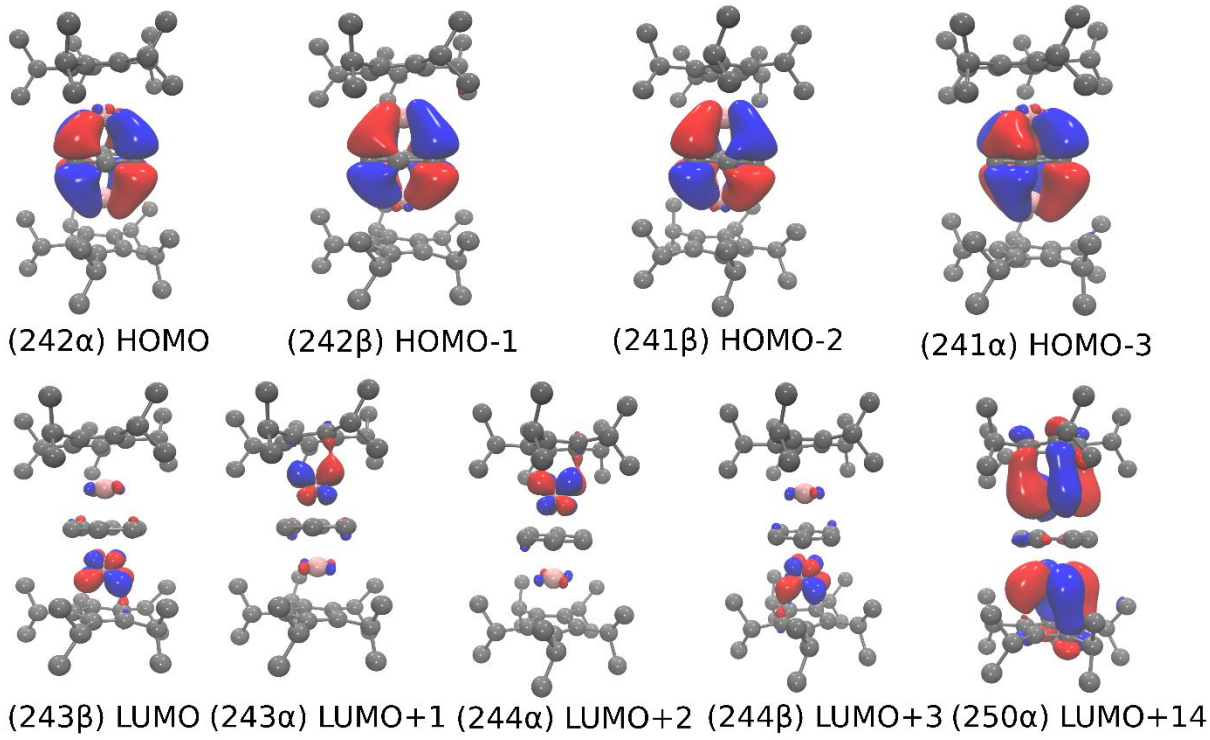

Figure S57. Molecular orbital plots of the singlet **1-Dy**(d). Hydrogen atoms are omitted for clarity, and a contour value of 0.03 was used in the orbital depictions.

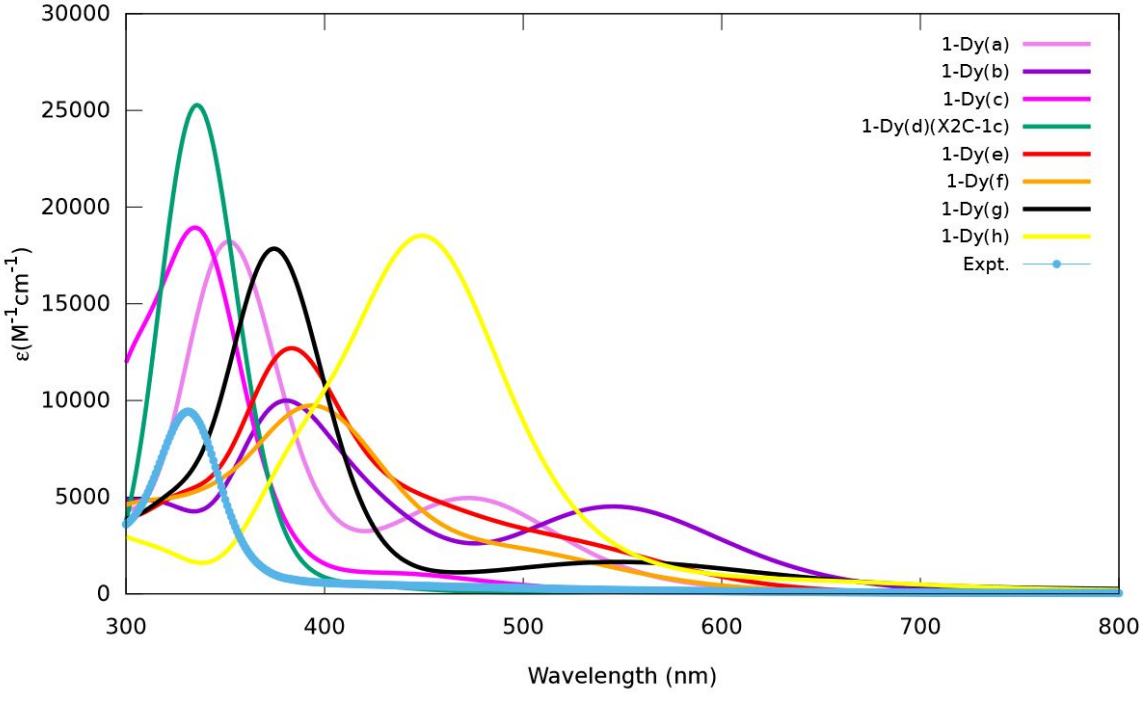

Figure S58. UV-Vis spectral comparison for **1-Dy**. Experimental (connected blue dots) and simulated (solid lines) spectra of all different spin states of **1-Dy** computed with TDDFT using TPSSh and COSMO solvent model. A Gaussian spectral lineshape with a width of 0.2 eV was used.

Table S24. Molecular orbital energies and Mulliken population analysis of singlet **1-Dy**(d) complex. The % metal character identifies the overall metal contribution from both Dy centers combined to the molecular orbital, the %d character identifies how much of the total orbital originates directly from the metal d orbitals. The % Bz character shows the overall contribution of the six carbons of the bridged benzene.

	Orbital	Energy (eV)	% Metal Character	% d Character	% Bz character
LUMO+15	250β	−0.035	69.8	67.0	0
LUMO+14	250α	−0.035	70.8	68.0	0
LUMO+13	249α	−0.076	70.1	69.0	0
LUMO+12	249β	−0.076	70.2	70.3	0
LUMO+3	244β	−1.497	98.8	7.0	0
LUMO+2	244α	−1.498	98.7	7.0	0
LUMO+1	243α	−1.510	98.8	7.2	0
LUMO	243β	−1.512	98.7	7.2	0
HOMO	242α	−3.459	40.2	29.3	59.8
HOMO-1	242β	−3.459	39.6	28.8	58.5
HOMO-2	241β	−3.466	39.4	29.2	60.6
HOMO-3	241α	−3.466	39.5	29.1	60.5

Table S25. Selected bond distances (Å) and angles (deg) for optimized geometry of singlet **1-Dy**(d) at the X2C-SR all-electron level using TPSSh, X2C-TZVPall-2c basis set for Dy, and X2C-SVPall-2c basis sets for C and H.

	$(Cp^{iPr5}Dy)_2(Bz)$		
Dy(1)···Dy(2)	3.963		
Dy(1)−Cnt(Cp1)	2.368	Dy(2)−Cnt(Cp2)	2.368
Dy(1)−C(3)	2.646	Dy(2)−C(14)	2.679
Dy(1)−C(4)	2.656	Dy(2)−C(15)	2.673
Dy(1)−C(5)	2.676	Dy(2)−C(16)	2.654
Dy(1)−C(6)	2.678	Dy(2)−C(17)	2.648
Dy(1)−C(7)	2.660	Dy(2)−C(18)	2.663
Dy(1)−Cnt(Bz)	1.982	Dy(2)−Cnt(Bz)	1.982
Dy(1)−C(8)	2.479	Dy(2)−C(8)	2.483
Dy(1)−C(9)	2.464	Dy(2)−C(9)	2.473
Dy(1)−C(10)	2.463	Dy(2)−C(10)	2.474
Dy(1)−C(11)	2.455	Dy(2)−C(11)	2.451
Dy(1)−C(12)	2.465	Dy(2)−C(12)	2.461
Dy(1)−C(13)	2.448	Dy(2)−C(13)	2.452
Dy(1)−(Cnt)(Bz)−Dy(2)	178.2	C(8)−C(9)	1.464
Cnt(Cp1)−Dy(1)−Cnt(Bz)	174.4	C(8)−C(10)	1.463
Cnt(Cp2)−Dy(2)−Cnt(Bz)	174.6	C(10)−C(12)	1.466
Cnt(Cp1)−Cnt(Bz)−Cnt(Cp2)	172.8	C(12)−C(13)	1.470
C(8)−C(9)−C(11)−C(13)*	−0.8	C(13)−C(11)	1.472
C(8)−C(10)−C(12)−C(13)*	−0.3	C(11)−C(9)	1.468

* dihedral angles

Table S26. Summary of single electronic excitations for singlet **1-Dy**(d) computed with TDDFT using TPSSh, X2C-TZVPall-2c basis set for Dy, and X2C-SVPall-2c basis sets for C and H, including COSMO solvent model. Oscillator strengths are reported in the length gauge. Only the dominant contributions to the overall excitation (%weight > %50) are reported.

Wavelength (nm)	Oscillator Strength	Dominant contributions		
		Occupied	Virtual	% weight
670	0.005	241β	244β	23.1
		241α	244α	22.7
		242β	243β	22.1
555	0.001	242α	246α	27.5
		241α	247α	17.7
		241β	246β	15.0
439	0.0008	241α	249α	22.5
		241β	249β	22.5
		242α	250α	18.3
409	0.007	236α	244α	19.1
		236β	244β	12.0
		238α	244α	10.4
		239α	243α	8.6
372	0.001	237α	244α	26.5
		237β	244β	17.3
		239α	244α	15.7
338	0.7	242α	250α	17.5
		242β	250β	17.5
		241β	249β	16.5
		241α	249α	16.5

Table S27. Selected structural and electronic properties of **1-Tm** at the X2C-SR all-electron level using TPSSh, X2C-TZVPall-2c basis set for Tm, and X2C-SVPall-2c basis sets for C and H. The ground state is highlighted in peach. Below, Ne^- is the number of unpaired electrons defined for the complex; S is the spin state of the compound; ΔE (eV) shows the energy difference with respect to the lowest energy; C–C(avg) is the average C–C bond distance of benzene; Tm–Bz and Tm–Cp are the metal benzene and metal Cp centroid distances (Å), respectively; Cp1–Bz–Cp2 is the angle (°) formed by the centroids of each Cp and the Bz ring. The Bz spin is the spin state of benzene and $\langle S^2 \rangle$ is the expectation value of the S^2 operator.

Structure	Ne^-	S	ΔE (eV)	C–C(avg) (Å)	Tm–Bz (Å)	Cp1–Bz–Cp2	Tm–Cp (Å)	Bz spin	$\langle S^2 \rangle$
(a)	4	2	0	1.464	1.998	168.8	2.326	0.37	6.01
(b)	2	1	0.37	1.457	2.066	170.1	2.327	-0.46	3.02
(c)	0	0	0.74	1.450	2.123	169.9	2.324	-1.1	2.02
(d)	0	0	0.003	1.465	1.994	168.9	2.324	0.03	1.99

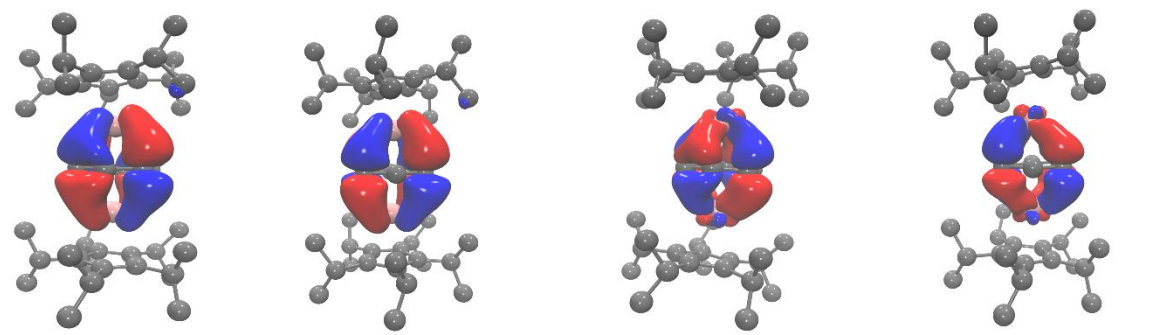

Figure S59. Molecular orbital plots of the quintet **1-Tm**(a). Hydrogen atoms are omitted for clarity, and a contour value of 0.03 was used in the orbital depictions.

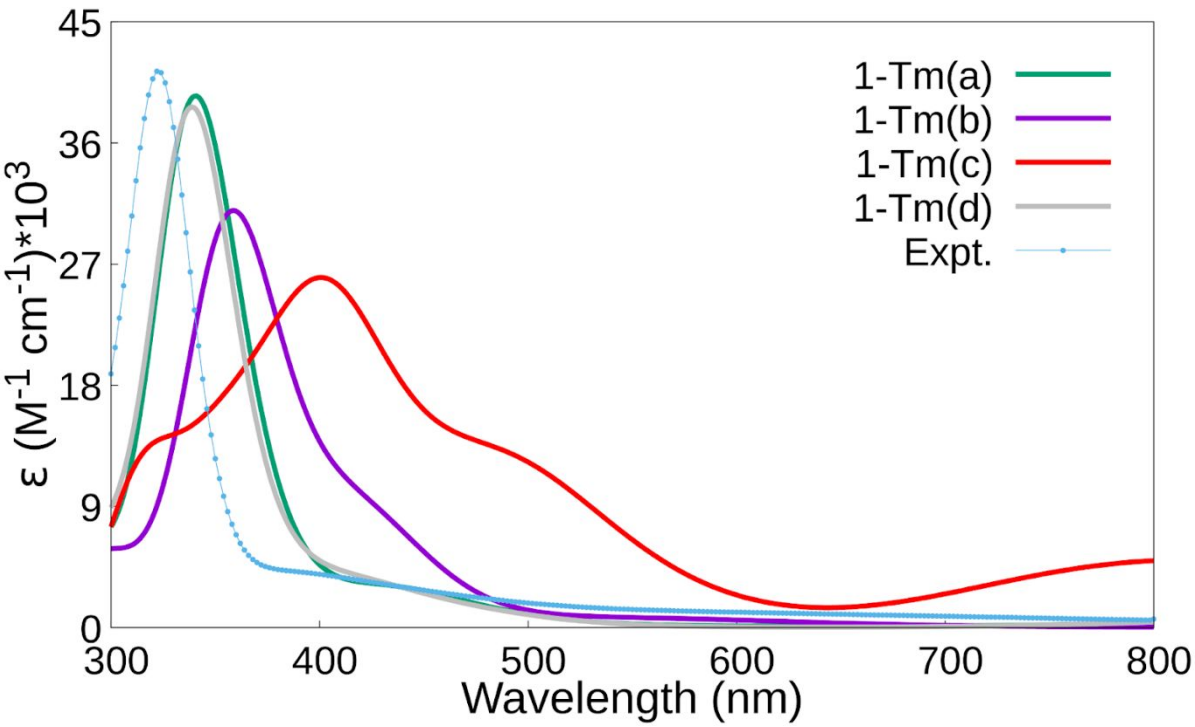

Figure S60. UV-Vis spectral comparison for **1-Tm**. Experimental (connected blue dots) and simulated (solid lines) spectra of all different spin states of **1-Tm** computed with TDDFT using TPSSh and COSMO solvent model. A Gaussian spectral lineshape with a width of 0.2 eV was used.

Table S28. Molecular orbital energies and Mulliken population analysis of quintet **1-Tm**(a) complex. The % metal character identifies the overall metal contribution from both Tm centers combined to the molecular orbital, the %d character identifies how much of the total orbital originates directly from the metal d orbitals. The % Bz character shows the overall contribution of the six carbons of the bridged benzene.

	Orbital	Energy (eV)	% Metal Character	% d Character	% Bz character
LUMO+13	252β	+0.288	61.6	60.3	0
LUMO+12	251β	+0.254	91.8	68.0	0
LUMO+10	250β	+0.209	64.5	60.9	35.5
LUMO+9	251α	+0.105	65.1	64.1	0
LUMO+8	250α	+0.029	67.8	66.4	0
LUMO+6	249α	−0.216	95.2	90.3	0
LUMO+5	248β	−0.473	100	42.8	0
LUMO+3	247β	−1.133	100	00.0	0
LUMO+2	246β	−1.158	100	00.3	0
LUMO+1	245β	−1.986	73.9	16.3	25.0
LUMO	244β	−2.051	76.9	15.0	23.1
HOMO	247α	−3.321	31.7	29.3	68.3
HOMO-1	246α	−3.348	32.3	29.9	67.7
HOMO-2	243β	−3.402	57.8	15.4	42.2
HOMO-3	242β	−3.429	59.2	14.3	40.8
HOMO-5	240β	−4.597	81.4	0.9	18.6
HOMO-6	239β	−4.730	79.4	1.1	20.6
HOMO-7	238β	−4.769	79.5	1.4	20.5
HOMO-12	237β	−5.113	40.3	4.1	58.6
HOMO-13	236β	−5.150	43.6	3.8	55.3
HOMO-14	235β	−5.180	40.0	4.0	60.0
HOMO-15	234β	−5.190	35.9	4.8	64.1
HOMO-16	233β	−5.400	97.6	0.1	2.4
HOMO-21	228β	−5.960	100	0.4	0

Table S29. Selected bond distances (Å) and angles (deg) for optimized geometry of quintet **1-Tm**(a) at the X2C-SR all-electron level using TPSSh, X2C-TZVPall-2c basis set for Tm, and X2C-SVPall-2c basis sets for C and H.

	$(Cp^{iPr5}Tm)_2(Bz)$		
Tm(1)···Tm(2)	3.995		
Tm(1)−Cnt(Cp1)	2.326	Tm(2)−Cnt(Cp2)	2.328
Tm(1)−C(3)	2.638	Tm(2)−C(14)	2.612
Tm(1)−C(4)	2.652	Tm(2)−C(15)	2.645
Tm(1)−C(5)	2.630	Tm(2)−C(16)	2.654
Tm(1)−C(6)	2.601	Tm(2)−C(17)	2.624
Tm(1)−C(7)	2.608	Tm(2)−C(18)	2.602
Tm(1)−Cnt(Bz)	1.998	Tm(2)−Cnt(Bz)	1.997
Tm(1)−C(8)	2.412	Tm(2)−C(8)	2.508
Tm(1)−C(9)	2.482	Tm(2)−C(9)	2.433
Tm(1)−C(10)	2.498	Tm(2)−C(10)	2.444
Tm(1)−C(11)	2.447	Tm(2)−C(11)	2.533
Tm(1)−C(12)	2.522	Tm(2)−C(12)	2.469
Tm(1)−C(13)	2.496	Tm(2)−C(13)	2.463
Tm(1)−(Cnt)(Bz)−Tm(2)	177.9	C(8)−C(9)	1.460
Cnt(Cp1)−Tm(1)−Cnt(Bz)	171.0	C(8)−C(10)	1.466
Cnt(Cp2)−Tm(2)−Cnt(Bz)	171.0	C(10)−C(12)	1.468
Cnt(Cp1)−Cnt(Bz)−Cnt(Cp2)	168.8	C(12)−C(13)	1.465
C(8)−C(9)−C(11)−C(13)*	7.0	C(13)−C(11)	1.463
C(8)−C(10)−C(12)−C(13)*	8.1	C(11)−C(9)	1.460

* dihedral angles

Table S30. Summary of single electronic excitations for **1-Tm**(a) computed with TDDFT using TPSSh, X2C-TZVPall-2c basis set for Tm, and X2C-SVPall-2c basis sets for C and H, including COSMO solvent model. Oscillator strengths are reported in the length gauge. Only the dominant contributions to the overall excitation (%weight > %50) are reported.

Wavelength (nm)	Oscillator Strength	Dominant contributions		
		Occupied	Virtual	% weight
751	0.0002	228β	244β	28.1
		228β	246β	23.7
657	0.0003	242β	247β	58.0
581	0.0005	240β	245β	61.4
493	0.001	247α	249α	85.9
474	0.003	237β	245β	32.6
		237β	244β	31.6
446	0.004	247α	250α	67.7
431	0.03	247α	251α	42.7
		243β	250β	23.4
405	0.01	242β	252β	41.9
		243β	250β	39.9
376	0.0002	243β	251β	85.0
367	0.07	235β	246β	39.1
		236β	246β	13.5
		238β	246β	13.2
363	0.02	234β	247β	38.8
		239β	247β	9.5
		237β	247β	8.8
342	0.05	246α	254α	86.5
340	0.2	243β	253β	53.2
		246α	254α	7.8
339	0.3	243β	253β	41.9
		242β	252β	9.6
		247α	251α	8.4
336	0.04	242β	253β	91.5
308	0.006	237β	248β	31.0
		233β	248β	28.6

Table S31. Atomic populations analysis from NPA (total density) for indicated **1-Ln** ground states calculated using TPSSh and the corresponding basis sets.

State	atom	charge	n(s)	n(p)	n(d)	n(f)
1-Y(a)	Y(1)	1.798	2.068	6.007	1.121	0
1-Y(a)	Y(2)	1.797	2.068	6.007	1.122	0
1-Gd(h)	Gd(1)	1.738	10.063	24.002	21.113	7.084
1-Gd(h)	Gd(2)	1.737	10.063	24.002	21.113	7.084
1-Tb(d)	Tb(1)	1.699	10.064	24.002	21.101	8.132
1-Tb(d)	Tb(2)	1.699	10.064	24.002	21.102	8.132
1-Dy(d)	Dy(1)	1.719	10.063	24.005	21.004	9.209
1-Dy(d)	Dy(2)	1.719	10.063	24.005	21.003	9.209
1-Tm(a)	Tm(1)	1.679	10.065	24.005	20.845	12.404
1-Tm(a)	Tm(2)	1.678	10.065	24.005	20.842	12.408
1-Tm(d)	Tm(1)	1.652	10.069	24.005	20.887	12.386
1-Tm(d)	Tm(2)	1.672	10.068	24.004	20.868	12.386

Table S32. Atomic populations analysis from NPA (spin density) for **1-Ln** (Ln = Gd, Tb, Dy, Tm) ground states calculated using TPSSh and the corresponding basis sets.

State	atom	sum	n(s)	n(p)	n(d)	n(f)
1-Gd(h)	Gd(1)	7.319	0.023	0.084	0.0329	6.883
1-Gd(h)	Gd(2)	−7.146	−0.006	−0.036	−0.237	−6.867
1-Tb(d)	Tb(1)	6.169	0.018	0.069	0.240	5.842
1-Tb(d)	Tb(2)	−6.005	−0.005	−0.028	−0.148	−5.825
1-Dy(d)	Dy(1)	−4.877	−0.004	−0.025	−0.104	−4.743
1-Dy(d)	Dy(2)	4.991	0.014	0.050	0.156	4.771
1-Tm(a)	Tm(1)	1.812	0.004	0.014	0.213	1.580
1-Tm(a)	Tm(2)	1.807	0.005	0.015	0.212	1.576
1-Tm(d)	Tm(1)	−1.673	0.00	−0.005	−0.089	−1.580
1-Tm(d)	Tm(2)	1.656	0.004	0.018	0.039	1.594

Table S33. Comparison of λ_{max} excitation energies obtained from experiment with parenthesized uncertainties and from computations for **1-Ln** along with the absolute errors.

Compound	ε_{expt} ($M^{-1}\cdot cm^{-1}$)	E_{expt} (eV)	E_{TDDFT} (eV)	$\lvert E_{expt}$ (eV) − E_{TDDFT} (eV)$\rvert$
1-Y	64500(600)	3.65	3.59	0.05
1-Gd	52700(600)	3.54	3.58	0.04
1-Tb	40400(400)	3.73	3.66	0.08
1-Dy	11000(1300)	3.75	3.67	0.08
1-Tm	35000(1800)	3.88	3.66	0.22

10. References

(1) McClain, K. R.; Gould, C. A.; Chakarawet, K.; Teat, S. J.; Groshens, T. J.; Long, J. R.; Harvey, B. G. High-Temperature Magnetic Blocking and Magneto-Structural Correlations in a Series of Dysprosium(III) Metallocenium Single-Molecule Magnets. *Chem. Sci.* **2018**, *9* (45), 8492–8503.

(2) Gould, C. A.; McClain, K. R.; Reta, D.; Kragskow, J. G. C.; Marchiori, D. A.; Lachman, E.; Choi, E.-S.; Analytis, J. G.; Britt, R. D.; Chilton, N. F.; Harvey, B. G.; Long, J. R. Ultrahard Magnetism from Mixed-Valence Dilanthanide Complexes with Metal-Metal Bonding. *Science* **2022**, *375* (6577), 198–202.

(3) Bruker. APEX III, 2012.

(4) Bruker. SAINT, 2012.

(5) Bruker. SMART, 2012.

(6) Sheldrick, G. M. SHELXT – Integrated Space-Group and Crystal-Structure Determination. *Acta Crystallogr. Sect. Found. Adv.* **2015**, *71* (1), 3–8.

(7) Müller, P.; Herbst-Irmer, R.; Spek, A. L.; Schneider, T. R.; Sawaya, M. R. *Crystal Structure Refinement: A Crystallographer's Guide to SHELXL*; Oxford University Press, 2006.

(8) Dolomanov, O. V.; Bourhis, L. J.; Gildea, R. J.; Howard, J. a. K.; Puschmann, H. OLEX2: A Complete Structure Solution, Refinement and Analysis Program. *J. Appl. Crystallogr.* **2009**, *42* (2), 339–341.

(9) Lu, T. Simple, Reliable, and Universal Metrics of Molecular Planarity. *J. Mol. Model.* **2021**, *27* (9), 263.

(10) Macrae, C. F.; Sovago, I.; Cottrell, S. J.; Galek, P. T. A.; McCabe, P.; Pidcock, E.; Platings, M.; Shields, G. P.; Stevens, J. S.; Towler, M.; Wood, P. A. Mercury 4.0: From Visualization to Analysis, Design and Prediction. *J. Appl. Crystallogr.* **2020**, *53* (1), 226–235.

(11) Kotyk, C. M.; MacDonald, M. R.; Ziller, J. W.; Evans, W. J. Reactivity of the Ln2+ Complexes [K(2.2.2-Cryptand)][$(C_5H_4SiMe_3)_3$Ln]: Reduction of Naphthalene and Biphenyl. *Organometallics* **2015**, *34* (11), 2287–2295.

(12) Gould, C. A.; Marbey, J.; Vieru, V.; Marchiori, D. A.; David Britt, R.; Chibotaru, L. F.; Hill, S.; Long, J. R. Isolation of a Triplet Benzene Dianion. *Nat. Chem.* **2021**, *13* (10), 1001–1005.

(13) Palumbo, C. T.; Halter, D. P.; Voora, V. K.; Chen, G. P.; Ziller, J. W.; Gembicky, M.; Rheingold, A. L.; Furche, F.; Meyer, K.; Evans, W. J. Using Diamagnetic Yttrium and Lanthanum Complexes to Explore Ligand Reduction and C–H Bond Activation in a Tris(Aryloxide)Mesitylene Ligand System. *Inorg. Chem.* **2018**, *57* (20), 12876–12884.

(14) Xin, T.; Wang, X.; Yang, K.; Liang, J.; Huang, W. Rare Earth Metal Complexes Supported by a Tripodal Tris(Amido) Ligand System Featuring an Arene Anchor. *Inorg. Chem.* **2021**, *60* (20), 15321–15329.

(15) Zhang, G.; Wang, S.; Zhou, S.; Wei, Y.; Guo, L.; Zhu, X.; Zhang, L.; Gu, X.; Mu, X. Synthesis and Reactivity of Rare-Earth-Metal Monoalkyl Complexes Supported by Bidentate Indolyl Ligands and Their High Performance in Isoprene 1,4-Cis Polymerization. *Organometallics* **2015**, *34* (17), 4251–4261.

(16) Deacon, G. B.; Feng, T.; Forsyth, C. M.; Gitlits, A.; Hockless, D. C. R.; Shen, Q.; Skelton, B. W.; White, A. H. A Simple Synthesis and a Structural Survey of Homoleptic Rare Earth(III) 2,6-Diphenylphenolates. *J. Chem. Soc. Dalton Trans.* **2000**, No. 6, 961–966.

(17) Palumbo, C. T.; Kotyk, C. M.; Ziller, J. W.; Evans, W. J. Synthesis and Crystallographic Characterization of Di-phenyl-amide Rare-Earth Metal Complexes Ln$(NPh_2)_3(THF)_2$ and [$(Ph_2N)_2$Ln(μ-NPh_2)]$_2$. *Acta Crystallogr. Sect. E Crystallogr. Commun.* **2020**, *76* (9), 1447–1453.

(18) Fryzuk, M. D.; Love, J. B.; Rettig, S. J. Arene Coordination to Yttrium(III) via Carbon−Carbon Bond Formation. *J. Am. Chem. Soc.* **1997**, *119* (38), 9071–9072.

(19) Fryzuk, M. D.; Jafarpour, L.; Kerton, F. M.; Love, J. B.; Patrick, B. O.; Rettig, S. J. Carbon−Carbon Bond Formation Using Yttrium(III) and the Lanthanide Elements. *Organometallics* **2001**, *20* (7), 1387–1396.

(20) Evans, W. J.; Ansari, M. A.; Ziller, J. W.; Khan, S. I. Utility of Arylamido Ligands in Yttrium and Lanthanide Chemistry1. *Inorg. Chem.* **1996**, *35* (19), 5435–5444.

(21) Hitchcock, P. B.; Huang, Q.; Lappert, M. F.; Wei, X.-H.; Zhou, M. Synthesis and Structures of Some Heterometallic [(Li, Y)2, (M3, Ce) (M = Li or Na), (Li, Zr2) and (Li, Zr)4] Oligomeric Diamides Derived from 1,2-Bis(Neopentylamino)Benzene. *Dalton Trans.* **2006**, No. 24, 2991–2997.
(22) Huang, W.; Dulong, F.; Wu, T.; Khan, S. I.; Miller, J. T.; Cantat, T.; Diaconescu, P. L. A Six-Carbon 10π-Electron Aromatic System Supported by Group 3 Metals. *Nat. Commun.* **2013**, *4* (1), 1448.
(23) Fusi, G. M.; Lim, Z.; Lindell, S. D.; Gomez-Bengoa, E.; Gordon, M. R.; Gazzola, S. 2- and 6-Purinylmagnesium Halides in Dichloromethane: Scope and New Insights into the Solvent Influence on the C−Mg Bond. *Eur. J. Org. Chem.* **2022**, *2022* (7), e202101009.
(24) Brennan, J. G.; Cloke, F. G. N.; Sameh, A. A.; Zalkin, A. Synthesis of Bis(η-1,3,5-Tri-t-Butylbenzene) Sandwich Complexes of Yttrium(0) and Gadolinium(0); the X-Ray Crystal Structure of the First Authentic Lanthanide(0) Complex, [Gd(η-$But_3C_6H_3)_2$]. *J. Chem. Soc. Chem. Commun.* **1987**, No. 21, 1668–1669.
(25) Huang, W.; Le Roy, J. J.; Khan, S. I.; Ungur, L.; Murugesu, M.; Diaconescu, P. L. Tetraanionic Biphenyl Lanthanide Complexes as Single-Molecule Magnets. *Inorg. Chem.* **2015**, *54* (5), 2374–2382.
(26) Fieser, M. E.; Palumbo, C. T.; Pierre, H. S. L.; Halter, D. P.; Voora, V. K.; Ziller, J. W.; Furche, F.; Meyer, K.; Evans, W. J. Comparisons of Lanthanide/Actinide +2 Ions in a Tris(Aryloxide)Arene Coordination Environment. *Chem. Sci.* **2017**, *8* (11), 7424–7433.
(27) Biagini, P.; Lugli, G.; Millini, R. Halogenoarene Complexes of Lanthanide (III): Molecular Structure of Yb (η^6-$C_6H_5CH_3$)$(AlCl_4)_3$ and Gd(η^6-$C_6H_5CH_3$)$(AlBr_4)_3$. *Gazzetta Chim. Ital.* **1994**, *124* (5), 217–225.
(28) Liu, S.-S.; Yan, B.; Meng, Z.-S.; Gao, C.; Wang, B.-W.; Gao, S. Two Half-Sandwich Organometallic Single-Ion Magnets with Toluene Coordinated to the Dy(III) Ion: The [$(C_7H_8)Dy(AlCl_4)_3$] and [$(C_7H_8)Dy(AlBr_4)_3$] Complexes. *Inorg. Chem. Commun.* **2017**, *86*, 312–314.
(29) Harriman, K. L. M.; Murillo, J.; Suturina, E. A.; Fortier, S.; Murugesu, M. Relaxation Dynamics in See-Saw Shaped Dy(III) Single-Molecule Magnets. *Inorg. Chem. Front.* **2020**, *7* (24), 4805–4812.
(30) Evans, W. J.; Allen, N. T.; Ziller, J. W. The Availability of Dysprosium Diiodide as a Powerful Reducing Agent in Organic Synthesis: Reactivity Studies and Structural Analysis of $DyI_2((DME)_3$ and Its Naphthalene Reduction Product1. *J. Am. Chem. Soc.* **2000**, *122* (47), 11749–11750.
(31) Gorlov, M.; Hussami, L. L.; Fischer, A.; Kloo, L. Mononuclear η^6-Arene Complexes of Lanthanides: One-Step Syntheses, Crystal Structures, and Arene Exchange. *Eur. J. Inorg. Chem.* **2008**, *2008* (33), 5191–5195.
(32) Liu, S.-S.; Ziller, J. W.; Zhang, Y.-Q.; Wang, B.-W.; Evans, W. J.; Gao, S. A Half-Sandwich Organometallic Single-Ion Magnet with Hexamethylbenzene Coordinated to the Dy(III) Ion. *Chem. Commun.* **2014**, *50* (77), 11418–11420.
(33) Boyle, T. J.; Bunge, S. D.; Clem, P. G.; Richardson, J.; Dawley, J. T.; Ottley, L. A. M.; Rodriguez, M. A.; Tuttle, B. A.; Avilucea, G. R.; Tissot, R. G. Synthesis and Characterization of a Family of Structurally Characterized Dysprosium Alkoxides for Improved Fatigue-Resistance Characteristics of PDyZT Thin Films. *Inorg. Chem.* **2005**, *44* (5), 1588–1600.
(34) Deacon, G. B.; Junk, P. C.; Moxey, G. J.; Ruhlandt-Senge, K.; St. Prix, C.; Zuniga, M. F. Charge-Separated and Molecular Heterobimetallic Rare Earth–Rare Earth and Alkaline Earth–Rare Earth Aryloxo Complexes Featuring Intramolecular Metal–π-Arene Interactions. *Chem. – Eur. J.* **2009**, *15* (22), 5503–5519.
(35) Fagin, A. A.; Bochkarev, M. N.; Kozimor, S. A.; Ziller, J. W.; Evans, W. J. Comparative Reductive Reactivity of SmI_2 with TmI_2 in the Synthesis of Lanthanide Arene Complexes. *Z. Für Anorg. Allg. Chem.* **2005**, *631* (13–14), 2848–2853.
(36) Bochkarev, M. N.; Fedushkin, I. L.; Fagin, A. A.; Schumann, H.; Demtschuk, J. Triple-Decker Naphthalene Complex of Thulium(III); Synthesis Andmolecular Structure of[{Tm(Dme)}2(η^2-$C_{10}H_8)_2$(μ^2-η^4: η^4-$C_{10}H_8$)]. *Chem. Commun.* **1997**, No. 18, 1783–1784.

(37) Müller-Buschbaum, K.; Quitmann, C. C. Homoleptic Rare-Earth Carbazolates and the Trends of Their E Redox Potentials: Mixed-Valent Samarium in $1\infty[Sm_2(Cbz)_5](CbzH)$ (CbzH = Carbazole) and Trivalent Thulium, Neodymium and Gadolinium in $[Ln_2(Cbz)_6]$. *Eur. J. Inorg. Chem.* **2004**, *2004* (21), 4330–4337.
(38) Bain, G. A.; Berry, J. F. Diamagnetic Corrections and Pascal's Constants. *J. Chem. Educ.* **2008**, *85* (4), 532.
(39) Peng, D.; Middendorf, N.; Weigend, F.; Reiher, M. An Efficient Implementation of Two-Component Relativistic Exact-Decoupling Methods for Large Molecules. *J. Chem. Phys.* **2013**, *138* (18), 184105.
(40) Franzke, Y. J.; Middendorf, N.; Weigend, F. Efficient Implementation of One- and Two-Component Analytical Energy Gradients in Exact Two-Component Theory. *J. Chem. Phys.* **2018**, *148* (10), 104110.
(41) Franzke, Y. J.; Weigend, F. NMR Shielding Tensors and Chemical Shifts in Scalar-Relativistic Local Exact Two-Component Theory. *J. Chem. Theory Comput.* **2019**, *15* (2), 1028–1043.
(42) Peng, D.; Reiher, M. Local Relativistic Exact Decoupling. *J. Chem. Phys.* **2012**, *136* (24).
(43) Pollak, P.; Weigend, F. Segmented Contracted Error-Consistent Basis Sets of Double-and Triple-ζ Valence Quality for One-and Two-Component Relativistic All-Electron Calculations. *J. Chem. Theory Comput.* **2017**, *13* (8), 3696–3705.
(44) Visscher, L.; Dyall, K. G. Dirac–Fock Atomic Electronic Structure Calculations Using Different Nuclear Charge Distributions. *At. Data Nucl. Data Tables* **1997**, *67* (2), 207–224.
(45) J. Franzke, Y.; Treß, R.; M. Pazdera, T.; Weigend, F. Error-Consistent Segmented Contracted All-Electron Relativistic Basis Sets of Double- and Triple-Zeta Quality for NMR Shielding Constants. *Phys. Chem. Chem. Phys.* **2019**, *21* (30), 16658–16664.
(46) Reed, A. E.; Weinstock, R. B.; Weinhold, F. Natural Population Analysis. *J. Chem. Phys.* **1985**, *83* (2), 735–746.